

1

[ATLAS Semivisible Jets]

2

[Elena Laura Busch]

3

Submitted in partial fulfillment of the
requirements for the degree of
Doctor of Philosophy
under the Executive Committee
of the Graduate School of Arts and Sciences

4

5

6

7

8

COLUMBIA UNIVERSITY

9

2024

10

© 2024

11

[Elena Laura Busch]

12

All Rights Reserved

13

Abstract

14

[ATLAS Semivisible Jets]

15

[Elena Laura Busch]

16

Abstract of dissertation (place-holder).

Table of Contents

18	Acknowledgments	xvi
19	Dedication	xvii
20	Introduction or Preface	1
21	I Theory	2
22	Chapter 1: The Standard Model	3
23	1.1 Phenomenology: Particles and Forces	3
24	1.1.1 Particles	3
25	1.1.2 Forces	5
26	1.2 QCD and Jets	7
27	1.3 Symmetries	8
28	1.3.1 Spontaneous Symmetry Breaking and The Higgs Mechanism	9
29	1.4 Experimental Validation of the Standard Model	10
30	1.5 Limitations of the Standard Model	11
31	Chapter 2: Physics Beyond the Standard Model	13
32	2.1 Hidden Valley Models	13
33	2.2 Dark QCD	14

34	2.3 Semi-visible Jets	15
35	II Experiment	17
36	Chapter 3: The Large Hadron Collider	18
37	3.1 Accelerator Physics	19
38	3.1.1 The Journey of a Proton	19
39	3.1.2 Magnets	20
40	3.2 Luminosity	21
41	3.3 LHC Timeline	24
42	Chapter 4: The ATLAS Detector	26
43	4.1 Coordinate System and Geometry	27
44	4.2 Inner Detector	28
45	4.2.1 Pixel Detector	29
46	4.2.2 Semiconductor Tracker	31
47	4.2.3 Transition Radiation Tracker	31
48	4.3 Calorimeters	31
49	4.3.1 Liquid Argon Calorimeter	32
50	4.3.2 Tile Calorimeter	35
51	4.4 Muon Spectrometer	36
52	4.5 Magnet System	38
53	4.6 Forward Detectors	39
54	4.7 Trigger and Data Acquisition	40

55	Chapter 5: Particle Reconstruction and Identification	44
56	5.1 Inner Detector Tracks	44
57	5.2 Photons and Electrons	46
58	5.3 Muons	48
59	5.4 Jets	50
60	5.4.1 Calorimeter Clusters	51
61	5.4.2 Particle Flow Algorithm	52
62	5.4.3 Jet Clustering	53
63	5.4.4 Ghost Track Association	56
64	5.5 Missing Transverse Energy	57
65	III Search	59
66	Chapter 6: Monte Carlo and Data	60
67	6.1 Data	60
68	6.2 Simulation	62
69	6.2.1 Simulated Backgrounds	62
70	6.2.2 Signal Simulation	63
71	Chapter 7: Machine Learning Tools	66
72	7.1 Introduction	66
73	7.1.1 Particle Flow Network (Supervised)	67
74	7.1.2 ANTELOPE (Semi-supervised)	77
75	Chapter 8: Analysis Strategy	84

76	8.1 Preselection	84
77	8.2 SVJ Fit and Discovery Analysis Strategies	86
78	8.3 Analysis Regions	90
79	8.3.1 Control and Validation Regions	90
80	8.3.2 Signal Region	92
81	8.4 Background Estimation	94
82	8.5 Fit Strategy and Validation	95
83	8.5.1 SVJ Fit Strategy	95
84	8.5.2 Discovery Strategy	103
85	Chapter 9: Results	109
86	9.1 SVJ Fit Result	109
87	9.1.1 Systematics	110
88	9.1.2 Interpretation	115
89	9.2 Discovery Result	115
90	Conclusion or Epilogue	118
91	References	122
92	Appendix A: Trigger Studies	129
93	Appendix B: Machine Learning Approaches	133
94	B.1 Unsupervised: AE vs. ANTELOPE	133
95	B.2 PFN Optimality Checks	134

96	B.3 Supervised: BDT vs. PFN	137
97	B.4 Single Jet vs Jet System ML Approach	137
98	B.5 PFN Training Composition	139
99	B.6 E_T^{miss} and $E_T^{miss}\phi$ Shapes	141
100	B.6.1 NCB Preselection	141
101	B.6.2 TileCal Correction	143
102	Appendix C: Truth Studies	146
103	C.1 Jet dR Matching	146
104	Appendix D: BumpHunter	148
105	D.1 Signal Mass Resolution m_T Binning	148

List of Figures

107	1.1	Diagram of the 17 particles comprising the Standard Model	4
108	1.2	Fundamental particle interactions of the three fundamental forces described by the	
109		Standard Model [2].	6
110	1.3	An example Feynmann diagram of jet production	7
111	1.4	An illustration of the “hat shaped” potential of the Higgs field, resulting in a non-	
112		zero vacuum expectation value.	9
113	2.1	Illustration of the hidden valley potential.	14
114	2.2	The massive mediator particle Z' of the s-channel realization of a HV model . . .	14
115	3.1	The LHC accelerator complex at CERN [29]	20
116	3.2	The octants of the LHC and location of various beam activities [28]. Stars indicate	
117		the locations of beam collisions, and the associated detectors recording the	
118		outcome of those collisions.	21
119	3.3	(Left) Total integrated luminosity over the course of Run 2. (Right) Average num-	
120		ber of pp interactions per bunch crossing in Run 2. Each curve is weighted by the	
121		integrated luminosity for the year.	23
122	3.4	Timeline of LHC and HL-LHC activities [31]. Integrated luminosity estimates are	
123		approximate, and not reflective of the exact amount delivered to each experiment. .	25
124	4.1	The ATLAS detector [34].	26
125	4.2	ATLAS coordinate system and geometry	29
126	4.3	A 3D visualization of the structure of the ID in the barrel region [35]	30

127	4.4 A 3D visualization of the structure of the ID end-caps [34]. The paths of two charged particles ($\eta = 1.4$ and 2.2) are illustrated.	30
128		
129	4.5 ATLAS calorimetry system [36]	32
130		
131	4.6 Diagram of a segment of the EMB, demonstrating the accordion plate arrangement and the cell segmentation pattern [37]. Three layers are illustrated, and the variation in the cell granularity between the front layer (Sampling Layer 1) and the back layer (Sampling Layer 3) is shown.	33
132		
133		
134	4.7 A LAr pulse as produced in the detector (triangle) and after shaping (curve) [37] . .	34
135		
136	4.8 Readout gap structure in HEC [37]	35
137		
138	4.9 TileCal wedge module [40]	36
139		
140	4.10 Cross section view of the muon spectrometer system [41]	37
141		
142	4.11 Layout of the barrel and end-cap toroid magnets [34]	39
143		
144	4.12 Block diagram of the L1 trigger process [34]. The overall L1 trigger decision is made by the CTP.	41
145		
146		
147		
148		
149	4.13 Block diagram of the trigger and data acquisition processes, including L1 and HLT processes [45].	42
150		
151		
152		
153		
154		
155	5.1 This graphic illustrates a slice of ATLAS detector barrel [46]. A photon, electron, and two jets (associated to the proton and neutron) are shown, illustrating each object's interaction with various ATLAS subsystems. The path of the charged particles is curved on account of the strong magnetic field produced by the solenoid and toroid magnets. A neutrino, generally representing the reconstruction of missing transverse energy, is also illustrated.	45
156		
149	5.2 Track reconstruction seeding, finding and fitting illustration [47]	46
150		
151	5.3 Three types of EM object candidates [49].	47
152		
153		
154		
155	5.4 The four types of muon track candidates [51]. The red bands indicate where detector measurements for each muon track candidate are made. The dashed lines indicate the path of the muon through detectors where no measurement is made. Standalone muon is another term for an extrapolated muon.	50
156		
155	5.5 The fragmentation and hadronization processes undergone by a quark produced in a proton-proton collision [53].	51
156		

157	5.6 A flow chart illustrating the particle flow algorithm progression [56]. The solid	54
158	lines indicate the progression of tracks through the algorithm, while the dotted	
159	lines indicate the progression of clusters. The process begins with track selection	
160	and continues until the energy associated with the tracks has been removed from	
161	the calorimeter. At the end charged particle tracks, unmodified topo-clusters, and	
162	the remnants of topo-clusters which have had part of their energy removed remain.	
163	5.7 A comparison of jet clustering with four different jet algorithms. The anti- k_t al-	55
164	gorithm is observed to create the most conical jets, where the shape of the jet is	
165	immune to the presence of soft radiation [57].	
166	5.8 A comparison of MC simulation and data for $Z \rightarrow \mu\mu$ events where real $E_T^{\text{miss}} =$	58
167	0 [65]. The resolution of the missing energy in the transverse ($x - y$) plane is	
168	observed to increase with increasing total $\sum E_T$	
169	6.1 Integrated luminosity for the ATLAS experiment as a function of time during Run	61
170	2 [66]	
171	6.2 The transverse momentum slices of the QCD MC simulation, overlayed to show	63
172	how they come together to create a smooth distribution (left) once weighted prop-	
173	erely. The original unweighted distribution is shown on the right, illustrating the	
174	enhanced statistics for the high p_T range.	
175	6.3 Background processes relevant to the SVJ signal.	64
176	7.1 The Energy/Particle Flow Network concept, from Ref. [75].	68
177	7.2 An annotated diagram of the PFN architecture. y and ϕ represent geometric in-	68
178	formation for the input particles, z represents energy information, and PID encom-	
179	passes any other particle ID information in the input.	
180	7.3 A illustration of the expected dijet behavior of semi-visible jets, where one jet is	69
181	closely aligned with E_T^{miss}	
182	7.4 Illustration of track coordinates d_0 and z_0	70
183	7.5 Distributions of the track multiplicity in the leading and subleading jets, comparing	70
184	signal and background PFN training samples.	
185	7.6 A diagram demonstrating how the two jet system is rotated in (ϕ, η)	71

186	7.7 The 6 PFN track variables in background MC and signal MC. There are some 187 differences between signal and background, but the track kinematics are largely 188 similar.	71
189	7.8 The 6 PFN track variables in data and background MC, after the scaling and ro- 190 tation procedure is applied. There is excellent modeling of the data by the MC 191 within the track variables. The slight discrepancy in the phi distribution is due to 192 the modeling of dead TileCal cells by the QCD MC, which will be discussed in 193 Chapter 8. The level of discrepancy is determined to be within tolerance given that 194 the final result will be data driven and the QCD model is used in the PFN training 195 only.	72
196	7.9 PFN score for background MC, data, and signal, comparing a PFN training on 197 QCD-only vs all-background MC samples. The average AUC for the QCD-only 198 training (left) is 0.93, while the average AUC for the mixed background training 199 (right) is 0.84. The sensitivity estimate across the grid is better for the QCD-only 200 training - from the distribution we can conclude that this is because the sensitivity 201 to MET enhanced signals is greatly reduced.	74
202	7.10 PFN architecture loss during training as a function of epoch (left) and the evaluated 203 loss over the signal and background (right).	74
204	7.11 ROC the PFN score for combined signal (true positive) and QCD background (false 205 positive).	75
206	7.12 AUC from the PFN score for each signal in the SVJ grid, shown versus the QCD- 207 only training sample.	76
208	7.13 PFN score for two signals and the total background MC (top), and between data 209 and MC (bottom). The difference between data and MC efficiency is minimal (< 210 5%).	76
211	7.14 A visual representation of the 64 PFN latent space variables which create the input 212 of the VAE component of ANTELOPE. The left shows a 2D histogram of the PFN 213 latent space index (0-63) versus the value assumed by that index. The right shows 214 1D histograms of two particular PFN latent space variables.	78
215	7.15 An annotated diagram of the ANTELOPE architecture.	79
216	7.16 ANTELOPE architecture loss during training as a function of epoch.	80
217	7.17 ANTELOPE score distribution comparing data and the total background MC (left), 218 with good agreement observed between data and simulated background, and com- 219 paring all background MC to signals (right), revealing good discrimination power. 220	81

221	7.18 AUC from the ANTELOPE score for each signal in the SVJ grid.	82
222	7.19 Comparing data and the alternate signal models for the PFN score (left) and AN-	
223	TELOPE score (right). The emerging jet signal is an example of the gain of the	
224	model-independent ANTELOPE approach, where it has a bimodal shape in PFN	
225	score but is clearly tagged as anomalous by ANTELOPE.	83
226	7.20 Comparing data and the alternate signal models in terms of sensitivity (S/\sqrt{B}) for	
227	the PFN and ANTELOPE tools, applying the selection that is used in the analysis.	
228	The ANTELOPE network is found to provide significant added sensitivity to alter-	
229	nate signals such as the gluino → R-hadron and emerging jets, which have higher	
230	E_T^{miss} than the SVJs.	83
231	8.1 Preselection cutflow for data (left) and signal (right).	85
232	8.2 Energy and momentum analysis variables at preselection, for data, all background	
233	MC and representative signal models. m_T is the key fit variable, and this plot	
234	illustrates the smoothly falling background in comparison to the resonant shape of	
235	the signals. m_T is further illustrated in Figure 8.9.	87
236	8.3 Orientation analysis variables at preselection, for data, all background MC and	
237	representative signal models. While $\Delta\phi(E_T^{\text{miss}}, j)$ variables are not used explicitly	
238	in the analysis flow, they help create a picture of the event.	88
239	8.4 Flow of analysis selections, regions, and background estimation/validation fitting	
240	strategy. TODO: diagram needs to be corrected	89
241	8.5 Distributions of the subleading jet width width_{j2} (left) and leading jet with width_{j1}	
242	(right) in data, background MC and signals at preselection. All SVJ signals are	
243	seen to be wider than the background in width_{j2} . The same is not true for width_{j1} ,	
244	where some signals are observed to closely match the background.	90
245	8.6 2D plots revealing correlations between width_{j2} and m_T (left), width_{j2} and ML	
246	score (middle), and m_T with ML score (right). For the top row, the ML score is	
247	the PFN score, and for the bottom three, the ML score is the ANTELOPE score.	
248	Minimal correlations are observed and are shown to not sculpt m_T , validating these	
249	variables for analysis region construction and statistical treatment.	91
250	8.7 m_T in simulation across the CR, VR, and SR for both PFN (left) and ANTELOPE	
251	(right) selections.	92

252	8.8 Definition of CR, VR, and SR regions using width_{j2} and the ML score, along with 253 the population of each region in data statistics. The SVJ Fit region is shown on top 254 with the PFN score on the x-axis, and Discovery region is shown on the bottom, 255 with the ANTELOPE score on the x-axis.	93
256	8.9 The resonant shape of the SVJ signals in m_T , in contrast to the smoothly falling 257 m_T background. The high R_{inv} signals (right) boast a wider shape, making them 258 more difficult to detect, while the low R_{inv} signals(left) produce a more narrow 259 resonance in m_T	94
260	8.10 Background-only m_T fits using representative MC in the CR (left), VR (middle), 261 and SR (right).	96
262	8.11 Background-only m_T fits using data in the full statistics CR and VR regions.	97
263	8.12 m_T distribution in the data CR, before (left) and after (right) smoothing.	98
264	8.13 Background-only m_T fits using pseudo-data from the CR template.	99
265	8.14 p -value histograms from 100 fits to Asimov data in the CR.	99
266	8.15 Example S+B fit on a background m_T spectrum with injected signal from the point 267 ($4000 \text{ GeV}, R_{inv}=0.2$).	100
268	8.16 Measured signal at a variety of injected values (1x, 2x, and $5\sqrt{b}$), for all signal 269 points in the grid, $R_{inv}=0.2$ (top left), 0.4 (top right), 0.6 (bottom left), and 0.8 270 (bottom right).	101
271	8.17 95% C.L. upper limits for signal models across Z' mass, for four different R_{inv} frac- 272 tions, from the CR region (without systematics). TODO - ATLAS style	102
273	8.18 95% C.L. upper limits and observed limit for signal models across Z' mass, with 274 varying amounts of signal injected. TODO - ATLAS style	103
275	8.19 Post-fit function and residuals for the ANTELOPE CR and VR.	104
276	8.20 BumpHunter fits on the ANTELOPE m_T spectra for both the CR (left) and VR 277 (right). In a signal-depleted region, good agreement with the background estima- 278 tion is observed.	105
279	8.21 BumpHunter p-values extracted for 100 Asimov toys for both the ANTELOPE CR 280 (left) and VR (right).	106
281	8.22 Example injected gaussian signal.	106

282	8.23 Response of the BumpHunter framework to signal injection of 5σ significance to 283 the model-dependent polynomial fit framework. The local significance (top) and 284 bump location (bottom) are shown.	108
285	8.24 Example BH response to gaussian signal injection at 4000 GeV with width of 10%.	108
286	9.1 m_T in the unblinded SVJ Fit SR with a background-only fit (p-value = 0.265).	109
287	9.2 Example spurious signal fits, indicating a Gaussian distribution around the mean 288 of spurious signal events.	111
289	9.3 Spurious signal as a function of resonance mass. The requirement $\mu/\sigma < 0.5$ is 290 satisfied for all signal points, where μ is the mean number of spurious signal events 291 and σ is the standard deviation of the number of spurious signal events from 100 292 pseudo-data experiments.	111
293	9.4 m_T of the 3500 GeV Z' , $R_{inv} = 0.2$ signal point, shown with an example JES 294 variation. The nominal shape (“Nom”), 1σ up (“Up”), and 1σ down (“down”) 295 variations are shown. The variation is seen to have a negligible impact on the 296 signal shape.	113
297	9.5 m_T of the 3500 GeV Z' , $R_{inv} = 0.2$ signal point, shown with the sum in quadrature 298 of all JES and JER variations. The nominal shape (“Nom”), 1σ up (“Up”), and 1σ 299 down (“down”) variations are shown.	114
300	9.6 Signal distribution of m_T , varying the ISR, FSR and MPI configuration.	114
301	9.7 Expected and observed 95% CL limits in the unblinded SR, as a function of Z' 302 masses for $R_{inv}=0.2$ (top left), 0.4 (top right), 0.6 (bottom left), 0.8 (bottom right); 303 no systematics.	116
304	9.8 m_T in the unblinded ANTELOPE SR with a background-only fit (p-value = 0.74), 305 left. BumpHunter test selecting the most significant data excess with a p-value of 306 0.8098, right.	117
307	A.1 Trigger yield and efficiency for both the MET trigger and small-R jet trigger ap- 308 proach. Each entry represent a signal point, labelled by the Z' mass and the 309 R_{inv} fraction.	129
310	A.2 The factor of improvement in S/\sqrt{B} for each trigger method compared to the un- 311 triggered case.	130
312	A.3 The ratio of S/\sqrt{B} of jet trigger over E_T^{miss} trigger selection.	130

313	A.4 Analysis variables where high R_{inv} signals a clearly distinct from background and 314 low R_{inv} variables. On the contrary, leading jet p_T is one of the only variables 315 where low R_{inv} signals are distinct from background.	132
316	A.5 OR of jet and E_T^{miss} triggers.	132
317	B.1	133
318	B.2	134
319	B.3 AUC from the PFN score for each signal in the SVJ grid, shown versus the QCD- 320 only training sample (top) and the total MC background (bottom). Note the three 321 missing points will be added shortly - they were delayed due to a DAOD production 322 mistake.	135
323	B.4 Comparison of PFN AUC (top), SIC (middle), and sensitivity in the m_T mass win- 324 dows (bottom) for a single PFN model (left) vs. two models, trained on $R_{inv} < 0.5$ 325 and > 0.5 separately.	136
326	B.5 Preferred cuts on the PFN score for each point in the grid, comparing the effect of 327 adding the NCB preselection.	137
328	B.6 Scans done to check for optimality of PFN training parameters.	138
329	B.7	138
330	B.8 ϕ Performance comparison between single jet and jet system ML approach	139
331	B.9 ϕ Comparison in the AUC score across the grid for the mixed background strategy 332 vs the QCD only strategy. The bottom table highlights that the QCD only strategy 333 gives superior sensitivity across the signal grid.	140
334	B.10 E_T^{miss} in data before and after Tight event cleaning is applied.	141
335	B.11 E_T^{miss} vs jet1 p_T in data before and after Tight event cleaning is applied.	142
336	B.12 η vs ϕ for leading and subleading jets, before and after the application of tight 337 cleaning.	142
338	B.13 Added NCB preselection and impact on E_T^{miss} shape.	143
339	B.14 NCB preselection impact on data and signal yields.	144
340	B.15 Impact of tight cleaning and non-collision background preselection.	145

341	B.16 $E_T^{\text{miss}}\phi$ in data, before (left) and after (right) application of the TileCal correction	
342	tool.	145
343	C.1 Index of jets truth matched (by requirement of $\Delta R < 0.4$) with dark quark.	146
344	C.2 Percent of jets with $\Delta R(j, E_T^{\text{miss}}) < 0.4$ comparing two jet identification strategies.	
345	Leading and subleading jets are seen to be the better metric for identifying jets	
346	associated with the dark quark decay.	147
347	D.1 Example determinations of the 60% mass window means for several signal points.	149
348	D.2 Signal mass resolution for m_T binning for the signal grid in (R_{inv}, mass) space.	149
349	D.3 m_T bins based on the signal mass resolution and the minimum 100 GeV width	
350	requirement, for each R_{inv} signal category.	150

List of Tables

352	4.1 General performance goals of the ATLAS detector [34].	27
353	6.1 Fixed parameters in the Pythia8 HV model	64
354	6.2 Values for m_{dark}	65
355	6.3 Mass points and cross sections of the SVJ search signal grid	65
356	8.1 Post-fit parameters for the PFN CR and VR. $p1$ can also be considered N_{bkg} or the 357 normalization factor.	97
358	8.2 Post-fit parameters for the ANTELOPE CR and VR.	104
359	9.1 Post-fit parameters for the PFN SR. $p1$ can also be considered N_{bkg} or the normal- 360 ization factor.	110
361	9.2 Summary of Experimental Uncertainties and their impact on the yield of MC signal 362 events.	112

363

Acknowledgements

364 Insert your acknowledgements text here. This page is optional, you may delete it if not

365 needed.

366

Dedication

367

Dedicated to my friends and family

368

Introduction or Preface

369 Insert your preface text here if applicable. This page is optional, you may delete it if not
370 needed. If you delete this page make sure to move page counter comment in thesis.tex to correct
371 location.

372

Part I

373

Theory

Chapter 1: The Standard Model

376 The Standard Model of particle physics is a universally accepted framework which explains
 377 the interactions of fundamental particles. All known fundamental particles, outlined in Figure
 378 1.1, are represented in the Standard Model. The model describes three of the four known forces:
 379 the electromagnetic force, the weak force, and the strong force. Gravity, the fourth fundamental
 380 force, is not addressed by the Standard Model. The Standard Model was primarily developed over
 381 the course of the 1960s and 1970s, by combining the work of many physicists into one coherent
 382 model. The Standard Model has been established as a well-tested theory by decades of experimen-
 383 tal physics research.

384 This chapter will seek to introduce the phenomenology and mathematical foundations of the
 385 Standard Model, and present the supporting experimental evidence. Phenomenon which are unex-
 386 plained by the Standard Model such as gravity will be considered at the end of the chapter, leading
 387 to an exploration of theories beyond the Standard Model in the subsequent chapter.

388 **1.1 Phenomenology: Particles and Forces**

389 1.1.1 Particles

390 A classic representation of the particles comprising the Standard Model is shown in Figure
 391 1.1. The two primary particles classes are bosons (gauge bosons and the scalar Higgs boson) and
 392 fermions (leptons and quarks). The bosons are carriers of fundamental forces, while the fermions
 393 are the building blocks of matter. Fermions are sorted into three *generations*, and each fermion is
 394 identified by a unique *flavor*.

395 Each entry in the table in Figure 1.1 is accompanied by 3 characteristic numbers: mass, charge,
 396 and spin. The mass of each particle is determined to limited precision by experimental observation,

Standard Model of Elementary Particles

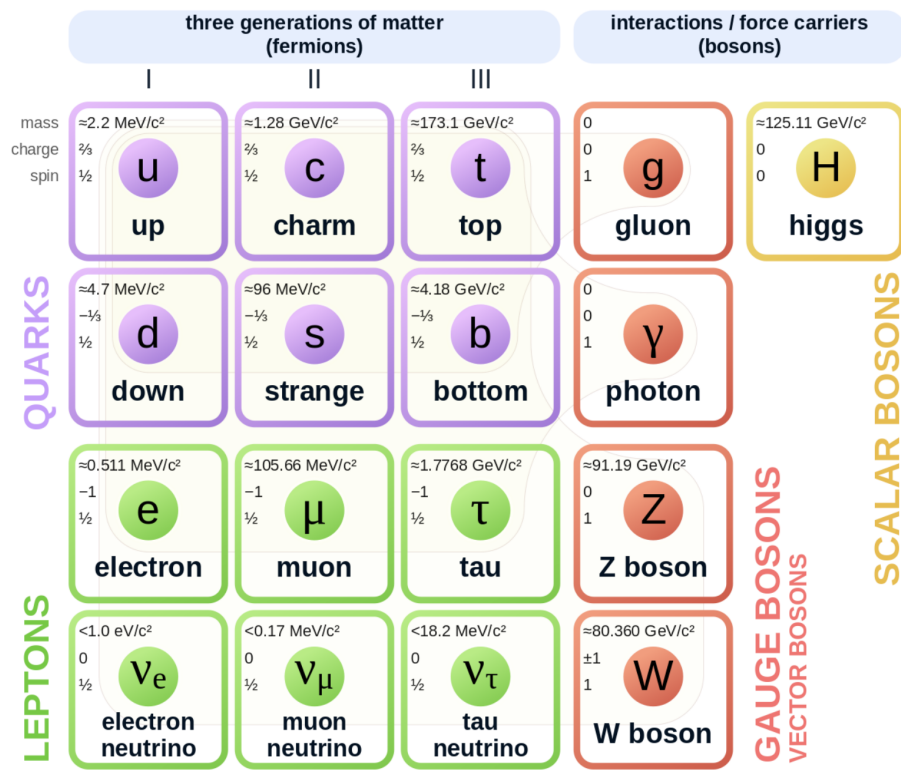


Figure 1.1: Diagram of the 17 particles comprising the Standard Model

397 with the exception of photons and gluons which are known to be massless. Charge refers to the
398 electromagnetic charge, which is integer for leptons and fractional for quarks. Spin is an intrinsic
399 form of angular momentum carried by fundamental particles; all fermions have half integer spin,
400 while bosons have integer spin.

401 Each particle is also known to have an *antiparticle*. Each antiparticle has the same mass but the
402 opposite charge of their Standard Model counter part; for example, the antiparticle of the electron
403 is the positron, which has all the same properties but a positive charge. The photon, Z boson,
404 and Higgs are each their own antiparticle. The nature of antineutrinos is an open question driving
405 neutrino physics research, as it is not currently known whether neutrinos are their own antiparticle.

406 1.1.2 Forces

407 The three fundamental forces explained by the Standard Model are the electromagnetic force,
408 the strong force, and the weak force. The photon is the carrier of the electromagnetic force, which
409 dictates the nature of interactions between electrically charged particles, and is widely covered by
410 introductory physics courses. The electromagnetic force has an infinite interaction range, a result
411 of the massless and non-self interaction nature of the photon. The electromagnetic interaction is
412 described by the theory of quantum electrodynamics (QED).

413 The weak force gives rise to atomic radiation and decay. It allows for the processes of beta
414 decay, which enables conversion between neutrons and protons within the nucleus of an atom. In
415 the process of beta decay, a proton decays into a neutron, a positron, and a neutrino; or, a neutron
416 decays into a proton, an electron and an antineutrino. The weak interaction allows for quark flavor
417 mixing, the which enables beta decay. The W^+ , W^- , and Z^0 are the force carriers of the weak force.
418 The effective range of the weak force is limited to subatomic distances, as a result of the massive
419 nature of the mediator bosons. The unified theory of the electroweak interaction posits that at high
420 enough energies the electromagnetic interaction and the weak force merge into the same force.
421 This threshold is termed the unification energy and calculated to be about 246 GeV [1].

422 The strong force confines quarks into hadron particles, such as protons and neutrons. The

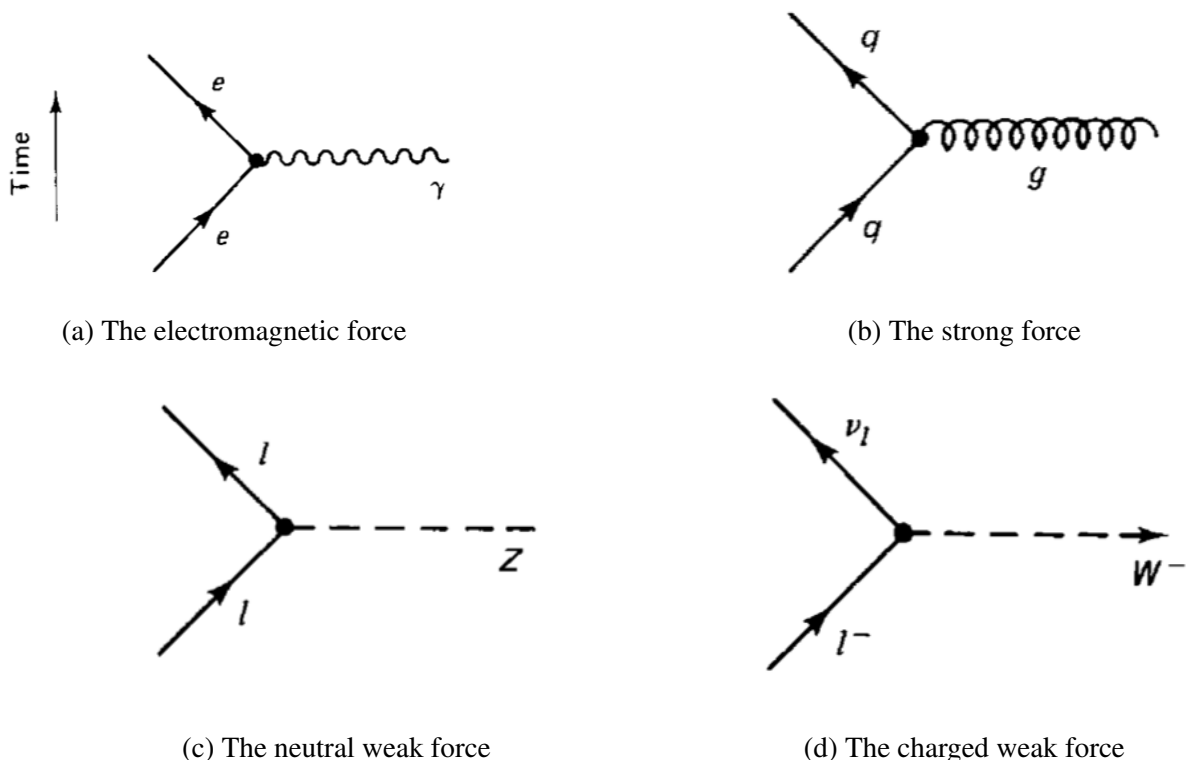


Figure 1.2: Fundamental particle interactions of the three fundamental forces described by the Standard Model [2].

423 strong force also allows for the creation of atomic nuclei by binding protons and neutrons together,
424 and is generally referred to as the “nuclear force” in this context. The gluon is the mediator of
425 the strong force, which is a short-range force which acts at subatomic distances on the order of
426 10^{-15} m. At this range, the strong force is about 100x as strong as the electromagnetic force,
427 which allows for the creation of positively charged nuclei [2]. The strong force is described by the
428 theory of quantum chromodynamics (QCD). In the same way that QED dictates the interaction of
429 electrically charges particles, QCD dictates the interactions of *color-charged* particles. Due to the
430 particular importance of QCD in this thesis, this topic will be explored in detail in section 1.2.

431 The fundamental Feynmann diagram for each of the three forces discussed here is depicted
432 in Figure 1.2. The fourth fundamental force, gravity, is not currently explained by any known
433 mechanism within the Standard Model.

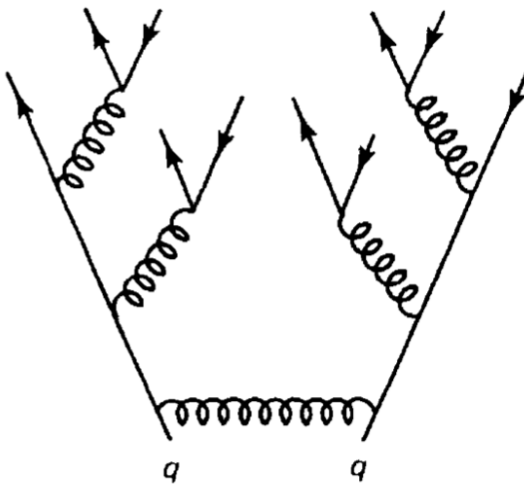


Figure 1.3: An example Feynmann diagram of jet production

434 1.2 QCD and Jets

435 While there is only one type of electric charge, there are three types of color charge; red, green,
 436 and blue. In the process $q \rightarrow q + g$, the color of the quark can change. In order to conserve color
 437 charge, gluons are bicolored, and always carry some positive color charge and some negative color
 438 charge.

439 Color charged particles can only exist in bound states which result in a neutral total color
 440 charge, a principle known as confinement. This requires that quarks and gluons exist in group
 441 states known as hadrons; either mesons in the case of two quarks or baryons in the case of three
 442 quarks. When a quark is separated from a hadron, confinement dictates that other colored objects
 443 are produced around the quark to obey confinement. An example of this process is shown in
 444 Figure 1.3. This ensemble of objects, generally a mixture of quarks and gluons, is termed a *jet*.
 445 Jets are among the most common phenomenon observed by detectors at hadron colliders, and their
 446 complex structure makes them a key focus of many physics analyses.

447 **1.3 Symmetries**

448 The Standard Model is a renormalizable quantum field theory that obeys the local symmetry

449 G_{SM} :

$$G_{SM} = SU(3)_C \times SU(2)_L \times U(1)_Y. \quad (1.1)$$

450 The $SU(3)_C$ symmetry component represents the non-Abelian gauge group of QCD. There
451 are 8 generators for the $SU_C(3)$ group which correspond to 8 types of gluon, each representing a
452 different superposition of color charge [3]. The $SU(2)_L \times U(1)_Y$ symmetry group represents the
453 electroweak sector of the Standard Model, which can be spontaneously broken into the electromag-
454 netic and weak sectors. There are 4 generators for this group, which correspond to four massless
455 gauge bosons W^1 , W^2 , W^3 , and B . From these massless gauge bosons are formed the massive
456 mediators of the weak force, the W^- , W^+ and Z^0 bosons, and the massless electromagnetic force
457 carrier, the photon γ . Spontaneous symmetry breaking and the process by which gauge bosons
458 acquire mass will be addressed in section 1.3.1.

459 Noether's theorem [4] stipulates that any continuous symmetry is associated with a conserved
460 quantity. In the Standard Model, this means that the $SU(3)_C$ symmetry gives rise to conservation of
461 color charge. The $SU(2)_L \times U(1)_Y$ symmetry gives rise to conservation of electromagnetic charge.
462 Conservation of spin results from the Poincaré symmetry described by the theory of special rela-
463 tivity, which combined with Noether's theorem gives us the conservation of energy, momentum,
464 and angular momentum.

465 The SM Lagrangian is invariant under CPT symmetry, or charge, parity, and time reversal.
466 Charge conjugation (C) transform a particle into its corresponding antiparticle by reversing the
467 charge and other quantum numbers. Parity conjugation (P) reverses spatial coordinates, which
468 transforms left-handed particles into right-handed particles and vice-versa. Time reversal (T) is
469 the theoretical process of reversing time. The L subscript in the $SU(2)_L$ group indicates that this
470 symmetry only applies to left-handed fermions. As a result, the $W^{1,2,3}$ gauge bosons of $SU(2)_L$

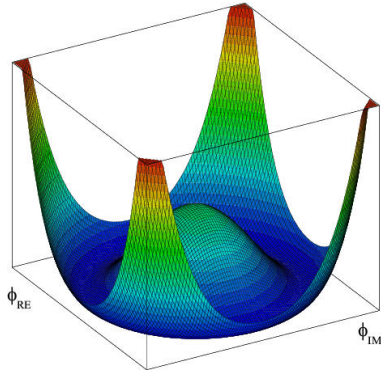


Figure 1.4: An illustration of the “hat shaped” potential of the Higgs field, resulting in a non-zero vacuum expectation value.

only interact with left handed particles, a process which maximally violates P-symmetry in the weak force. A small amount of the CP symmetry violation is also observed in the Standard Model, through the decays of strange flavored mesons [5] and b -mesons [6]. The CPT theorem posits that the violation of CP symmetry implies that T-symmetry must also be violated, so that CPT is a preserved symmetry.

1.3.1 Spontaneous Symmetry Breaking and The Higgs Mechanism

Spontaneous symmetry breaking is the process by which a Lagrangian obeys a symmetry at high energies, but exhibits asymmetric behavior at lower energies. The electroweak symmetry group is spontaneously broken as $SU(2)_L \times U(1)_Y \rightarrow U(1)_{EM}$. The quantity conserved by the $SU(2)_L$ symmetry is weak isospin $T_{1,2,3}$, while the quantity conserved by $U(1)_Y$ symmetry is weak hypercharge Y . Below very high energies, the presence of the Higgs field causes the electroweak symmetry to break. The Higgs field is a scalar field which forms a complex doublet of the $SU(2)$ symmetry group, with four degrees of freedom. The shape of the Higgs field potential, shown in Figure 1.4, results in a ground state with a non-zero vacuum expectation value; thus the Higgs field takes a non-zero value throughout all space, which breaks the symmetry of the weak isospin $SU(2)$ group.

The interaction with the Higgs field mixes the four massless gauge bosons $W^{1,2,3}$ and B . Three Higgs field degrees of freedom mix with the massless gauge bosons, resulting in three massive

489 gauge bosons W^- , W^+ and Z^0 . The massless photon γ is created from the components of the
490 massless gauge bosons which do not interact with the Higgs field. The scalar Higgs boson arises
491 from the one unmixed degree of freedom the Higgs field. Spontaneous symmetry breaking also
492 violates the conservation of weak isospin and weak hypercharge, leaving only electromagnetic
493 charge ($Q = T_3 + \frac{1}{2}Y$) as a conserved quantity associated with the $U(1)_{EM}$ symmetry.

494 **1.4 Experimental Validation of the Standard Model**

495 The theoretical framework of the Standard Model coalesced into a unified theory in the mid-
496 20th century. A cascade of discoveries providing empirical evidence for the model followed
497 closely. In the 1960s, three quarks (up, down and strange) and four leptons (electron, muon,
498 and their associated neutrinos) were the known particulate building blocks of matter and the Stan-
499 dard Model. The discovery of the charm quark in 1974, through the observation of the J/ψ meson
500 [7][8], confirmed the existence of a fourth quark flavor. The discovery of the τ in 1975 [9] provided
501 the first evidence of a 3rd generation of matter. This was quickly followed by the observation of
502 the Υ meson in 1977 [10], which provided evidence for the existence of a fifth quark, the b quark
503 (bottom, or beauty). The existence of a 3rd generation of fermion also explained the observation
504 of CP violation in the weak force, as it allowed for the addition of a complex phase in the CKM
505 matrix (a unitary matrix which describes flavor mixing in the weak interaction). The top quark
506 (t) and tau neutrino (ν_τ) were predicted at this point as the final building blocks of three complete
507 generations of fermions, and they were discovered by experimental observation around the turn of
508 the 21st century [11] [12] [13].

509 The W and Z bosons were predicted by the Standard Model, but to observe them required the
510 construction of a particle accelerator powerful enough to produce them. They were finally observed
511 at CERN in 1983 by the UA1 and UA2 experiments [14] [15] at the newly constructed Super Proton
512 Synchrotron (SPS). Their masses were observed to be compatible with the masses predicted by the
513 Standard Model nearly a decade earlier. The final missing piece then was confirming the existence
514 of the Higgs, which again required the construction of a newer and more powerful collider. CERN

515 achieved this with the construction of the Large Hadron Collider (LHC), and in 2012 the ATLAS
516 and CMS experiments announced the discovery of the Higgs particle [16] [17].

517 1.5 Limitations of the Standard Model

518 While the Standard Model has enjoyed decades of experimental results which confirm its pre-
519 dictions, there are several glaring shortcomings. The observed phenomenon for which the Standard
520 Model provides no explanation are summarized below.

- 521 • Gravity - the Standard Model does not account for the fourth fundamental force of gravity.
- 522 • Dark Matter - there is no viable candidate to explain the existence of dark matter, a non-
523 interacting form of matter which must exist to account for gravitational observations which
524 cannot be explained by general relativity, such as the motion of galaxies, gravitational lens-
525 ing, and the structure of the universe [18].
- 526 • Matter-Antimatter asymmetry - the level of CP violation in the Standard Model isn't suf-
527 ficient to explain the large discrepancy between the amount of matter and the amount of
528 antimatter in the universe today, and the origins of this imbalance are not understood.
- 529 • Neutrino masses - the Standard Model assumes that neutrinos are massless and provides
530 no mechanism for them to acquire mass. However, observations of neutrino oscillations
531 indicates they posses some small non-zero mass [19].

532 In addition to these unexplained natural phenomenon, there are several questions about the
533 *naturalness* of the Standard Model. The principle of naturalness states that dimensionless ratios
534 between physical constants should be of order 1, and that nature should not be arbitrarily fine-
535 tuned. While this is largely an aesthetic argument, it points to many aspects of the Standard Model
536 for which there exists no natural explanation.

- 537 • Strong CP - while CP symmetry is violated in the weak force, observations indicate that it
538 is preserved by the strong force [20]. The Standard Model predicts that CP violation in the

539 strong force is possible. There is no principle which motivates this incongruity between the
540 weak force and strong force.

- 541 • Hierarchy Problem - The wide range of masses for elementary particles and the wide range of
542 scales at which the four fundamental forces operate is not motivated by the SM. Specifically,
543 it is not understood why the Higgs mass is observed to be well below the Plank scale λ ,
544 which is the energy level at which the effects of quantum gravity become significant. QFT
545 indicates that the Higgs mass is determined by contributions from all energy scales including
546 λ , meaning that its observed mass is inexplicably small.

547 The limitations of the Standard Model provide a road map for theoretical and experimental
548 particle physicists, who seek to develop new theories which account for these observations, and
549 then to find evidence which might support these *Beyond the Standard Model* (BSM) theories. The
550 next chapter will introduce the BSM theories which motivate the physics search presented in this
551 thesis.

Chapter 2: Physics Beyond the Standard Model

554 In light of the various phenomenon unexplained by the Standard Model, physicists have pro-
 555 posed various extensions to the Standard Model, collectively termed *Beyond the Standard Model*
 556 (BSM) theories. A particular focus of the physics programs at the Large Hadron Collider (LHC)
 557 are BSM models which suggest dark matter candidate particles. If these particles couple to Stan-
 558 dard Model, they could be produced and observed at the LHC. This chapter will explore Hidden
 559 Valley models, and in particular the potential for Hidden Valley models to produce *semi-visible*
 560 *jets*. This will set the theoretical foundations for the experimental search presented in the later
 561 chapters of this thesis. The mechanisms of dark QCD that arise from these models and allow for
 562 the production of semi-visible jets will also be discussed.

563 **2.1 Hidden Valley Models**

564 Hidden Valley (HV) models are a category of BSM models that allow for dark matter (DM)
 565 production at the LHC. They extend the Standard Model with an additional non-Abelian gauge
 566 group [21]. This introduces the possibility of a complex dark sector, which mirrors the complexities
 567 of Standard Model QCD, and introduces the possibility of dark quarks and gluons. The term
 568 “hidden valley” refers to the idea that the DM is hidden from the SM by a high-energy barrier, as
 569 illustrated in Figure 2.1. The dark sector is assumed to communicate with the Standard Model via
 570 a “portal”, or “messenger particle”, that can interact with both Standard Model and HV forces. For
 571 the s-channel scenario, the portal is considered to be a new massive mediator particle Z' .

572 The portal particle allows for the production of dark sector particles at hadron colliders. If
 573 dark quarks are produced via the decay $Z' \rightarrow q_D q_D$ they can hadronize and form dark jets. The
 574 properties of the dark jets are determined by the dynamics of the dark sector, which are explored in

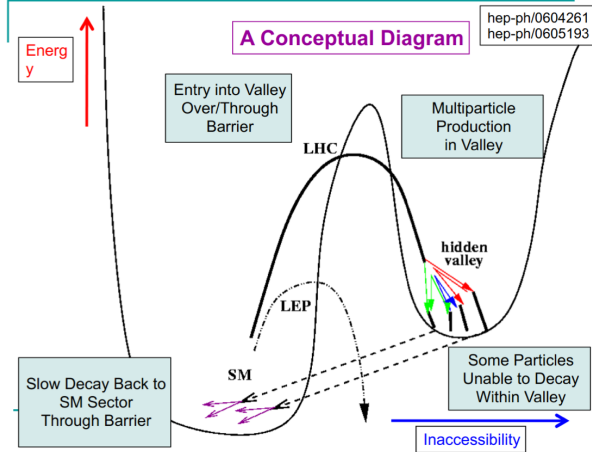


Figure 2.1: Illustration of the hidden valley potential.

575 the subsequent section. Depending on the details of the model, the jets formed by the dark hadrons
 576 can be categorized as fully dark, semi-visible, leptonic, emerging, or other [21].

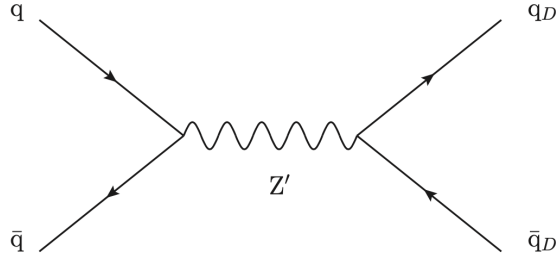


Figure 2.2: The massive mediator particle Z' of the s-channel realization of a HV model

577 2.2 Dark QCD

578 The theoretical underpinning of the semi-visible jet phenomenology is a dark sector with a
 579 gauge group $SU(N)_d$ leading to confinement at a scale Λ_d . For illustration, let's consider the
 580 case of an $SU(2)_d$ gauge theory, which gives rise to two dark fermionic generations $\chi_a = \chi_1, \chi_2$.
 581 Following the work of Ref [22] we can write the fundamental dark Lagrangian as:

$$\mathcal{L}_{dark} \supset -\frac{1}{2} \text{Tr} G_{\mu\nu}^d G^{d\mu\nu} - \bar{\chi}_a (i\cancel{D} - M_{d,a}) \chi_a \quad (2.1)$$

582 The first term allows for the dark gluons to self-interact, while the second term enables the dark
583 quarks to hadronize and acquire mass. The dark quarks are assumed to have a common mass M_d .

584 The coupling strength of the strongly interacting dark quarks is termed α_d . At the confinement
585 scale Λ_d , the dark quarks can form bound states. At the scale $M_d \approx \Lambda_d$ a QCD-like shower occurs.

586 The properties of the hadrons formed by the dark quarks are of particular importance to the
587 observed dark QCD dynamics. Dark-isospin number $U(1)_{1-2}$ and dark-baryon number $U(1)_{1+2}$
588 are accidental symmetries of the theory which determine the stability of the hadrons. In the case
589 of two dark flavors, six dark hadrons can be formed: four mesons ($\chi_1\bar{\chi}_1$, $\chi_2\bar{\chi}_2$, $\chi_1\bar{\chi}_2$, $\bar{\chi}_1\chi_2$) and
590 two baryons ($\bar{\chi}_1\bar{\chi}_2$, $\bar{\chi}_1\chi_2$). The mesons $\chi_1\bar{\chi}_2$ and $\bar{\chi}_1\chi_2$ are charged under dark-isospin and will be
591 stable if this symmetry is unbroken. The baryons would also be stable as they are charged under
592 the dark-baryon number. These four stable hadrons become dark matter candidates of the theory.

593 The $\chi_1\bar{\chi}_1$ and $\chi_2\bar{\chi}_2$ mesons are not charged under either symmetry and are thus expected to decay.
594 The unstable mesons can decay into stable dark mesons, or into an off-shell Z' . The off-shell Z'
595 will then decay into two DM quarks or two SM quarks, and its products will continue to shower
596 until the final state particles are stable.

597 The number of stable and unstable dark states varies substantially depending on the details
598 of the model. The model discussed above can be generalized from $SU(2)_d$ to $SU(N)_d$, with any
599 number of colors N_c or flavors N_f . This affects the ratio of possible stable to unstable mesons,
600 which can directly impact the amount of missing energy. The fraction of missing energy is a
601 variable in many dark QCD models, and is especially important in the case of semi-visible jets.

602 2.3 Semi-visible Jets

603 A “semi-visible jet” occurs when the heavy Z' messenger particle decays into dark quarks,
604 which then hadronize in a QCD-like shower. If some of the dark hadrons are stable while others
605 decay to SM quarks via the off-shell Z' , a collimated mixture of visible and dark matter is formed
606 – this is termed a semi-visible jet. If the Z' messenger particle is produced at rest, the two jets will
607 be back-to-back in the transverse plane. If there is an imbalance in the amount of invisible particles

608 between the two jets, one of the jets will be observed to be aligned with missing transverse energy.

609 While there are a myriad of HV and dark QCD models, a handful of model parameters are most
610 important in determining the observable of these showers within a particle detector. The coupling
611 strength α_d is one of the most important, as it controls the fraction of dark hadrons emitted in the
612 shower and their average p_T . The mass of the dark quarks directly impacts the jet mass. If the
613 masses of the dark quark flavors are comparable, the ratio of stable to unstable dark hadrons will
614 be approximately 1:1. However, if there is a mass splitting, stable or unstable dark hadrons may
615 be favored, which impacts the amount of missing energy observed.

616 The ratio of stable to unstable dark hadrons in the shower is a critical variable for capturing the
617 behavior of dark showers. This value is termed R_{inv} :

$$R_{inv} = \frac{\# \text{ of stable hadrons}}{\# \text{ of hadrons}} \quad (2.2)$$

618 Events containing jets aligned with missing transverse momentum are generally considered to
619 be misreconstructed by other DM searches, and therefore discarded. This class of final states is
620 therefore largely uncovered by existing DM searches. The nature of the dark hadron shower is
621 determined by the following parameters: the Z' mass $m_{Z'}$, the Z' couplings to visible and dark
622 quarks g_q and g_{q_D} , the number of dark colors and flavors, the characteristic scale of the dark sector
623 confinement Λ_D , the mass scale of the dark hadrons m_D , and the average fraction of stable hadrons
624 in the decay R_{inv} . The coupling to SM quarks determines the Z' production cross section.

625

Part II

626

Experiment

Chapter 3: The Large Hadron Collider

629 The Large Hadron Collider (LHC) is a 26.7 km circular high-energy particle accelerator, span-
 630 ning the Swiss-French border near the city of Geneva, Switzerland [23]. The LHC occupies the
 631 tunnel constructed in 1989 for the Large Electron-Positron (LEP) Collider, and reaches a maxi-
 632 mum depth of 170m below the surface. The LHC is operated by the European Organization for
 633 Nuclear Research (CERN), the largest international scientific collaboration in the world.

634 The LHC accelerates protons and heavy ions, and collides them at four interaction points
 635 around the ring, with a design center-of-mass energy per collision of $\sqrt{s} = 14$ TeV. Each interaction
 636 point is home to one of four detector experiments, which study the products of the collisions. The
 637 largest of these experiments is the ATLAS detector, a general purpose detector designed to study
 638 the Standard Model and search for new physics that could be produced in LHC collisions [24].
 639 The CMS detector is another general purpose detector, designed and operated independently of the
 640 ATLAS detector, but intended to probe the same range of physics [25]. The ALICE experiment is
 641 a dedicated heavy ion experiment, and the LHC-b experiment is a dedicated *b*-physics experiment
 642 [26] [27].

643 This chapter will cover the multi-component accelerator complex powering the LHC, the state-
 644 of-the-art magnets which steer the particle beams, measurements of the intensity and number of
 645 collisions produced by the LHC, and finally an overview of LHC activities in the past, present, and
 646 future.

647 **3.1 Accelerator Physics**

648 **3.1.1 The Journey of a Proton**

649 From 2010 - 2018, the protons which fed the LHC started as hydrogen gas. The electrons were
650 removed from the hydrogen atoms through the use of strong electric fields. The linear accelerator
651 LINAC2 then accelerated the protons to an energy of 50 MeV. Between 2018 and 2020, LINAC2
652 was replaced with LINAC4, which instead accelerates H^- ions, hydrogen atoms with two electrons.
653 LINAC4 is capable of accelerating the H^- ions to 160 MeV. Before injection to the next part of
654 the acceleration chain, both electrons are stripped from the H^- ions, leaving just protons. From
655 here the protons enter the Proton Synchrotron booster, where they are accelerated up to 1.4 GeV of
656 energy. Subsequently they are sorted into bunches separated in time by 25 ns, where each bunch
657 contains approximately 10^{11} protons. Next the bunches pass through the Proton Synchrotron (PS)
658 and the Super Proton Synchrotron (SPS), where they reach energies of 25 GeV and 450 GeV
659 respectively. Finally they are injected into the LHC as two beams traveling in opposite direction.
660 The original design allowed each beam to be accelerated up to 7 TeV of energy. Due to limitations
661 in the performance of the superconducting LHC magnets, the highest energy actually achieved by
662 the LHC beams during Run 2 was 6.5 TeV, giving a collision center-of-mass energy of $\sqrt{s} = 13$
663 TeV [28]. Figure 3.1 shows the full LHC accelerator complex.

664 Acceleration in the LHC is performed by eight radio frequency (RF) cavities located around the
665 ring. Each RF cavity produces a 2 MV electric field oscillating at 40 MHz. The 40MHz oscillation
666 produces a point of stable equilibrium every 2.5 ns. These points of equilibrium are synchronized
667 with the occurrence of the proton bunches produced in the PS – a proton bunch occupies one out
668 of every ten points of stable equilibrium, such that the bunches maintain a 25 ns spacing [28].

669

The CERN accelerator complex Complexe des accélérateurs du CERN

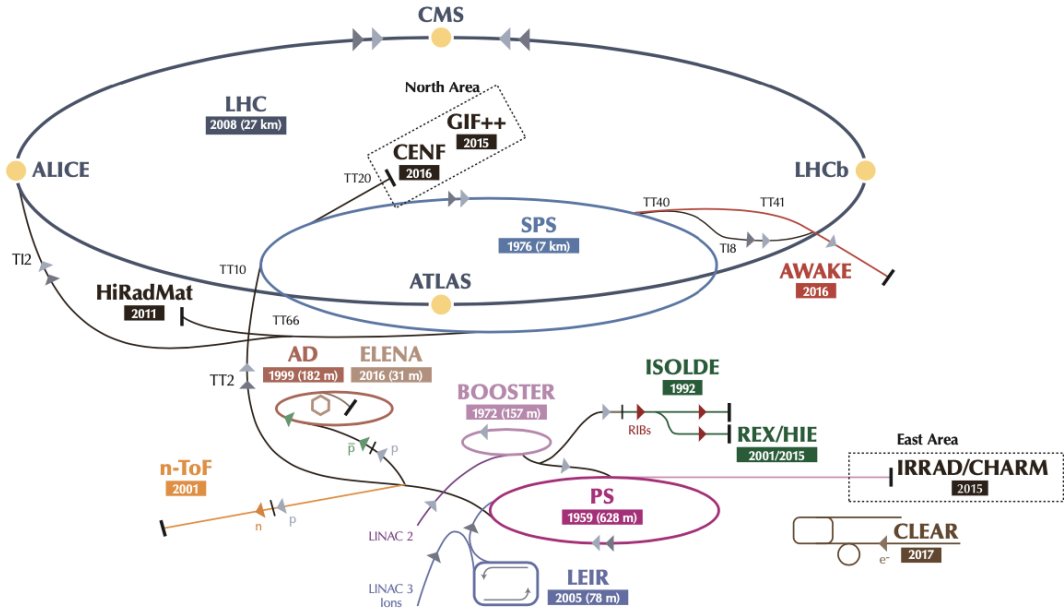


Figure 3.1: The LHC accelerator complex at CERN [29]

670 3.1.2 Magnets

671 In addition to the acceleration cavities, the LHC houses 9593 superconducting magnets which
 672 direct and focus the proton beam on its 27 kilometer journey. The magnets are comprised of super-
 673 conducting Niobium-Titanium coils cooled to 1.9K by superfluid helium. As the beams approach
 674 one of the four collision points around the ring, multipole magnets focus and squeeze the beam for
 675 optimal collisions [28].

676 The LHC is divided into sections, where each section contains an arc and a straight insertion. The arcs are composed of 1232 large dipole magnets which bend the beam
 677 to follow the roughly circular 27 km path. The main dipoles generate powerful 8.3 tesla magnetic
 678 fields to achieve this bend. Each dipole magnet is 15 meters long and weighs 35 tonnes. The
 680 dipoles work in conjunction with quadrupole magnets, which keep the particles in a focused beam,
 681 and smaller sextupole, octupole and decapole magnets which tune the magnetic field at the ends of
 682 the dipole magnets [30].

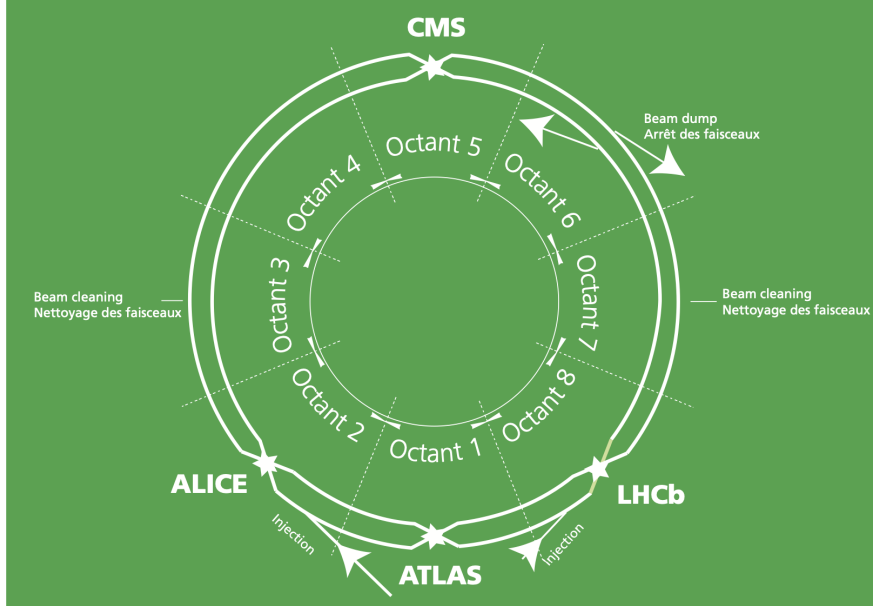


Figure 3.2: The octants of the LHC and location of various beam activities [28]. Stars indicate the locations of beam collisions, and the associated detectors recording the outcome of those collisions.

683 The straight insertion sections have different purposes depending on their location around the
 684 ring: beam collisions, beam injection, beam dumping, or beam cleaning. At the four collision
 685 points, insertion magnets squeeze the beam to ensure a highly focused collision. This is accom-
 686 plished with a triplet of quadrupole magnets, which tighten the beam from 0.2 millimeters to just
 687 16 micrometers in diameter. Insertion magnets also clean the beam, which prevents stray particles
 688 from hitting sensitive components throughout the LHC. When the LHC is ready to dispose of a
 689 beam of particles, beam dump magnets deflect the path of the beam into a straight line towards
 690 a block of concrete and graphite that stops the beam. A dilution magnet then reduces the beam
 691 intensity by a factor of 100,000 before the final stop [30]. Figure 3.2 shows the locations various
 692 beam activities.

693 3.2 Luminosity

694 Collisions at the LHC occur when the two beams of proton bunches cross at one of the four
 695 interaction points. The intensity of collisions is described by the instantaneous luminosity, the

696 formula for which is given in equation 3.1.

$$L = \frac{fN_1N_2}{4\pi\sigma_x\sigma_y} \quad (3.1)$$

697 Here f is the revolution frequency, N_1 and N_2 are the number of particle per bunch for each
698 beam, and σ_x , σ_y are the horizontal and vertical beam widths.

699 The instantaneous luminosity gives the number of the collisions that could be produced at the
700 interaction point per unit of cross-sectional area per unit of time, generally expressed in $\text{cm}^{-2}\text{s}^{-1}$.
701 The integrated luminosity is obtained by integrating the instantaneous luminosity over a given
702 block of time, and measures the total number of collisions which have occurred during that op-
703 eration period. The total integrated luminosity is directly correlated with the size of the datasets
704 collected by the LHC experiments. Total integrated luminosity for Run 2 is illustrated in Figure
705 3.3.

706 High levels of instantaneous luminosity result in multiple pp collisions per bunch crossing,
707 which leads to an effect known as *pileup*. Pileup poses a challenge for detector physics, as recon-
708 structing the products of multiple simultaneous events is far more challenging than reconstructing
709 a single event with no pileup. Pileup conditions vary from year-to-year and run-to-run of LHC op-
710 eration, and the impact of these conditions are taken into account when analyzing the data, as will
711 be discussed further in Chapter 5. Measurement of pileup conditions during Run 2 are illustrated
712 in Figure 3.3.

713 The design peak luminosity of the LHC is $1.0 \times 10^{34} \text{ cm}^{-2}\text{s}^{-1}$. During Run 1 of the LHC the
714 peak instantaneous luminosity was $0.8 \times 10^{34} \text{ cm}^{-2}\text{s}^{-1}$. Over the course of Run 1 the LHC collected
715 a total integrated luminosity of 5.46 fb^{-1} at $\sqrt{s} = 7 \text{ TeV}$, and 22.8 fb^{-1} at $\sqrt{s} = 8 \text{ TeV}$. Following the
716 first long shutdown and upgrade phase of operations, the LHC achieved a center of mass energy
717 $\sqrt{s} = 13 \text{ TeV}$ at the beginning of Run 2 in 2015. The LHC was also able to deliver 2.0×10^{34}
718 $\text{cm}^{-2}\text{s}^{-1}$ peak instantaneous luminosity, double the design value. During LHC Run 2, from 2015-
719 2018, the LHC delivered 156 fb^{-1} of integrated luminosity for proton-proton collisions. Run 3 of

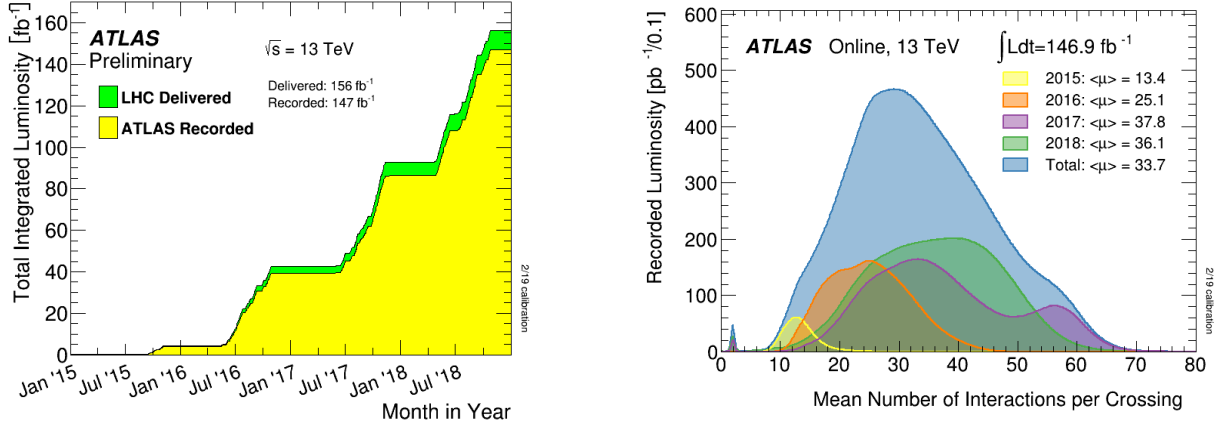


Figure 3.3: (Left) Total integrated luminosity over the course of Run 2. (Right) Average number of pp interactions per bunch crossing in Run 2. Each curve is weighted by the integrated luminosity for the year.

720 the LHC began in 2022, and is expected to deliver 250 fb^{-1} of integrated luminosity to the ATLAS
721 and CMS experiments by 2026 [31].

722 The goal of LHC physic analyses is to find and study rare events produced by interesting
723 physics processes. The cross section σ of a given process indicates the probability of that process
724 occurring given the beam conditions of the LHC. Multiplying the cross section by the integrated
725 luminosity of a dataset gives the expected number of events for that process within the dataset.

$$N_{\text{events}} = \int \sigma L(t) dt = \mathcal{L} \times \sigma \quad (3.2)$$

726 The cross section for most processes of interest, especially BSM processes, is several orders of
727 magnitude below the total cross section for the LHC. Therefore maximizing the number of events
728 produced in collisions is crucial to increase the likelihood of producing events from processes of
729 interest. For this reason, maximizing instantaneous luminosity is a key factor in accelerator design
730 and operation, while mitigating the resulting pileup effects is a key component in detector design
731 and operation.

732 **3.3 LHC Timeline**

733 The first proton-proton collisions at the LHC were achieved in 2010 with a center-of-mass
734 energy of $\sqrt{s} = 7$ TeV. Run 1 of the LHC took place between 2010 and early 2013, during which
735 time the center-of-mass collision energy increased from 7 TeV to 8 TeV. Figure 3.4 shows an
736 overview of LHC activities beginning in 2011, in the midst of Run 1. The data collected during
737 Run 1 led to the discovery of the Higgs Boston in 2012 [32].

738 Between 2013 and 2015 the LHC underwent the first Long Shutdown (LS1) during which
739 time maintenance and renovation was performed on the accelerator chain, including the repair and
740 consolidation of the high-current splices which connect the super-conducting LHC magnets. Run
741 2 of the LHC took place from 2015 to 2018 and achieved a center-of-mass energy of $\sqrt{s} = 13$ TeV.
742 Analysis of data collected in Run 2 is still on going, and is the subject of study in this thesis.

743 Between 2018 and 2022 the LHC underwent the second Long Shutdown (LS2), allowing for
744 further detector and accelerator maintenance and upgrades. Key improvements to the LHC in-
745 cluded the improvement of the insulation for over 1200 diode magnets, and the upgrade from
746 LINAC2 to LINAC4 mentioned in Section 3.1.1. Run 3 of the LHC began in 2022 and achieved a
747 center-of-mass energy of $\sqrt{s} = 13.6$ TeV.

748 Run 3 is scheduled to continue through 2026, at which point the LHC machine and detectors
749 will undergo upgrades for the *high luminosity* LHC (HL-LHC). The HL-LHC will increase the
750 instantaneous machine luminosity by a factor of 5 - 7.5 with respect to the nominal LHC design.
751 The bottom panel of Figure 3.4 shows an overview of the preparation work for the HL-LHC that
752 has been going on concurrently with Run 1, 2, and 3 of the LHC [33].



Figure 3.4: Timeline of LHC and HL-LHC activities [31]. Integrated luminosity estimates are approximate, and not reflective of the exact amount delivered to each experiment.

Chapter 4: The ATLAS Detector

755 The ATLAS detector (**A** Toroidal **L**H**C** Apparatu**S**) is one of two general purpose physics
 756 detectors designed to study the products of proton-proton collisions at the LHC. The detector is
 757 composed of a variety of specialized subsystems, designed to fully capture a wide array of physics
 758 processes. A diagram of the detector is shown in Figure 4.1 The apparatus is 25m high, 44m in
 759 length, and weighs over 7000 tons [34]. The LHC beam pipes direct proton beams to an interaction
 760 point at the center of ATLAS, and the cylindrical detector design captures a complete 360° view
 761 of the *event*¹, tracking all particles that result from the collision.

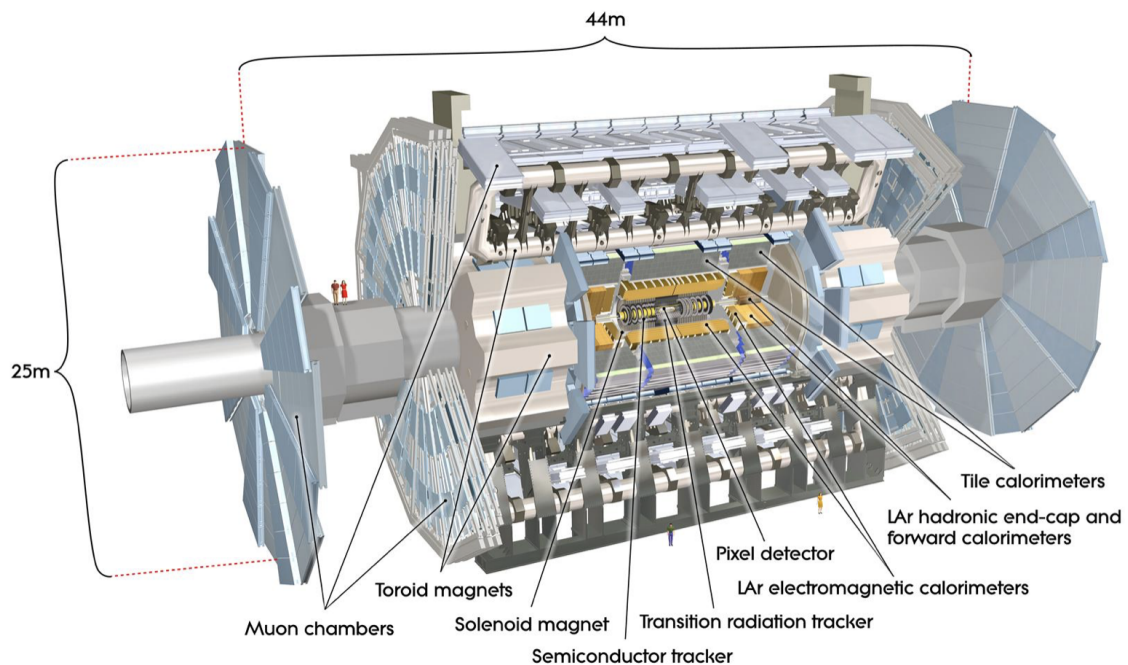


Figure 4.1: The ATLAS detector [34].

¹An ATLAS event is a snapshot of all the measurements associated to a given $p p$ collision

762 The main components of the ATLAS detector are the Inner Detector (ID) which provides high
 763 precision tracking of charged particles leaving the collision vertex, the calorimeter system which
 764 measures the energy of electromagnetic and hadronic objects, and the Muon Spectrometer (MS)
 765 which gives detailed information about muons that reach the outer radii of the detector. A summary
 766 of the resolution and angular coverage of each of these systems is presented in Table 4.1. Two
 767 magnet systems, a 2 T solenoid magnet surrounding the ID, and a 0.5-1.0 T toroid magnet system
 768 situated throughout the MS, produce magnetic fields which bend the trajectory of charged particles
 769 traversing the detector. In addition to the main detector components, dedicated forward detectors
 770 monitor beam conditions and instantaneous luminosity, and an online trigger system reduces the
 771 data rate to a manageable level for storage. Each of these components will be discussed in further
 772 detail in this chapter.

Detector component	Required resolution	η coverage	
		Measurement	Trigger
Tracking	$\sigma_{p_T}/p_T = 0.05\% p_T \oplus 1\%$	± 2.5	
EM calorimetry	$\sigma_E/E = 10\%/\sqrt{E} \oplus 0.7\%$	± 3.2	± 2.5
Hadronic calorimetry (jets)			
barrel and end-cap	$\sigma_E/E = 50\%/\sqrt{E} \oplus 3\%$	± 3.2	± 3.2
forward	$\sigma_E/E = 100\%/\sqrt{E} \oplus 10\%$	$3.1 < \eta < 4.9$	$3.1 < \eta < 4.9$
Muon spectrometer	$\sigma_{p_T}/p_T = 10\% \text{ at } p_T = 1 \text{ TeV}$	± 2.7	± 2.4

Table 4.1: General performance goals of the ATLAS detector [34].

773 4.1 Coordinate System and Geometry

774 The ATLAS detector employs a right hand cylindrical coordinate system. The z axis is aligned
 775 with the beam line, and the $x - y$ plane sits perpendicular to the beam line. The coordinate system
 776 origin is centered on the detector, such that the origin corresponds with the interaction point of the
 777 two colliding beams. The detector geometry is usually characterized by polar coordinates, where
 778 the azimuthal angle ϕ spans the $x - y$ plane. The polar angle θ represents the angle away from the
 779 beam line, or z axis. $\theta = 0$ aligns with the positive z axis, and $\phi = 0$ aligns with the positive x axis.

780 The polar coordinate θ is generally replaced by the Lorentz invariant quantity *rapidity* or y :

$$y = \frac{1}{2} \ln\left(\frac{E + p_z}{E - p_z}\right). \quad (4.1)$$

781 This substitution is advantageous because objects in the detector are traveling at highly rela-
782 tivistic speeds. The relativistic speed also means that the masses of the particles are generally small
783 compared to their total energy. In the limit of zero mass, the rapidity y reduces to the pseudorapid-
784 ity η , which can be calculated directly from the polar angle θ :

$$\eta = -\ln\left(\frac{\theta}{2}\right). \quad (4.2)$$

785 The distance between physics objects in the detector is generally expressed in terms of the solid
786 angle between them ΔR :

$$\Delta R = \sqrt{\Delta\phi^2 + \Delta\eta^2} \quad (4.3)$$

787 Figure 4.2a depicts the orientation of the coordinate system with respect to the ATLAS detector,
788 while Figure 4.2b illustrates the relationship between θ , η , and the beamline axis z . Direct or “head
789 on” proton-proton collisions are more likely to result in objects whose momentum is directed
790 along transverse plane (low $|\eta|$); glancing proton-proton collisions are more likely to result in
791 objects whose momentum is directed along the z -axis (high $|\eta|$). Due to the difference in the
792 nature of these collisions, as well as the cylindrical design of the ATLAS detector, the detector
793 is divided into regions of low and high $|\eta|$. Each subsystem has a “central” or “barrel” region
794 covering low $|\eta|$, while the “forward” or “end-cap” regions cover the area up to $|\eta| = 4.9$. Each of
795 the three main ATLAS subsystems will be discussed in the following sections.

796 **4.2 Inner Detector**

797 The Inner Detector (ID) is the ATLAS subsystem closest to the interaction point. The primary
798 purpose of the ID is to determine the charge, momentum, and trajectory of charged particles pass-

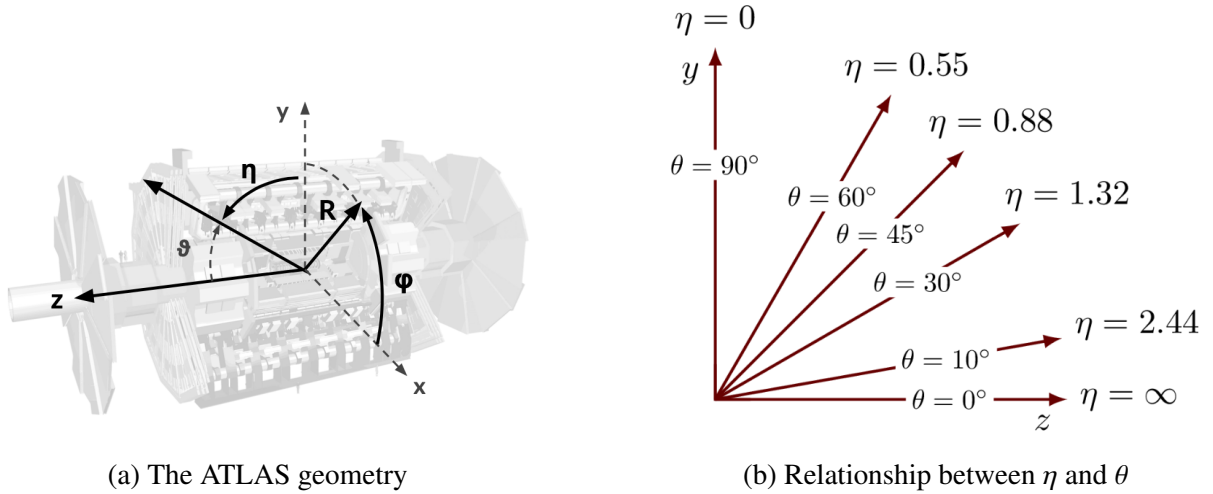


Figure 4.2: ATLAS coordinate system and geometry

799 ing through the detector. With this information the ID is also able to precisely determine interaction
 800 vertices.

801 The ID is composed of three sub-detectors; the Pixel Detector, the Semiconductor Tracker
 802 (SCT) and the Transition Radiation Tracker (TRT) [34]. Figure 4.3 shows the location of these
 803 three subsystems with respect to each other and the interaction point.

804 4.2.1 Pixel Detector

805 The pixel detector is the first detector encountered by particles produced in LHC collisions.
 806 The original pixel detector consists of 3 barrel layers of silicon pixels, positioned at 5 cm, 9 cm
 807 and 12 cm from the beamline. There are also 3 disks on each end-cap positioned 50 - 65 cm
 808 from the interaction point, providing full coverage for $|\eta| < 2.2$. Figure 4.4 illustrates the end-cap
 809 geometry for the ID. The layers are comprised of silicon pixels each measuring $50 \times 400 \mu\text{m}^2$,
 810 with 140 million pixels in total. The pixels are organized into modules, which each contain a set
 811 of radiation hard readout electronics chips. In 2014, the Insertable B-layer (IBL) was installed,
 812 creating a new innermost layer of the pixel detector sitting just 3.3 cm from the beamline. The
 813 pixels of the IBL measure $50 \mu\text{m}$ by $250 \mu\text{m}$, and cover a pseudo-rapidity range up to $|\eta| < 3$.
 814 The IBL upgrade enhances the pixel detector's ability to reconstruct secondary vertices associated

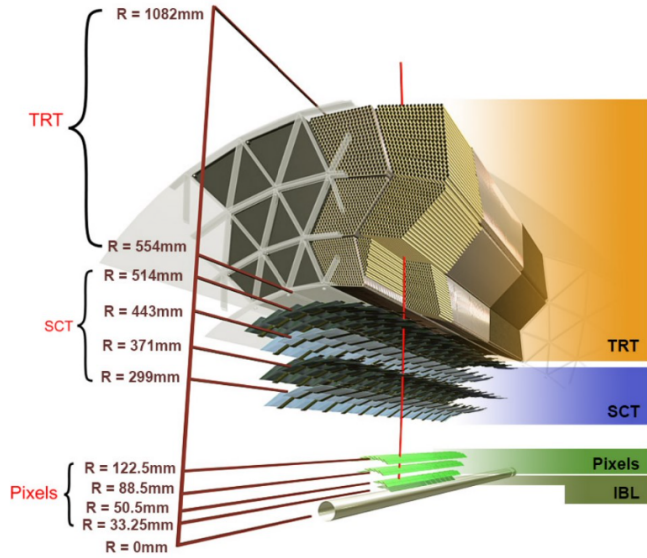


Figure 4.3: A 3D visualization of the structure of the ID in the barrel region [35]

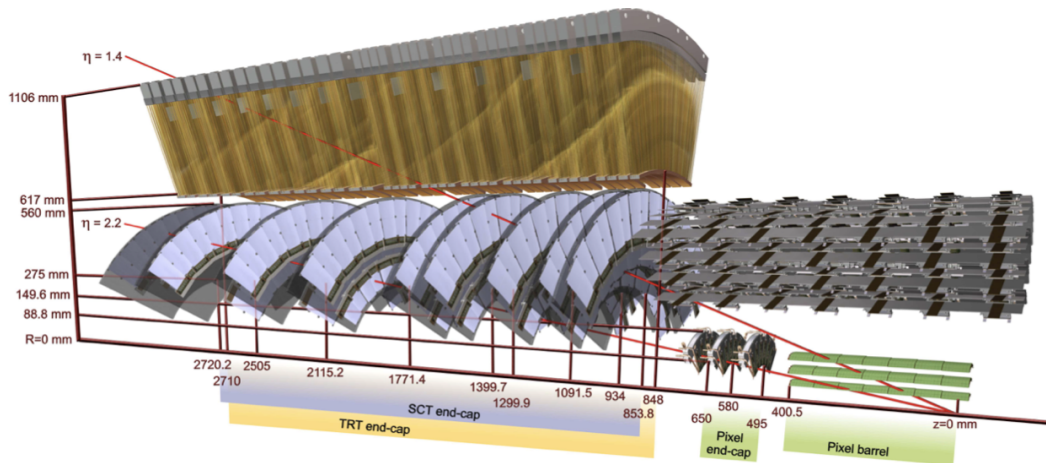


Figure 4.4: A 3D visualization of the structure of the ID end-caps [34]. The paths of two charged particles ($\eta = 1.4$ and 2.2) are illustrated.

815 with short-lived particles such as the b-quark. The improved vertex identification also helped
816 compensate for increasing pile-up in Run 2.

817 **4.2.2 Semiconductor Tracker**

818 The SCT provides at least 4 additional measurements of each charged particle. It employs the
819 same silicon technology as the Pixel Detector, but utilizes larger silicon strips which measure 80
820 μm by 12.4 cm. The SCT is composed of 4 barrel layers, located between 30 cm and 52 cm from
821 the beamline, and 9 end-cap layers on each side. The SCT can distinguish tracks that are separated
822 by at least 200 μm .

823 **4.2.3 Transition Radiation Tracker**

824 The TRT provides an additional 36 hits per particle track. The detector relies on gas filled
825 straw tubes, a technology which is intrinsically radiation hard. The straws which are each 4 mm in
826 diameter and up to 150 cm in length and filled with xenon gas. The detector is composed of about
827 50,000 barrel region straws and 640,000 end-cap straws, comprising 420,000 electronic readout
828 channels. Each channel provides a drift time measurement with a spatial resolution of 170 μm per
829 straw. As charged particles pass through the many layers of the detector, transition radiation is
830 emitted. The use of two different drift time thresholds allows the detector to distinguish between
831 tracking hits and transition radiation hits.

832 **4.3 Calorimeters**

833 The ATLAS calorimeter system is responsible for measuring the energy of electromagnetically
834 interacting and hadronically interacting particles passing through the detector. The calorimeters are
835 located just outside the central solenoid magnet, which encloses the inner detectors. The calorime-
836 ters also stop most known particles, which the exception of muons and neutrinos, preventing them
837 from traveling to the outermost layers of the detector. The ATLAS calorimetry system is composed
838 of two subsystems - the Liquid Argon (LAr) calorimeter for electromagnetic calorimetry and the

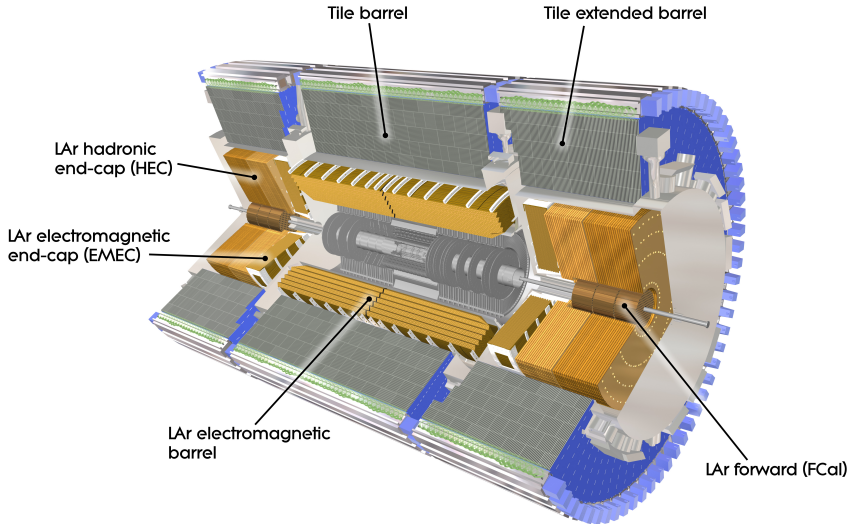


Figure 4.5: ATLAS calorimetry system [36]

839 Tile calorimeter for hadronic calorimetry. The full calorimetry system is shown in Figure 4.5.

840 4.3.1 Liquid Argon Calorimeter

841 The LAr calorimeter is a sampling calorimeter designed to trigger on and measure the ener-
 842 gies of electromagnetic (EM) particles, as well as hadronic particles in the high $|\eta|$ regions [37].
 843 It is divided in several regions, as shown in Figure 4.5. For the region $|\eta| < 1.4$, the electro-
 844 magnetic barrel (EMB) is responsible for EM calorimetry, and provides high resolution energy,
 845 timing, and position measurements for electrons and photons passing through the detector. The
 846 electromagnetic end-cap (EMEC) provides additional EM calorimetry up to $|\eta| < 3.2$. In the
 847 region $1.4 < |\eta| < 3.2$, the hadronic end-cap (HEC) provides hadronic calorimetry. For hadronic
 848 calorimetry in the region $|\eta| < 1.4$, corresponding to a detector radii > 2.2 m, the less expensive
 849 tile calorimeter (discussed in the next section) is used instead. A forward calorimeter (FCAL)
 850 extends the hadronic calorimetry coverage up to $3.1 < |\eta| < 4.9$.

851 The LAr calorimeter is composed of liquid argon sandwiched between layers of absorber mate-
 852 rial and electrodes. Liquid argon is advantageous as a calorimeter active medium due to its natural
 853 abundance and low cost, chemical stability, radiation tolerance, and linear response over a large

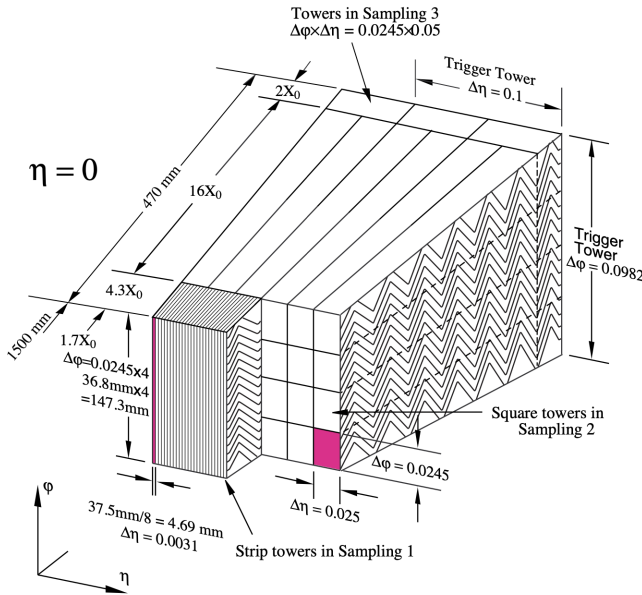


Figure 4.6: Diagram of a segment of the EMB, demonstrating the accordion plate arrangement and the cell segmentation pattern [37]. Three layers are illustrated, and the variation in the cell granularity between the front layer (Sampling Layer 1) and the back layer (Sampling Layer 3) is shown.

854 energy range [38]. The calorimeter is cooled to 87k by three cryostats: one barrel cryostat encom-
 855 passing the EMB, and two end-cap cryostats. The barrel cryostat also encloses the solenoid which
 856 produces the 2T magnetic field for the inner detector. Front-end electronics are housed outside the
 857 cryostats and are used to process, temporarily store, and transfer the calorimeter signals.

858 Electromagnetic Calorimeter

859 For the electromagnetic calorimeters, the layers of electrodes and absorber materials are ar-
 860 ranged in an accordion shape, as illustrated in Figure 4.6. The detector is divided into $\eta - \phi$ regions
 861 or *cells*, which are each read out independently. The The accordion shape ensures that each half
 862 barrel is continuous in the azimuthal angle, which is a key feature for ensuring consistent high
 863 resolution measurements. Liquid argon permeates the space between the lead absorber plates, and
 864 a multilayer copper-polymide readout board runs through the center of the liquid argon filled gap.

865 The detection principle for the LAr calorimeter is the current created by electrons which are

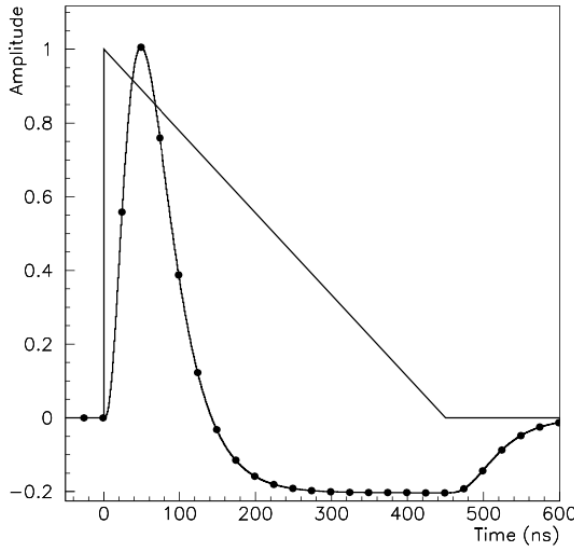


Figure 4.7: A LAr pulse as produced in the detector (triangle) and after shaping (curve) [37]

released when a charged particle ionizes the liquid argon. In the barrel region, the electrons are driven towards the center electrodes by a 2,000 V potential with a drift time of less than 450 ns [39]. In the end-caps the voltage varies as a function of the radius in order to maintain a flat response [37]. The amount of current produced by the ionized electrons is proportional to the energy of the particle creating the signal. Figure 4.7 shows the shape of the signal produced in the LAr calorimeter, before and after it undergoes shaping during the readout process. The shaping of the pulse enforces a positive peak and a negative tail, which ensures that subsequent pulses can be separated with the precision required for the 25 ns LHC bunch spacing.

Hadronic End-cap Calorimeter

The HEC sits radially beyond the EMEC. The copper absorber plates in the HEC are oriented perpendicular to the beamline, with LAr as the active medium. Each end-cap is divided into two independent wheels; the inner wheel uses 25 mm copper plates, while the outer wheel uses 50 mm plates as a cost saving measure. In each wheel, the 8.5 mm plate gap is crossed by three parallel electrodes, creating an effective drift distance of 1.8 mm. This gap is illustrated in Figure 4.8. Each wheel is divided into 32 wedge-shaped modules, each containing their own set of readout

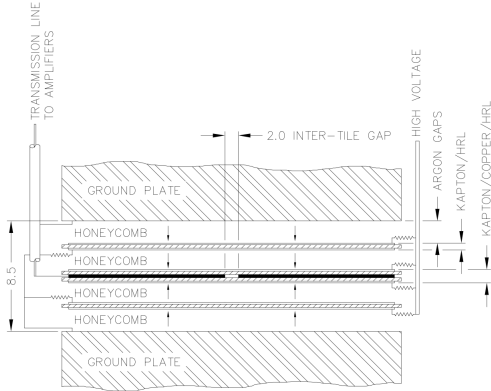


Figure 4.8: Readout gap structure in HEC [37]

881 electronics.

882 Forward Calorimeter

883 The forward range ($3.1 < |\eta| < 4.9$) is covered by the FCal, which provides both EM and
 884 hadronic calorimetry. It is composed of three active cylindrical modules; one EM module with
 885 copper absorber plates, and two hadronic modules with tungsten absorber plates [37]. The plates
 886 are oriented perpendicular to the beamline, and LAr is used as the active material throughout. The
 887 electrodes of the FCal consist of tubes that run parallel to the beam line, arranged in a honeycomb
 888 pattern. The resulting LAr gaps are as small as $250 \mu\text{m}$, which enables the FCal to handle the high
 889 particle flux in the forward region.

890 4.3.2 Tile Calorimeter

891 The Tile Calorimeter (TileCal) provides hadronic calorimetry in the region $|\eta| < 1.7$, and sur-
 892 rounds the LAr calorimeter. It is responsible for measurements of jet energy and jet substructure,
 893 and also plays an important role in electron isolation and triggering (including muons) [40]. Tile-
 894 Cal is composed of 3 sections, as shown in Figure 4.5; a barrel calorimeter sits directly outside the
 895 LAr EMB and provides coverage up to $|\eta| < 1.0$. Two extended barrel sections sit outside the LAr
 896 end-caps and cover the region $0.8 < |\eta| < 1.7$.

897 TileCal is a sampling calorimeter composed of steel and plastic scintillator plates as illustrated

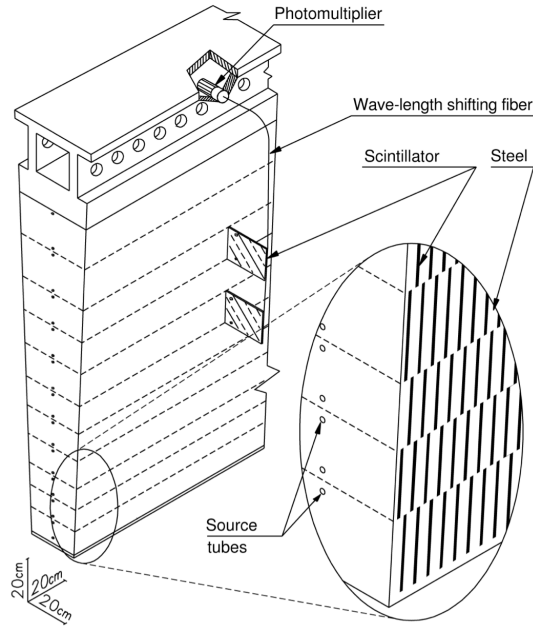


Figure 4.9: TileCal wedge module [40]

in Figure 4.9. A total of 460,000 scintillators are read out by wavelength-shifting fibers. The fibers are gathered to define cells and in turn read out by photomultiplier tubes, which amplify the scintillation light and convert it to an electrical signal. Each cell has an approximate granularity of $\Delta\eta \times \Delta\phi = 0.1 \times 0.1$. Each barrel is divided azimuthally into 64 independent modules, an example of which is show in Figure 4.9. The modules are each serviced by front-end electronic housed in a water-cooled drawer on the exterior of the module.

The detection principle of the TileCal is the production of light from hadronic particles interacting with the scintillating tiles. When a hadronic particle hits the steel plate, a shower of particles are produced. The interaction of the shower with the plastic scintillator produces photons, the number and intensity of which are proportional to the original particle's energy.

908

909 4.4 Muon Spectrometer

910 Unlike electrons, photons, and hadrons, muons interact minimally with the ATLAS calorimeters, and can pass through large amounts of detector material without stopping. The ATLAS Muon

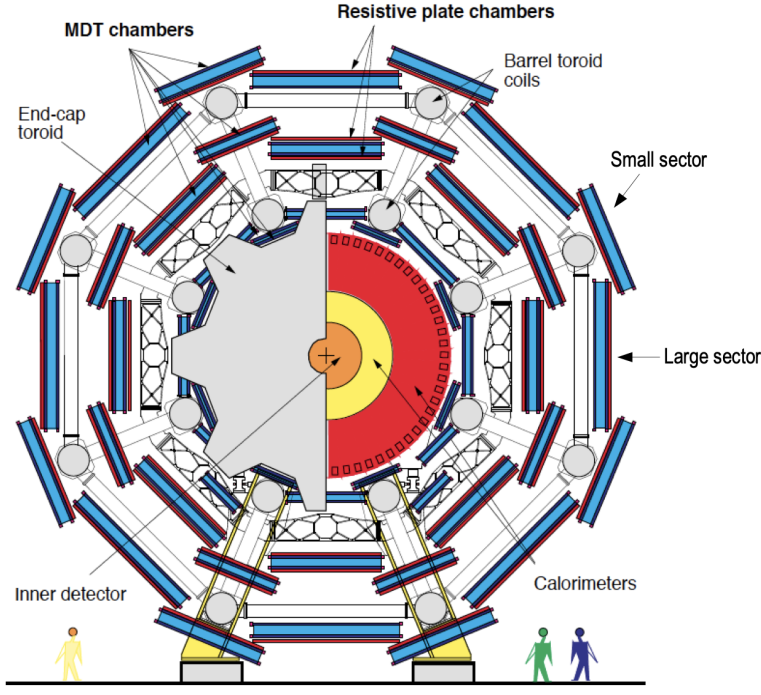


Figure 4.10: Cross section view of the muon spectrometer system [41]

912 Spectrometer (MS) provides additional tracking information to improve the identification and mea-
 913 surement of muons [41]. The MS comprises the outermost layers of the detector, and is interspersed
 914 with toroid magnets (discussed in Section 4.5), which provide a magnetic field of approximately
 915 0.5 T. The magnetic field bends the trajectory of the muons as they pass through the detector, and
 916 the degree of the bend is directly correlated with the muon momentum. The path of the muon is
 917 primarily measured by hits in three layers of Monitored Drift Tube (MDT) precision chambers,
 918 which cover the range $|\eta| < 2.7$. The barrel layout of the MS is shown in Figure 4.10.

919 Muon triggering is provided by three layers of Resistive Plate Chambers (RPC) in the barrel
 920 ($|\eta| < 1.05$), and 3 - 4 layers of Thin Gap Chambers (TGC) in the end-caps ($1.05 < |\eta| < 2.4$).
 921 RPCs and TGCs also provide muon track measurements in the non-bending coordinate (ϕ). RPCs
 922 are constructed from two parallel resistive plates separated by a 2mm gap filled with a sensitive
 923 gas mixture. This provides a total of six independent measurements for each muon track, with a
 924 spatial resolution of ~ 1 cm and a time resolution of ~ 1 ns. Time measurements from the RPCs
 925 are primarily associated to hits in the MDT precision chambers to determine the bunch crossing.

926 The time measurement is also used to reject cosmic muons, and to search for delayed signals.
927 TCGs provide triggering in the end-cap regions, and consist of parallel 30 μm wires suspended
928 in a sensitive gas mixture. TCGs provide high radiation tolerance and a fast response time, both
929 features that are necessary for handling the high flux of muons in the forward region.

930 Precision measurements of muon momentum and position are primarily achieved by MDTs.
931 The MDTs are constructed from 30 mm diameter tubes, permeated by a gas mixture of 93% Ar
932 and 7% CO₂ [42]. The average single-tube spatial resolution is 80 μm . Each chamber consists
933 of six drift tube layers, which together provide a muon track segment resolution of 35 μm . The
934 momentum of the muons can be calculated from the bend in the muon trajectory as they pass
935 through the 0.5T magnetic field provided by the toroids. For a $p_T = 1$ TeV track, the average
936 p_T resolution is 11%. In the inner most end-cap wheels, Cathode Strip Chambers (CSC) are
937 used instead of MDTs, covering the region $2.0 < |\eta| < 2.7$. CSCs are multi-wire proportional
938 chambers, with a cathode strip readout. The CSCs have a spatial resolution in the range of 50 μm ,
939 and a maximum drift time of about 30 ns, which makes them superior for handling the high flux of
940 particles in the forward region.

941 4.5 Magnet System

942 The ATLAS magnet system consists of four sets of superconducting magnets: a barrel solenoid,
943 a barrel toroid, and two end-cap toroids [43]. The solenoid magnet produces a 2T magnetic field
944 responsible for bending the trajectories of charged particles as they pass through the inner detector.
945 The three toroid magnets provide a field of 0.5 - 1 T and curve the path of muons passing through
946 the muon spectrometer.

947 The inner solenoid magnet is composed of over 9 km of niobium-titanium superconductor
948 wires, which are embedded into strengthened pure aluminum strips. The solenoid is just 4.5 cm
949 thick, which minimizes interactions between the magnet material and particles passing through the
950 detector. It is housed in the LAr cryostat, as described in section 4.3.1, which further reduces the
951 amount of non-detector material required to support the solenoid. The return yoke of the magnet

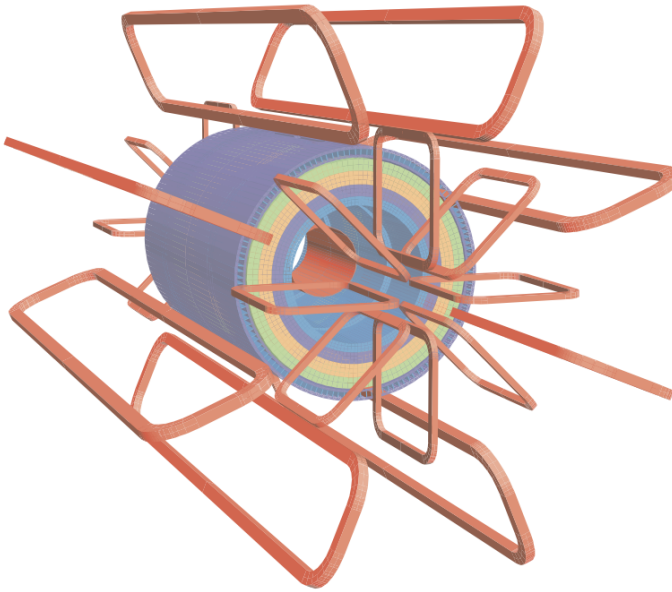


Figure 4.11: Layout of the barrel and end-cap toroid magnets [34]

952 is provided by the iron absorber of the TileCal.

953 The central ATLAS toroid magnet, providing the magnetic field for the barrel region of the
 954 MS, is the largest toroidal magnet ever constructed at 25.3 m in length [44]. The toroid is com-
 955 posed of eight individual coils, each housed in their own cryostat. The toroidal magnetic field is
 956 advantageous as the direction of the field is almost perpendicular to the path of the charged par-
 957 ticles. 56 km of aluminum stabilized niobium-titanium-copper superconductor wire compose the
 958 magnet. In each end-cap, eight smaller superconducting coils extend the toroidal magnetic field
 959 to particles leaving the detector in the forward direction [43]. Figure 4.11 shows the layout of the
 960 toroid magnets.

961 4.6 Forward Detectors

962 In addition to the inner detector, calorimeters, and muon spectrometer, three smaller detectors
 963 provide coverage in the very forward region. The innermost forward detector, at 17 m from the
 964 interaction point, is the **L**uminosity measurement using **C**erenkov **I**ntegrating **D**etector (LUCID).
 965 LUCID's primary purpose is to measure the relative online-luminosity for the ATLAS detector,

966 from inelastic $p - p$ scattering. The detector is composed of 20 aluminum Cerenkov tubes which
967 surround the beam pipe and face towards the interaction point.

968 The second forward detector is the Zero-Degree Calorimeter (ZDC), located 140 m from the
969 interaction point in both directions, at the point where the LHC beam-pipe divides into two separate
970 pipes. The ZDC's primary purpose is to detect forward neutrons from heavy ion collisions.

971 The third forward detector is the Absolute Luminosity For ATLAS (ALFA) system, located 240
972 m from the interaction point in both directions. ALFA determines luminosity by measuring elastic
973 scattering at small angles, from which luminosity can be calculated via the optical theorem. The
974 detector is built from scintillating fiber trackers. These are connected to the accelerator vacuum
975 via Roman pots, which allow the detector to come as close as 1mm to the beam without disrupting
976 the machine vacuum. The LUCID and ALFA detectors are crucial to determining the real-time
977 conditions of the beams and the total luminosity delivered to the ATLAS detector [34].

978 **4.7 Trigger and Data Acquisition**

979 The trigger and Data Acquisition systems (TDAQ) are responsible for selecting the most inter-
980 esting events to save for further downstream processing. Because of the high luminosities delivered
981 to the ATLAS detector, not all events recorded can be saved; the 40 MHz bunch crossing rate must
982 be reduced by 5 orders of magnitude to an event storage rate of ~ 1 kHz. The trigger system is
983 composed of three distinct levels: Level 1 (L1), Level 2 (L2) and the event filter [34]. Collectively
984 the L2 trigger and the event filter form the High Level Trigger (HLT).

985 The L1 trigger is implemented in the hardware of the ATLAS calorimeter and muon systems.
986 A block diagram of the L1 trigger is available in Figure 4.12. The primary modality of the L1 trig-
987 ger is to identify muons, electrons, photons, jets, and τ -leptons with high transverse momentum.
988 Particles with high transverse momentum are more likely to originate from direct, high energy
989 collisions, which are most likely to produce interesting physics processes. The L1 trigger also
990 identifies events with large missing transverse energy, which could be indicative of new physics.
991 The L1 muon trigger (L1Muon) relies on RPC and TGC trigger chambers in the barrel and end-

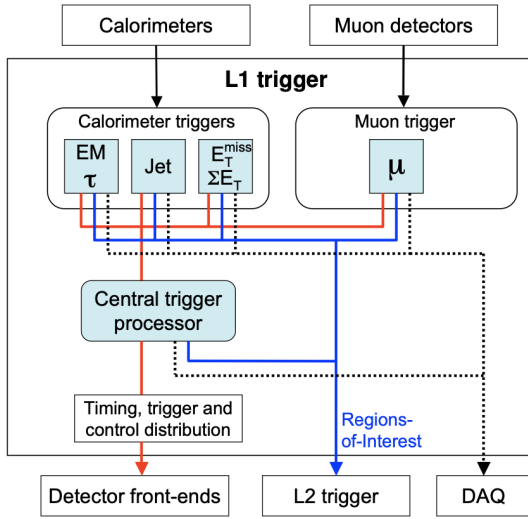


Figure 4.12: Block diagram of the L1 trigger process [34]. The overall L1 trigger decision is made by the CTP.

992 cap regions of the muon spectrometer. The L1 Calorimeter Trigger (L1Calo) uses reduced gran-
993 ularity information collected by all the calorimeter subsystems. Results from the L1Muon and
994 L1Calo triggers are combined by the Central Trigger Processor (CTP), which implements a trigger
995 ‘menu’, listing various combinations of trigger requirements. The maximum L1 acceptance rate
996 is 100 kHz, and the L1 trigger decision must reach the front-end electronics within 2.5 μ s of its
997 associated bunch-crossing.

998 The L1 trigger defines a Region-of-Interest (RoI) for each passing event. The ROI is repre-
999 sented by the η - ϕ detector region where interesting features were identified by the L1 selection
1000 process. Information about the type of feature identified and the threshold which was exceeded to
1001 trigger the L1 response is also recorded. The ROI data is sent to the L2 trigger, which uses all of
1002 the available information within the ROI at full granularity and precision. The L2 trigger reduces
1003 the event rate from 100 kHz to 3.5 kHz, with an average processing time of 40 ms. The final stage
1004 of the HLT is the event filter, which reduces the event rate to 200 Hz (<1 kHz). The event filter uses
1005 an offline analysis process to select fully rebuilt events which will be saved for further analysis. A
1006 diagram of the full ATLAS TDAQ system is shown in Figure 4.13.

1007 All levels of the ATLAS trigger system depend on specialized electronics. Each detector front-

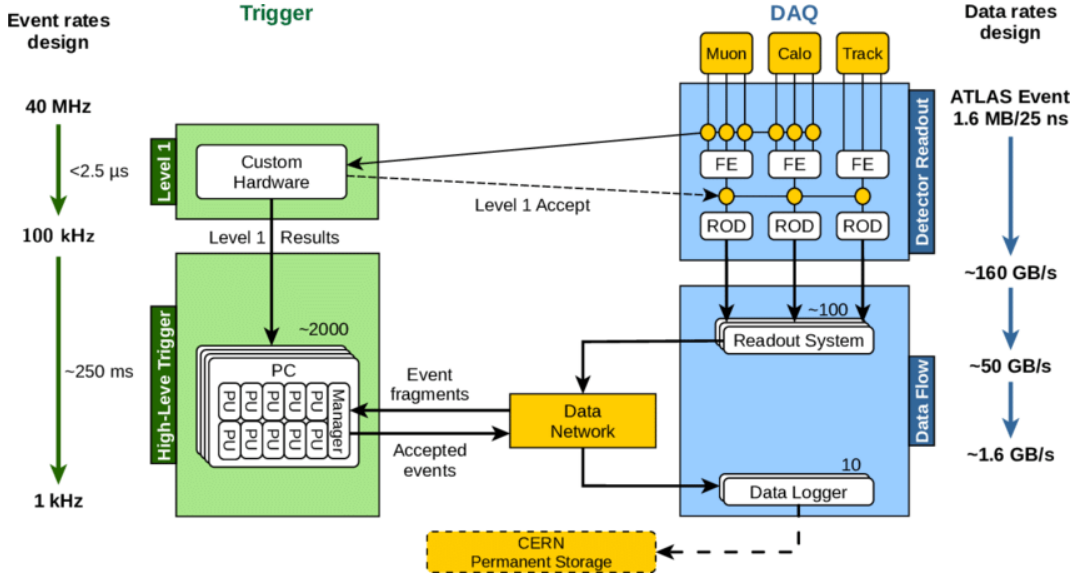


Figure 4.13: Block diagram of the trigger and data acquisition processes, including L1 and HLT processes [45].

1008 end system has a specialized Readout Driver (ROD) which collects information from several front-
 1009 end data streams at once. The ROD is composed of front-end analogue processing, a L1 buffer
 1010 which retains the information long enough for the L1 trigger decision, and dedicated links which
 1011 send the front-end L1 triggered data to Data Acquisition System (DAQ). Any digital signals are
 1012 formatted as raw data before being transferred to the DAQ. The first stage of the DAQ temporarily
 1013 stores the L1 data in local buffers. The ROI data is then requested by the L2 trigger, after which
 1014 selected events are transferred to an event building system, before events passing the event filter
 1015 are sent to the CERN computer center for permanent storage. The DAQ system not only allows
 1016 for the readout of detector data, but is also responsible for the monitoring and configuration of
 1017 the hardware and software components which make up the data readout system via the Detector
 1018 Control System (DCS).

1019 The DCS allows centralized control of all detector subsystems simultaneously. It continually
 1020 monitors operational conditions, reports any abnormal behavior to the operator, and can perform
 1021 both automatic and manual interventions. The DCS reports on real time detector conditions such
 1022 as high or low voltage detector electronics, gas and cooling systems, magnetic field conditions,
 1023 humidity and temperature. This information is continually monitored by experts in the ATLAS

1024 control room, so that action can be taken immediately to correct any issues that arise. The DCS also
1025 handles communication between detector systems, and other systems such as the LHC accelerator,
1026 the ATLAS magnets, and CERN technical services [34].

Chapter 5: Particle Reconstruction and Identification

1029 With a design luminosity of $1.0 \times 10^{34} \text{ cm}^{-2}\text{s}^{-1}$, and a peak Run 2 instantaneous luminosity of
 1030 $2.0 \times 10^{34} \text{ cm}^{-2}\text{s}^{-1}$, reconstructing and identifying the products of LHC $p p$ collisions is one of the
 1031 most complex tasks for each LHC experiment. The accurate reconstruction and identification of
 1032 *physics objects*¹ lays the ground work for all subsequent physics analyses, so it is also one of the
 1033 most fundamentally important tasks performed by an experiment.

1034 Reconstruction is the process of combining raw and uncalibrated hits across various subsystems
 1035 into unique objects. Two particular subsystems, the Inner Detector (ID) tracker and the calorime-
 1036 ters play particularly important roles and will be discussed in detail. Analysis of the properties of
 1037 the reconstructed objects identifies them as photon, electrons, muons, or jets. While photons, elec-
 1038 trons, and muons are fundamental particles, jets represent a collimated shower of many hadronic
 1039 particles, whose definition is more flexible. Jet reconstruction, clustering and track association are
 1040 all of particular import to jet identification, and to the later content of this thesis. Finally, recon-
 1041 struction also identifies *missing transverse energy* E_T^{miss} in events, which is a crucial variable for
 1042 BSM physics searches. Figure 5.1 shows how the physics objects listed here interact with various
 1043 systems in the ATLAS detector.

1044 **5.1 Inner Detector Tracks**

1045 As the inner most layer of the detector, the ID measures charged particles close to the interac-
 1046 tion point. The various hits of these charged particles throughout the ID are used to reconstruct
 1047 *tracks* which give the trajectories of charged particles [47]. Track reconstruction begins by clus-
 1048 tering hits in the Pixel and SCT detectors, and combining clusters from different radial layers of

¹A particle which has appeared in the ATLAS detector and whose properties have been estimated via the measurements left in various detector subsystems.

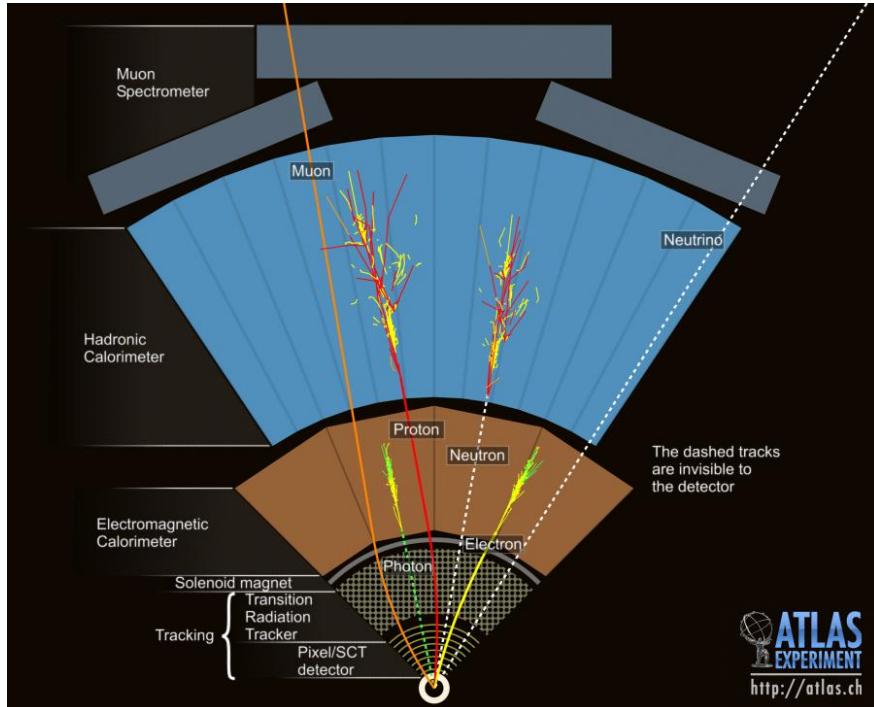


Figure 5.1: This graphic illustrates a slice of ATLAS detector barrel [46]. A photon, electron, and two jets (associated to the proton and neutron) are shown, illustrating each object's interaction with various ATLAS subsystems. The path of the charged particles is curved on account of the strong magnetic field produced by the solenoid and toroid magnets. A neutrino, generally representing the reconstruction of missing transverse energy, is also illustrated.

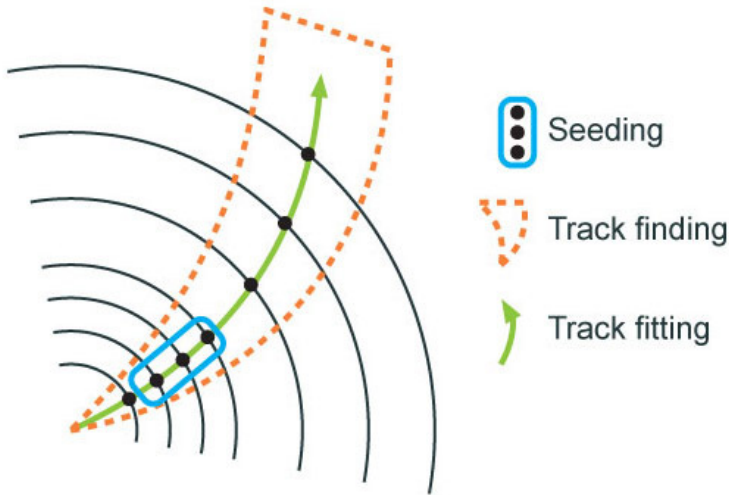


Figure 5.2: Track reconstruction seeding, finding and fitting illustration [47]

1049 these detectors. The multi-layer clusters form track *seeds*, which provide initial estimates of mea-
 1050 surements belonging to an individual track. The requirement of three points allows for a rough
 1051 estimate of the track p_T to be made by calculating the curvature of the track and accounting of the
 1052 magnetic field in the ID.

1053 Track seeds are subject to a variety of quality requirements, such as having a minimum esti-
 1054 mated p_T and passing interaction region compatibility criterion. If these requirements are satisfied,
 1055 the track seeds are passed to the track finding and fitting algorithms. The interplay of these three
 1056 track reconstruction steps is illustrated in Figure 5.2.

1057 5.2 Photons and Electrons

1058 Photons and electrons shower in the LAr calorimeter, and are identified by the energy deposits
 1059 they leave there. Energy deposits in a collection of nearby cells are termed *proto-clusters*, which
 1060 become the starting point for electron and photon reconstruction [48]. The clustering algorithm
 1061 begins when the energy deposit in a certain cell exceeds the noise threshold with a significance
 1062 of 4σ . The algorithm then collects neighboring cells which have an energy deposit exceeding the
 1063 noise threshold with a significance of 2σ , creating a *topo-cluster*². Next, these topo-clusters are

²A topological grouping of neighboring calorimeter cells based on their energy deposits

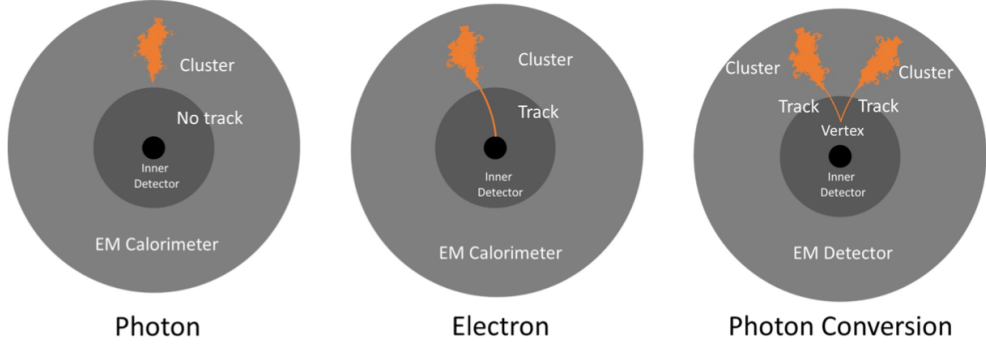


Figure 5.3: Three types of EM object candidates [49].

1064 matched to ID tracks, created as described in Section 5.1. The location of the topo-cluster defines
 1065 a region of interest (ROI) in the ID, where additional modified track reconstruction algorithms are
 1066 run in the case that no associated tracks are found. Any ID tracks associated to the topo-cluster
 1067 are retrofitted to allow for additional energy loss due to bremsstrahlung. A converted photon track
 1068 reconstruction algorithm is run to check for tracks coming from secondary vertices consistent with
 1069 converted photons. The secondary vertices are constructed from two oppositely charged tracks
 1070 consistent with a massless particle, or from one track without any hits in the innermost layer of the
 1071 ID.

1072 For electron identification, the EM cluster is required to match ID tracks that originate from
 1073 the primary vertex at the interaction point. For photon identification, the EM cluster can either be
 1074 matched to tracks coming from a secondary vertex (converted photon), or matched to no tracks
 1075 (unconverted photon). Figure 5.3 illustrates these three cases for EM object identification.

1076 *Superclusters* are built separately for photons and electrons, based on the combined topo-cluster
 1077 and ID track information. First, the EM topo-clusters are tested to see if they meet the minimum
 1078 requirements to become electron or photon seed clusters. For electrons, the cluster must have a
 1079 minimum E_T of 1 GeV, and must be matched to a track with at least 4 hits in the silicon tracking
 1080 detectors. For photons, the cluster must have an E_T greater than 1.5 GeV. If the seed cluster require-
 1081 ments are met, the algorithm searches for satellite clusters, which can arise from bremsstrahlung
 1082 radiation. If the satellite clusters pass the positional, energy and tracking requirements to be asso-

1083 ciated with the proto-cluster, they are combined into a supercluster.

1084 Electron and photon objects are identified from the superclusters after the energy calibration
1085 is applied, which accounts for the energy resolution of each subdetector measurement. Because
1086 photon and electron superclusters are built independently, some clusters can produce both a photon
1087 and an electron. In this case an ambiguity resolution procedure is applied to determine if the
1088 supercluster can be easily identified as only a photon (no tracks present) or only an electron (good
1089 tracks pointing to the primary vertex). In some cases, the identity of the cluster is still ambiguous,
1090 in which case both a photon and electron object are created for analysis and flagged as ambiguous.
1091 Energy, shower shape, and other analysis variables are calculated from the supercluster and saved
1092 with the electron or photon object.

1093 5.3 Muons

1094 Muons are identified through the tracks and energy deposits they leave in the ID, calorimeters,
1095 and Muon Spectrometer (MS). Muons experience minimum ionizing loss, meaning they do not
1096 deposit much of their energy in the calorimeters (recall Figure 5.1), and therefore reach the outer
1097 regions of the detector where the MS is housed. Muon identification begins in the Muon Drift
1098 Tube chambers by performing a straight line fit between the hits found in each layer, creating
1099 *segments*. Segments in the middle layers are then used as seeds for the track building algorithm,
1100 which searches for compatible combinations of segments based on their relative positions and
1101 angles [50]. A χ^2 fit is performed on each track candidate. Based on the χ^2 criteria, hits are
1102 removed or added such that the track contains as many hits as possible while satisfying the fit
1103 criteria.

1104 The MS track candidates are combined with track information from the ID and calorimeters
1105 according to various algorithms based on the information available from each subdetector. Four
1106 different types of muons arise from the various reconstruction algorithms:

- 1107 • Combined muon: a muon track identified through independent track reconstruction in the
1108 ID and MS, where the combined track is formed using a global refit that uses hit information

1109 from both detectors. Most muons are constructed through an outside-in procedure, in which
1110 a muon track candidate is identified in the MS and then an associated track is found in the ID.
1111 A complementary inside-out procedure is also implemented and identifies additional muons.

- 1112 • Segment-tagged muon: an ID track is identified as a muon if when extrapolated out to the
1113 MS (following the inside-out global fit procedure) it is matched to at least one local MS
1114 segment.
- 1115 • Calorimeter-tagged muon: an ID track is identified as a muon if it is matched to a calorimeter
1116 energy deposit that is compatible with a minimum-ionizing particle. This muon identifica-
1117 tion has the lowest purity, but it used in regions where the MS has only partial coverage due
1118 to cabling and service access routes.
- 1119 • Extrapolated muons: the muon is reconstruction only from the MS track and a requirement
1120 on compatibility with the primary interaction point. The muon track is required to cross at
1121 least two layers of the MS, and three layers in the forward region. These muons are mainly
1122 used to extend muon acceptance into the region $2.5 < |\eta| < 2.7$ where ID track information
1123 is not available.

1124 Figure 5.4 illustrates the four types of muon reconstruction. Overlap between reconstructed
1125 muons using ID tracks is resolved by giving preference to combined muons, then segment tagged
1126 muons, and finally calorimeter tagged muons. Overlap with extrapolated muons is resolved by
1127 giving preference to the muon with a better fit quality and higher number of tracks.

1128 All muon track candidates are required to pass a series of quality selections to be identified in
1129 the final muon collection. The primary qualities considered are the χ^2 goodness of fit for the global
1130 track, the difference in p_T measurement between the ID and MS tracks, and the ratio between the
1131 charge and momentum of the tracks. The quality requirements help reject hadrons, primarily from
1132 kaon and pion decays. Muons candidates consistent with cosmic rays are also rejected.

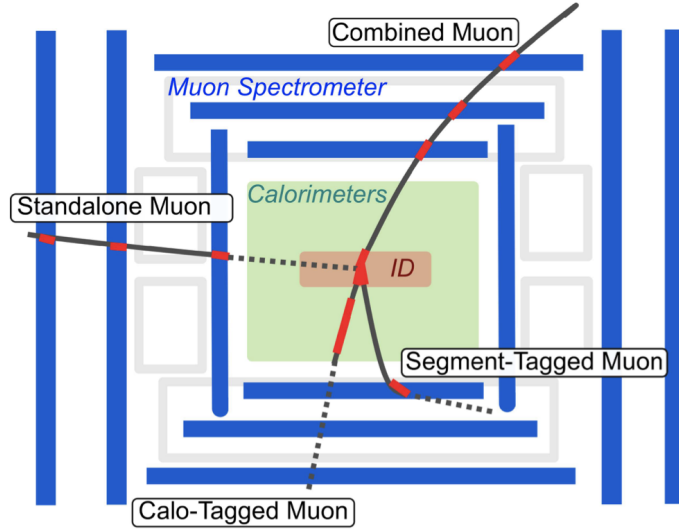


Figure 5.4: The four types of muon track candidates [51]. The red bands indicate where detector measurements for each muon track candidate are made. The dashed lines indicate the path of the muon through detectors where no measurement is made. Standalone muon is another term for an extrapolated muon.

1133 5.4 Jets

1134 The protons accelerated in the LHC are composed of quarks and gluons, and thus their colli-
 1135 sions often result in the release of energetic quarks and gluons, collectively termed *partons*. The
 1136 energetic partons can radiate additional gluons, and these gluons can pair produce quarks in a pro-
 1137 cess called *fragmentation*. Fragmentation continues until the energy drops sufficiently that color
 1138 conservation plays a dominant role. At that point, additional quarks and gluons are produced from
 1139 vacuum to create neutral color states for the fragmented collection of partons. This process is
 1140 known as *hadronization* [52]. The hadronized partons compose a collimated stream of particles,
 1141 known as a *jet*, which is then observed in the detector. The full process that produces jets is known
 1142 as a *parton shower*, and is illustrated in Figure 5.5.

1143 Jets are identified by the energy deposits they leave in the calorimeter, which are then matched
 1144 to the tracks they leave in the ID. Jet reconstruction generally begins in the calorimeters, with
 1145 the identification of *topo-clusters*. Then jet reconstruction algorithms combine calorimeter infor-
 1146 mation with tracking information. There are a variety of jet collections depending on the exact

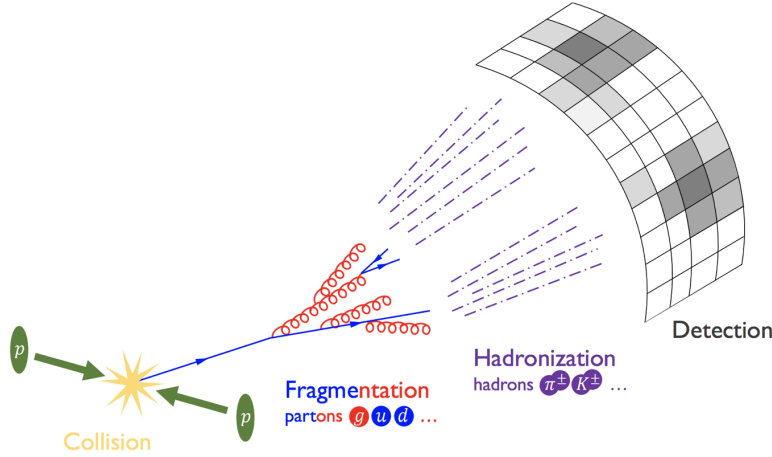


Figure 5.5: The fragmentation and hadronization processes undergone by a quark produced in a proton-proton collision [53].

1147 usage of calorimeter and tracking information in the reconstruction. Some common collections
 1148 include particle flow jets (PFlow), track calo-cluster jets (TCC), EM topo-cluster jets (EMTopo),
 1149 and unified flow object jets (UFO). Only particle flow jets will be discussed in greater detail due to
 1150 their importance in this analysis. The following sections discuss jet identification in the calorime-
 1151 ters, particle flow jet construction using the *anti- k_t algorithm*, jet clustering and jet substructure
 1152 characteristics.

1153 5.4.1 Calorimeter Clusters

1154 Jets are first identified by the energy deposits they leave in the calorimeters. As for photons
 1155 and electrons, the reconstruction of jets in ATLAS begins with the construction of topo-clusters,
 1156 which are topologically-grouped noise-suppressed clusters of calorimeter cells [54]. The topo-
 1157 cluster seed is a cell with an energy that exceeds the noise threshold for the cell with a significance
 1158 of at least 4σ . Any cells adjacent to the seed cell in three dimensions are added to the cluster if
 1159 they have an energy deposit of at least 2σ . This process is repeated, growing the cluster, until no
 1160 adjacent cells exceeding the energy deposit threshold remain. As a final step, all adjacent cells are
 1161 added to the topo-cluster, irrespective of their energy.

1162 The construction process for topo-clusters allows for the possibility that several independent

signatures are grouped into one topo-cluster. To correct for this, the topo-cluster is scanned for local maxima, defined by any cell with energy > 500 MeV, and no neighboring cells with greater energy. If more than one local maximum is identified, the topo-cluster is split among the corresponding energy peaks [55]. In the event that one cell neighbors two or more local maxima, the cell is assigned to the two highest-energy clusters that it neighbors. This means each cell is shared at most once, between at most two post-splitting topo-clusters.

Two measurements for the total energy of the topo-cluster are considered. The raw, or electromagnetic (EM), scale simply considers the sum of energy from all cells in the topo-cluster. The local cell weighting (LCW) scale first classifies clusters as electromagnetic or hadronic, and then applies appropriate corrections for hadronic interactions in the jet energy calculation [54]. The corrections are derived from Monte Carlo simulations, and account for the weaker response of ATLAS calorimeters to hadronic interactions (ATLAS calorimeters are *non-compensating*³), and hadronic energy losses due to interactions with dead material [55].

5.4.2 Particle Flow Algorithm

The calorimeters provide excellent jet energy resolution for high energy jets. However, the granularity of the hadronic calorimeter is restricted to 0.1×0.1 in $\eta \times \phi$. Combining the information from the calorimeter with tracking information provides superior angular resolution and energy resolution. The particle flow (PFlow) algorithm is one of a handful of algorithms which can perform this task.

An overview of the process is given in Figure 5.6. Tracks from the ID which are selected for the PFlow algorithm are required to have at least 9 hits in the silicon detector, and missing pixel hits in places where a hit would be expected. Additionally, the tracks have $p_T > 0.5$ GeV, and $|\eta| < 2.5$. The algorithm then attempts to match these tracks to EM scale calorimeter topo-clusters. This matching is performed using the distance metric

³The response of ATLAS calorimeters is different for EM showers and hadronic showers, since the calorimeter response to hadronic showers is energy dependent

$$\Delta R' = \sqrt{(\frac{\Delta\phi}{\sigma_\phi})^2 + (\frac{\Delta\eta}{\sigma_\eta})^2} \quad (5.1)$$

1187 where σ_η and σ_ϕ represent the angular widths of the topo-clusters, and $\Delta\eta$ and $\Delta\phi$ represent
 1188 the distance between the track (extrapolated to the second layer of the EM calorimeter) and the
 1189 barycenter of the topo-cluster [56]. The topo-cluster closest to the track as measured by $\Delta R'$ is
 1190 considered matched to the track. If no topo-cluster is found within the cone size of $\Delta R' = 1.64$, it
 1191 is assumed that particle which left the track did not form a topo-cluster in the calorimeter.

1192 The PFlow algorithm predicts the expected single topo-cluster energy for a given track, based
 1193 on the track momentum and topo-cluster position. This value is then compared to the observed
 1194 energy of the topo-cluster, and the probability that the particle energy was deposited in more than
 1195 one topo-cluster is evaluated. If necessary, the algorithm adds more topo-clusters to the track/topo-
 1196 cluster system, in order to account of the full shower energy of the track particle.

1197 To reduce the impact of double counting the energy of a given particle by including both its
 1198 tracker and calorimeter energy measurements, the calorimeter energy measurements associated to a
 1199 given track are subtracted from the total calorimeter measurement. If the expected energy deposited
 1200 by the particle exceeds the topo-cluster energy, the full topo-cluster is removed. If the expected
 1201 energy is less than the EM scale energy of all the considered topo-clusters, topo-cluster cells are
 1202 removed one by one, until the full expected energy deposit of the particle has been removed from
 1203 the calorimeter information. The resulting set of tracks and topo-clusters represent the event with
 1204 no double-counting of energy between subdetectors [56]. This information is passed to the jet-
 1205 finding algorithm.

1206 5.4.3 Jet Clustering

1207 When a parton decays in the detector, its energy deposits often result in multiple calorimeter
 1208 clusters. For physics purposes, it is useful to combine clusters that likely resulted from an individ-
 1209 ual parton decay, in order to reconstruct the parton. The process of grouping topo-clusters which
 1210 were produced by the same parton decay is *jet clustering*.

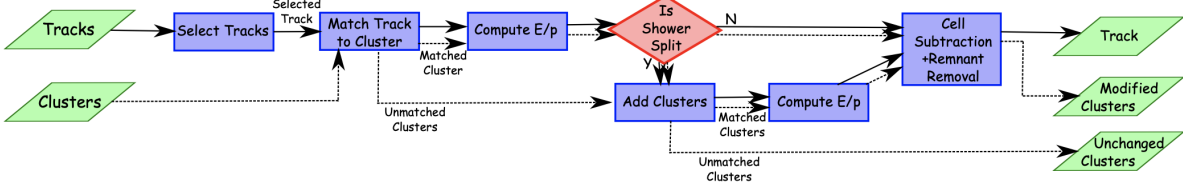


Figure 5.6: A flow chart illustrating the particle flow algorithm progression [56]. The solid lines indicate the progression of tracks through the algorithm, while the dotted lines indicate the progression of clusters. The process begins with track selection and continues until the energy associated with the tracks has been removed from the calorimeter. At the end charged particle tracks, unmodified topo-clusters, and the remnants of topo-clusters which have had part of their energy removed remain.

1211 The anti- k_t algorithm [57] as provided by the FastJet library [58] is most commonly used for
 1212 jet clustering in the ATLAS experiment, with varying reconstruction radius settings. The anti-
 1213 k_t algorithm is based on sequential recombination algorithms [59]. A sequential recombination
 1214 considers the distance d_{ij} between objects i and j (particles or pseudojets), and the distance d_{iB}
 1215 between an object i and the beam line B . If d_{ij} between two objects is the smallest distance among
 1216 those considered, i and j are combined into a pseudojet. The process continues until the smallest
 1217 distance is d_{iB} at which point the object i is determined to be a jet and removed from the objects in
 1218 consideration. The procedure is repeated with the remaining objects until there are none remaining
 1219 [57].

1220 The anti- k_t algorithm adopts this procedure, but modifies the distance measurements d_{ij} and
 1221 d_{iB} to consider the transverse momentum k_t :

$$d_{ij} = \min(k_{ti}^{2p}, k_{tj}^{2p}) \frac{\Delta_{ij}^2}{R^2}, \quad (5.2a)$$

$$d_{iB} = k_{ti}^{2p}. \quad (5.2b)$$

1222 The addition of the term p allows adjustments to algorithm which govern the relative power of
 1223 the momentum versus the geometrical scale $\Delta_{i,j}$, which is defined as $\Delta_{i,j} = (y_i - y_j)^2 + (\phi_i - \phi_j)^2$
 1224 where y_i and ϕ_i are respectively the rapidity and azimuth of particle i [57]. The radius parameter

1225 R is chosen and determines the geometric cone size [59].

1226 In the case $p = 1$ the inclusive k_t algorithm [59] is recovered, which is a standard sequential
 1227 combination jet clustering algorithm. In the case $p = 0$, the Cambridge/Aachen sequential combi-
 1228 nation algorithm [60] is recovered. The case $p = -1$ gives rise to the anti- k_t algorithm. The impact
 1229 of this choice means that the distance d_{ij} between many soft particles is larger than between soft
 1230 and hard particles. Therefore, soft particles tend to cluster with hard ones before they cluster with
 1231 other soft particles. They key feature of this behavior is that soft particles do not modify the shape
 1232 of the jets. This leads to the creation of circular conical jets, a desirable feature which sequen-
 1233 tial combination algorithms and cone algorithms struggle to achieve. Figure 5.7 compares anti- k_t
 1234 jet formation with the inclusive k_t and Cambridge/Aachen algorithms mentioned here, as well as
 1235 the SIScone algorithm [61], which checks for sets of stable cones compatible with the observed
 1236 radiation.

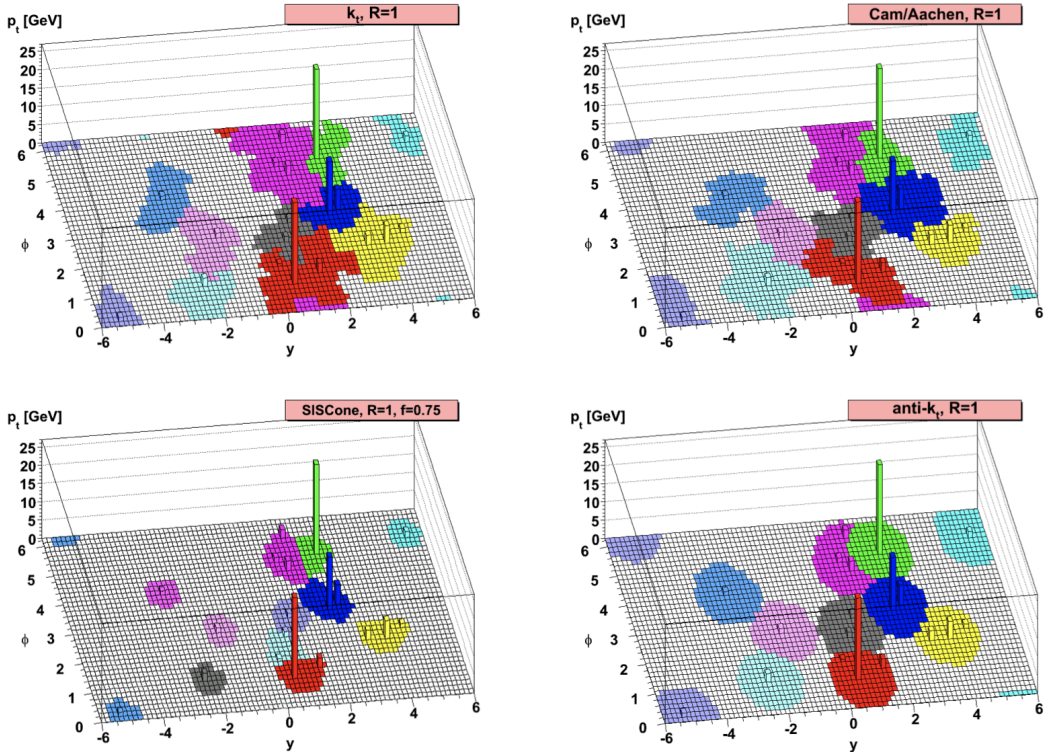


Figure 5.7: A comparison of jet clustering with four different jet algorithms. The anti- k_t algorithm is observed to create the most conical jets, where the shape of the jet is immune to the presence of soft radiation [57].

1237 Any useful jet clustering algorithm must satisfy the requirements of infrared safety and collinear
1238 (IRC) safety. Infrared safety implies that the resulting set of jets is unaltered by the presence of
1239 additional soft particles in the list of seed clusters. As explained above, the anti- k_t algorithm
1240 is naturally infrared safe. Collinear safety requires that the final set of jets is not impacted by
1241 collinear splitting of one of the jets. If the hardest particle p_1 is split into a collinear pair (p_{1a}, p_{1b})
1242 (as is common in the fragmentation process for a hard parton), the jet clustering algorithm must
1243 still recognize (p_{1a}, p_{1b}) as the hardest jet in the collision. If another softer particle p_2 with
1244 $p_{t,1a}, p_{t,1b} < p_{t,2} < p_{t,1}$ is instead considered the hardest particle in the event, a different final
1245 set of jets would be returned. Collinear safety is a requirement of perturbative QCD, to ensure
1246 non-divergent higher-order calculations [62]. The anti- k_t algorithm's tendency to cluster hard par-
1247 ticles first ensures its collinear safety. By satisfying the IRC safety requirement, anti- k_t jets can be
1248 calculated using perturbative QCD, which improves comparisons with theory.

1249 5.4.4 Ghost Track Association

1250 Once a collection of jets has been created, the jet objects can be studied at both the event-level
1251 and the jet-level. In the event-level picture, the momentum, energy, and geometric orientation of
1252 the jets within an event are considered. This yields important information about decay of any
1253 resonant heavy objects, the total energy in the event, and the distribution of energy amongst the
1254 jets. In the jet-level picture, the particle constituents of the jet are considered. The momentum,
1255 energy, and geometric orientation of the associated particle tracks provides a low-level picture of
1256 the jet, which can help determine if the properties of the jet are consistent with standard QCD, or
1257 if new physics processes might be represented within the low-level patterns. Jet-level analysis is
1258 also widely used in flavor tagging.

1259 For anti- k_t jets with a radius parameter $R = 0.4$, one way of studying the jet-level picture is
1260 through considering the ghost-associated tracks. Track association is the process of determining
1261 which tracks should be considered associated with a given jet. In the ghost association algorithm,
1262 the anti- k_t clustering algorithm is used for the collection of tracks and calorimeter clusters [63].

1263 However, the tracks are considered to have infinitesimal momentum (*ghosts*), so their addition to
1264 a jet object does not alter the four-momentum of the jet. This ensures the final jet collection is not
1265 altered by the presence of the ghost tracks in the reclustering, but information about the associated
1266 tracks for each reconstructed jet becomes available [64].

1267 Ghost tracks are of particular importance to this analysis, as a means of providing a low-level
1268 picture of the shape of $R = 0.4$ jets, and discriminating Standard Model QCD-like jets from dark
1269 QCD-like jets.

1270 5.5 Missing Transverse Energy

1271 A simple principle leveraged in ATLAS physics analyses is checking for conservation of mo-
1272 mentum among the products of any $p p$ collisions. The initial state transverse momentum of any
1273 $p p$ collision is always zero, so the transverse momentum of all final state particles should likewise
1274 be zero. The missing transverse energy, E_T^{miss} , is determined by the magnitude of the negative
1275 momentum vector sum of all final state objects resulting from the $p p$ collision.

1276 Specifically, the objects considered in the E_T^{miss} calculation are photons, electrons, muons, jets,
1277 and soft terms. The first four items comprise the hard components of the E_T^{miss} calculation, and
1278 have been discussed previously in this chapter. The final item represents a collection of *soft terms*,
1279 comprising any detector signals not associated to hard detector objects. These can be based on
1280 unassociated tracks, or unassociated soft calorimeter clusters. Both are generally not used in the
1281 same calculation to avoid double counting of soft terms. In this analysis the calorimeter cluster
1282 soft terms are considered in the E_T^{miss} calculation.

1283 E_T^{miss} can arise due to non-interacting Standard Model objects such as a neutrinos, fake sources
1284 such as mis-reconstructed objects and dead detector regions, or in some theories, non-interacting
1285 BSM objects such as a dark matter candidate particles. To understand the amount of E_T^{miss} at-
1286 tributable to detector noise and mis-reconstruction, E_T^{miss} is studied in $Z \rightarrow \mu\mu$ where little real
1287 E_T^{miss} is expected [65]. As Figure 5.8 illustrates, the resolution of E_T^{miss} generally decreases as
1288 E_T^{miss} increases, due to detector resolution effects. As E_T^{miss} is an important quantity for most dark

¹²⁸⁹ QCD analyses, limitations in the accuracy of the E_T^{miss} calculation must be considered.

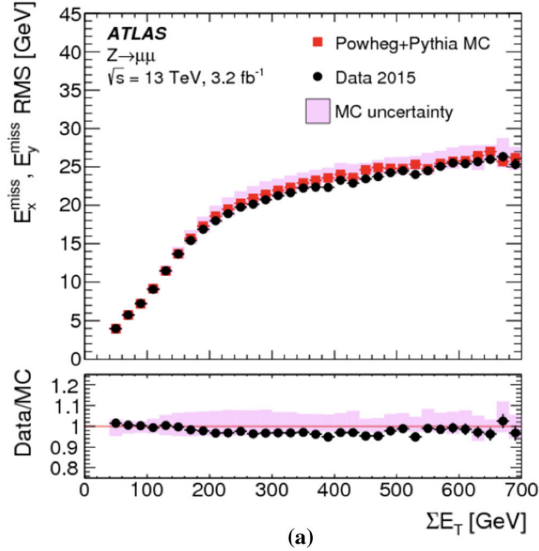


Figure 5.8: A comparison of MC simulation and data for $Z \rightarrow \mu\mu$ events where real $E_T^{\text{miss}} = 0$ [65]. The resolution of the missing energy in the transverse ($x - y$) plane is observed to increase with increasing total $\sum E_T$.

1290

Part III

1291

Search

1292

1293

Chapter 6: Monte Carlo and Data

1294 The search for semi-visible jets via s-channel production presented in the following chapters
1295 is performed with an integrated luminosity of 139 fb^{-1} of proton-proton collision data collected
1296 by the ATLAS detector during Run 2 (2015 - 2018). The full Run 2 dataset is used for the final
1297 interpretation. Monte Carlo (MC) simulations of background processes and the semi-visible jet
1298 signal process are used in the development of the analysis strategy, and in the final interpretation
1299 to set limits on the observed cross-section of the signal model. This chapter will provide details
1300 about the full Run 2 dataset, and the background MC simulations, and the signal MC simulations
1301 used in this search.

1302 **6.1 Data**

1303 The 139 fb^{-1} integrated luminosity of proton-proton collision data used for physics analyses
1304 are required to pass a set of data quality checks. In Run 2 94% of the pp collisions delivered by
1305 the LHC were successfully recorded by the ATLAS experiment, as illustrated in Figure 6.1. 95%
1306 of the data recorded by the ATLAS experiment was marked as “good for physics”, resulting in 139
1307 fb^{-1} of integrated luminosity. Events are rejected if they are corrupted or incomplete, or if they
1308 were recorded during a subsystem malfunction.

1309 Events for this analysis are further required to pass a single-jet trigger selection, where events
1310 are required to have a jet at trigger-level with a p_T that exceeds a certain value. The lowest p_T un-
1311 prescaled¹ single jet trigger threshold for each period is as follows:

- 1312 • 2015: $p_T \geq 360 \text{ GeV}$

¹An unprescaled trigger records every event that meets the trigger requirement. A prescaled trigger only records a fraction of events that meet the trigger requirement.

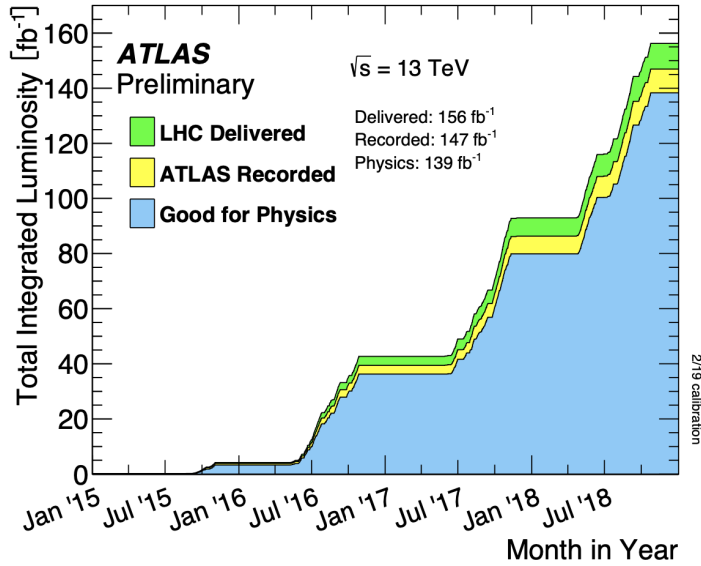


Figure 6.1: Integrated luminosity for the ATLAS experiment as a function of time during Run 2 [66]

- 2016 & 2017: $p_T \geq 380 \text{ GeV}$

- 2018: $p_T \geq 420 \text{ GeV}$

A post-trigger selection of jet $p_T > 450 \text{ GeV}$ ensures all these triggers are fully within their

efficiency plateaus. The jet collection used is anti- k_t EM particle flow jets with a radius parameter of $R = 0.4$, also referred to as small- R jets.

Due to the variance in visible and invisible momenta due to the R_{inv} parameter of the signal

model, many signals also have significant E_T^{miss} . The use of a E_T^{miss} trigger to select events was considered, and the single jet approach described here was found to preserve more signal events across the grid, particularly in the high resonance mass and low R_{inv} region of phase space. These studies are documented in Appendix A.

The data are subject to a blinding strategy throughout the analysis design so as to mitigate

analyzer-induced bias. Blinded and unblinded region definitions are described further in Section 8.1.

1326 **6.2 Simulation**

1327 Simulated events are generated with a variety of Monte Carlo (MC) generator processes that
1328 run in stages. The $p p$ hard scatter physics process is simulated, and the final state particles are
1329 subsequently showered and decayed. This full description of the event is then propagated through
1330 a detailed detector simulation based on GEANT4 [67]. The MC simulation is weighted to match
1331 the distribution of the average number of interactions per bunch crossing μ observed in collision
1332 data.

1333 All simulated samples included in this analysis were produced with three different MC cam-
1334 paigns: `mc20a` corresponds to 2015-2016 data-taking conditions, `mc20d` to 2017, and `mc20e` to
1335 2018. These three campaigns are weighted to the integrated luminosities of their respective data-
1336 taking periods and combined to produce simulation for the entire Run 2 dataset. Simulated events
1337 are reconstructed with the same algorithms run on collision data.

1338 **6.2.1 Simulated Backgrounds**

1339 Although the final background estimation is data-driven, background MC is studied for analysis
1340 optimization and machine learning tool development.

1341 Dijet QCD is the dominant background process. QCD is simulated with PYTHIA8 [68], and
1342 generated in approximate slices of p_T , to ensure high statistics across the momentum spectrum.
1343 The slices are then reweighted using MC generated event weights to create a physical distribution.
1344 Figure 6.2 illustrates the 8 momentum slices used in this analysis.

1345 Due to presence of E_T^{miss} in the SVJ signals, additional MC background processes are required
1346 to create a full picture of the relevant background. The $Z \rightarrow \nu\nu$ process contributes to the back-
1347 ground due to its high missing energy. Leptonic W/Z decays and W/Z+jets are also included as
1348 they can contribute both additional missing energy and significant hadronic activity. Single top
1349 and $t\bar{t}$ processes are also considered for their contribution to hadronic activity. After the analysis

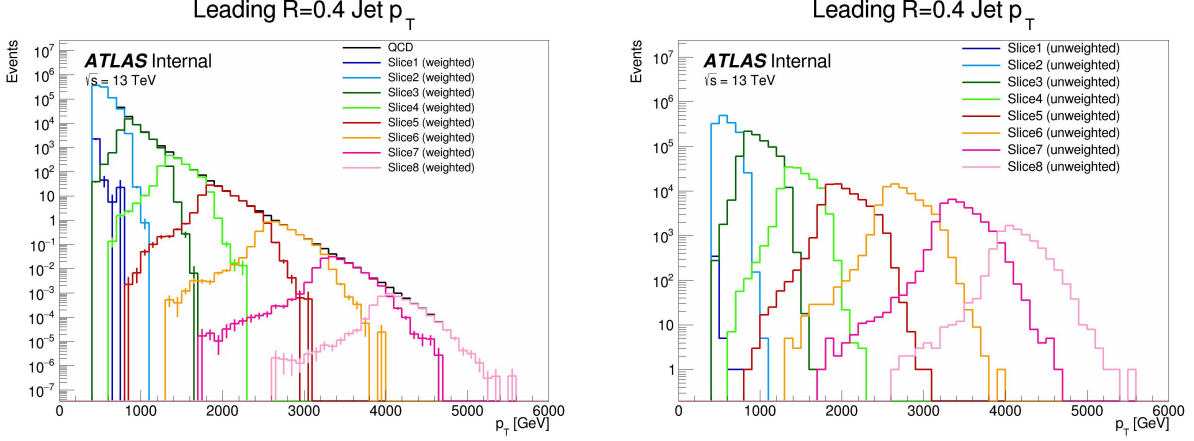


Figure 6.2: The transverse momentum slices of the QCD MC simulation, overlayed to show how they come together to create a smooth distribution (left) once weighted properly. The original unweighted distribution is shown on the right, illustrating the enhanced statistics for the high p_T range.

1350 *preselection*² is applied to isolate events most relevant to the SVJ topology, the background compo-
 1351 sition is 76% QCD, 12% $W+jets$, 8% top and $t\bar{t}$ processes, and 4% $Z \rightarrow \nu\nu$. Figure 6.3 illustrates
 1352 the background composition for the analysis. The lower panel in Figure 6.3 illustrates the ratio
 1353 between data (black) and the combined MC processes (grey). While the agreement between data
 1354 and MC is not perfect (ratio = 1.0 for all E_T^{miss} values), the difference is < 20% throughout the
 1355 distribution. This is within tolerance for this analysis, since the final background estimation will
 1356 be data driven, and background MC is only needed for approximate modeling. Analysis selections
 1357 for high energy jets (discussed in Section 8.1) create some sculpting in the $Z \rightarrow \nu\nu$ and $W+jets$
 1358 distributions; however, the total E_T^{miss} distribution is smoothly falling so this is not an issue.

1359 6.2.2 Signal Simulation

1360 The Hidden Valley (HV) signal model implementation is based on Ref [22]. The s-channel
 1361 semi-visible jet model, which was described in Chapter 2, is governed by a number of parameters.
 1362 The mass of the mediator $m_{Z'}$ can be set, together with the couplings of the Z' to the visible and
 1363 dark quarks g_q and g_{q_D} . The dark sector shower is governed by the number of dark colors N_{c_D} ,

²A preselection is a set of cuts on physical observables used to isolate a collection of events which are most likely to contain the desired signal. The preselection for this analysis will be discussed in Section 8.1

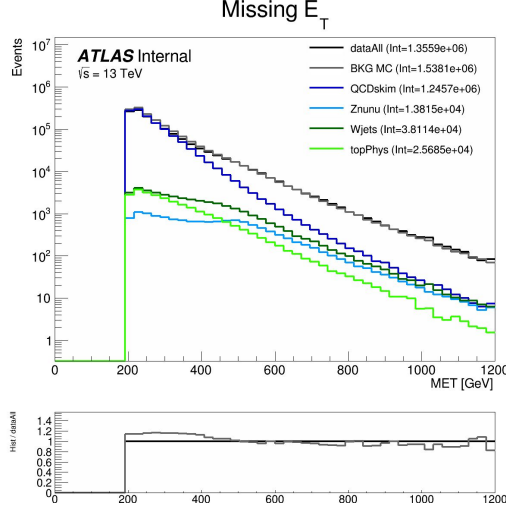


Figure 6.3: Background processes relevant to the SVJ signal.

Parameter	Value
N_{c_D}	3.0
g_{qD}	1.0
Λ_D	10.0
N_{f_D}	2.0

Table 6.1: Fixed parameters in the Pythia8 HV model

1364 the number of dark flavors N_{f_D} , and the dark sector confinement scale Λ_D . There is also the
 1365 characteristic scale of the dark hadrons m_{dark} , determined by the mass of the dark quarks m_{q_D} .
 1366 The characteristic scale determines the mass of the dark hadrons, which can be pseudoscalars m_{π_D}
 1367 or vectors m_{ρ_D} . Finally, the average fraction of invisible particles in the final state jet is dictated
 1368 by R_{inv} .

1369 The chosen parameters for this model were carefully selected in collaboration with theorists
 1370 to be compatible with the new benchmarks established in the 2021 Snowmass process [21]. The
 1371 signal generation allows for up to two initial state radiation jets, and uses a jet-matching scheme
 1372 described in Ref. [69] and implemented in Ref. [68] to match jets to the original partons.

1373 The choices of fixed parameters for the Pythia8 HV model are summarized in Table 6.1. A
 1374 detailed discussion of these parameters and their implications on the dark shower topology can be
 1375 found in Ref. [21]. The mass choices for the dark quark and the dark hadrons are also summarized
 1376 in Table 6.2.

Parameter	Value [GeV]
m_{π_D}	17.0
m_{ρ_D}	31.77
m_{q_D}	10.0

Table 6.2: Values for m_{dark}

$m_{Z'}$ (GeV)	Cross section (fb)
2000	252
2500	74.2
3000	24.5
3500	8.83
4000	3.49
5000	0.757

Table 6.3: Mass points and cross sections of the SVJ search signal grid

1377 Note that the number of dark flavors differs from the Snowmass recommendation of $N_{f_D} =$
 1378 4. This change is minimal in impact because R_{inv} is set explicitly (rather than allowing it to
 1379 arise naturally from the HV theory), and allows this ATLAS analysis result to remain comparable
 1380 with the CMS semi-visible jets s-channel analysis [70] and the ATLAS semi-visible jets t-channel
 1381 analysis [71].

1382 The mediator mass $m_{Z'}$ and the fraction of invisible particles in the final state R_{inv} vary, and
 1383 are used to define the search grid. $m_{Z'}$ varies between 2.0 TeV and 5.0 TeV, while R_{inv} varies from
 1384 0.2 to 0.8. R_{inv} values of 0.2, 0.4, 0.6, and 0.8 are generated for each $m_{Z'}$ mass point. Table 6.3
 1385 illustrates the signal grid and the associated cross-section for each signal.

1386 Samples are generated using MADGRAPH5 [72] version 2.9.9 interfaced to PYTHIA8.244P3 [68]
 1387 for shower and hadronization with NNPDF23LO PDF [73] and the ATLAS A14 [74] to tune the
 1388 underlying event data.

1389

1390

Chapter 7: Machine Learning Tools

1391 **7.1 Introduction**

1392 The search for semi-visible jets presents an opportunity to use novel machine learning (ML)
1393 tools to uncover patterns in the behavior of dark QCD. The subtlety of the shower differences
1394 between dark QCD (signal) and SM QCD (background) motivates a complex model that can accept
1395 high-dimensional low-level information, such as travel level information, to best understand key
1396 differences between signal and background correlations. Additionally, the large number of theory
1397 parameters which can be chosen arbitrarily and affect the shape of the dark QCD shower motivate
1398 exploring a data-driven machine learning approach, which could be sensitive to a wider variety of
1399 dark QCD behavior.

1400 To this end, two machine learning approaches are developed for this search, which are used
1401 in tandem. The first is a supervised ML method where the ML algorithm is built to maximize
1402 exclusion sensitivity to the specific generated SVJ signal models used in this analysis. Here, su-
1403 pervised refers to the use of full and correct *labels*¹ for all events considered during model training,
1404 which necessitates training over simulated data. The second is a semi-supervised method, where
1405 training of the model is data-driven and labels are only partially provided during training. The
1406 semi-supervised ML algorithm broadens the discovery sensitivity of the search, and reduces the
1407 dependence on the exact theory parameters chosen for signal model simulation.

1408 The two different ML algorithms used in this approach will be explained in the following
1409 sections, along with their application in the SVJ analysis strategy.

¹In machine learning a label refers to the correct identification information for an input. In the case of the binary classifier algorithm discussed here, the label is either “signal” or “background”.

1410 7.1.1 Particle Flow Network (Supervised)

1411 **Architecture Fundamentals**

1412 A Particle Flow Network (PFN) [75] architecture is selected for two reasons: *permutation in-*
1413 *variant input modeling* to best describe the events consisting of an unordered set of particles, and a
1414 *low-level input modeling* using tracks to take advantage of the available high-dimensional informa-
1415 tion to best exploit available correlations within the event. Permutation invariant input modeling
1416 is an architecture priority as ordered input modeling has been observed to bias the performance of
1417 low-level modeling tools as in [76]. Low-level input modeling is an architecture priority to capture
1418 the intricacies of dark QCD showers which may not express themselves in higher level variables,
1419 as explored in [22]. A comparison to a high-level *boosted decision tree* (BDT) is available in
1420 Appendix B.3.

1421 The PFN is used to model input events as an unordered set of tracks. Given the inherently
1422 unordered and variable-length nature of particles in an event, this choice of modeling as a *set*
1423 can enable the model to better learn the salient features of the dataset that enable a signal-to-
1424 background classification. Constructing the PFN involves the creation of new basis variables Φ
1425 for each particle in the event. Permutation invariance is enforced by summing over the Φ basis for
1426 every particle in the event to create a new permutation invariant latent space basis O . Finally the
1427 classifier F is a function of the sum over this new basis. The creation of the latent space basis O
1428 from M particles \vec{p} with d features each can be expressed as:

$$O(\{\vec{p}_1, \dots, \vec{p}_M\}) = \sum_{i=1}^M \Phi_i(\vec{p}_i) \quad (7.1)$$

1429 where $\Phi : \mathbb{R}^d \rightarrow \mathbb{R}^l$ is a per particle mapping, with l being the dimension of the new basis O .
1430 Figure 7.1 gives a graphical representation of the use of summation in the PFN over per-particle
1431 information to create a permutation-invariant event representation.

1432 Figure 7.2 provides an annotated diagram of the PFN architecture as used in this analysis.

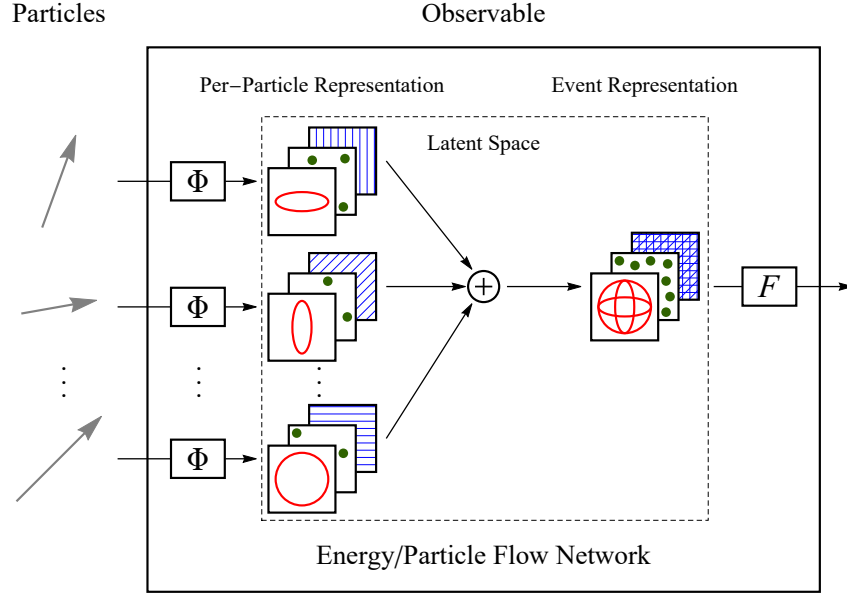


Figure 7.1: The Energy/Particle Flow Network concept, from Ref. [75].

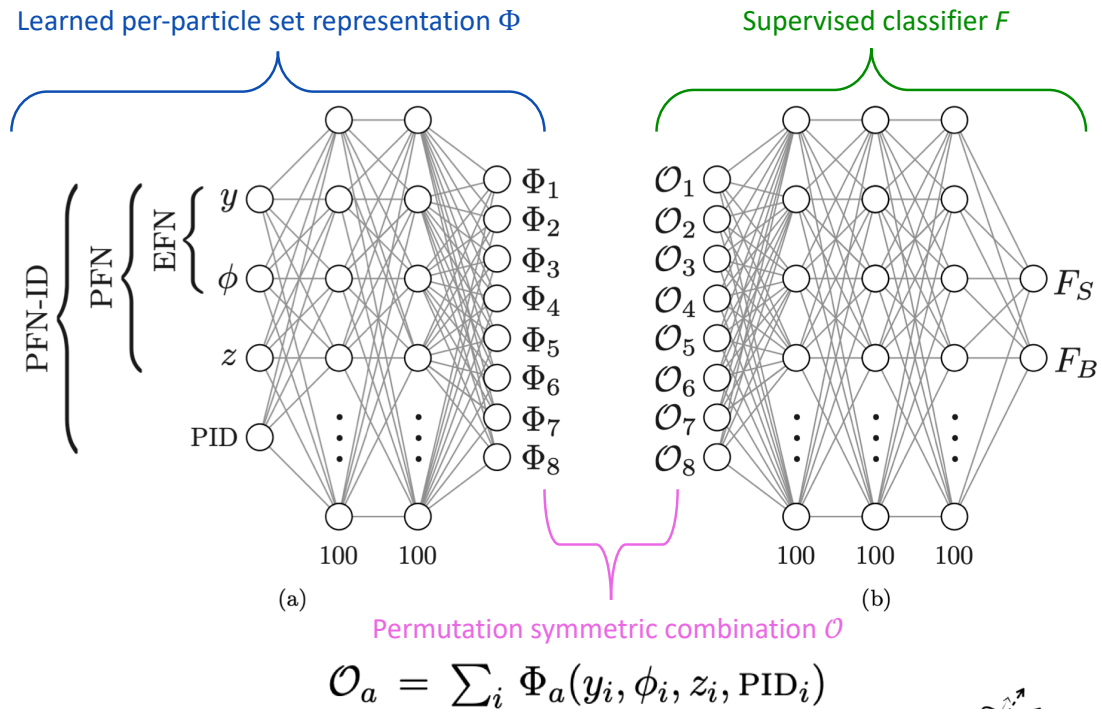


Figure 7.2: An annotated diagram of the PFN architecture. y and ϕ represent geometric information for the input particles, z represents energy information, and PID encompasses any other particle ID information in the input.

1433 **Input Modeling, Scaling, and Rotation**

1434 In this implementation, the particle input information comes from all tracks associated to the
1435 leading and subleading jets. The track association method is Ghost association, as discussed in
1436 Section 5.4.4. A single jet tagger strategy was also considered, but utilizing tracks from both
1437 leading jets creates a complete low-level picture of the event, which both focuses on the objects
1438 most likely to be associated to the decay of the dark quark (as will be justified in Chapter 8)
1439 and the relationship between those objects. If we consider the dijet topology of semi-visible jets
1440 as illustrated in Figure 7.3, the advantage of modeling both leading jets simultaneously becomes
1441 clear. In the semi-visible jet model presented in [22], E_T^{miss} in the event is expected to arise due to
1442 an imbalance in the number of visible tracks of the two jets associated to the dark quark decay.

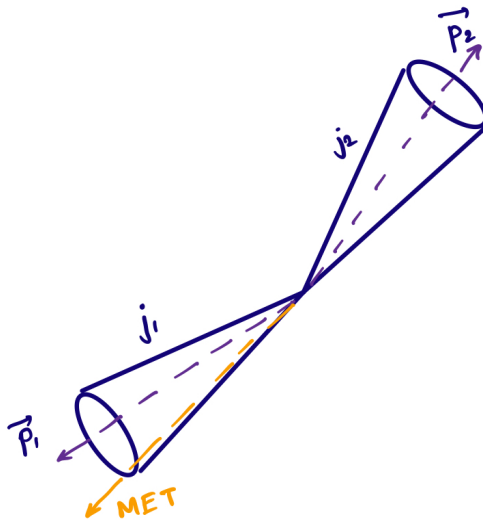


Figure 7.3: A illustration of the expected dijet behavior of semi-visible jets, where one jet is closely aligned with E_T^{miss} .

1443 Each track is described using six variables: the four-vector of the track (p_T , η , ϕ , E), and the
1444 track displacement parameters d_0 and z_0 , where d_0 measures displacement in the radial direction
1445 from the beamline and z_0 measures displacement along the beamline from the primary interac-
1446 tion point. Figure 7.4 illustrates these coordinates. Up to 80 tracks per jet are allowed, which is
1447 a threshold chosen to generally include all the tracks in the jet, which leads to maximal perfor-

1448 mance. Figure 7.5 shows the track multiplicity in the leading and subleading jet for the signal and
 1449 background samples used in training.

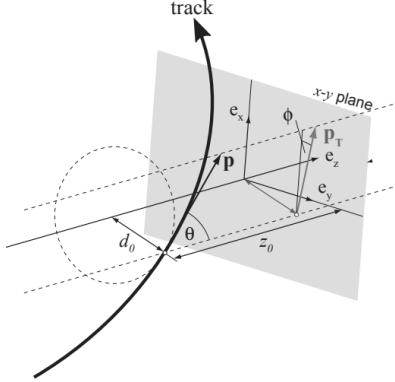


Figure 7.4: Illustration of track coordinates d_0 and z_0 .

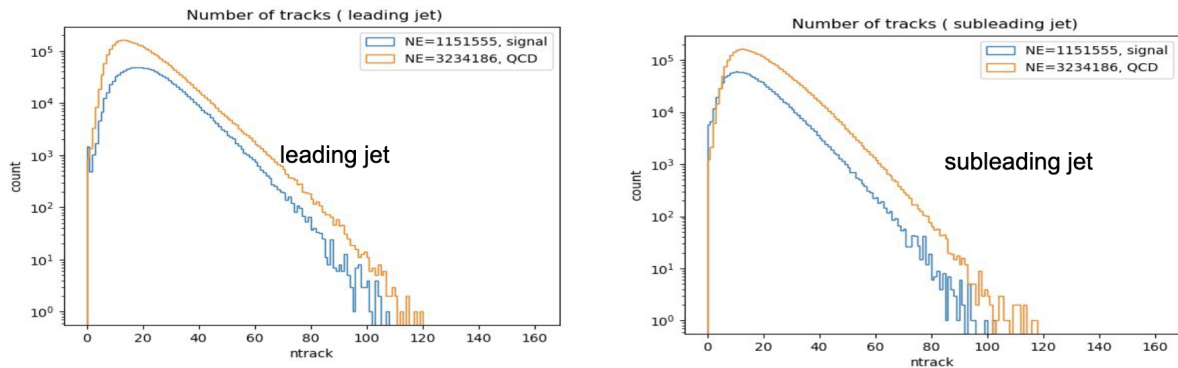


Figure 7.5: Distributions of the track multiplicity in the leading and subleading jets, comparing signal and background PFN training samples.

1450 These tracks (up to 160 total) are the input to the PFN. Referencing Equation 7.1, this corre-
 1451 sponds to $M = 160$ and $d = 6$. The two leading jets and their associated tracks are rotated so
 1452 that the center of the system is aligned with $(\eta, \phi) = (0, 0)$. Each track is normalized to its relative
 1453 fraction of the total dijet system energy and transverse momentum- this enforces agnosticism to the
 1454 total energy and transverse momentum of the event. The rotation and scaling are motivated by the
 1455 procedures described in [75] to improve the optimality of the PFN learning. Figure 7.6 illustrates
 1456 the rotation process.

1457 Finally, each of the 6 track variables is scaled so that its range is $[0,1]$. This is a common

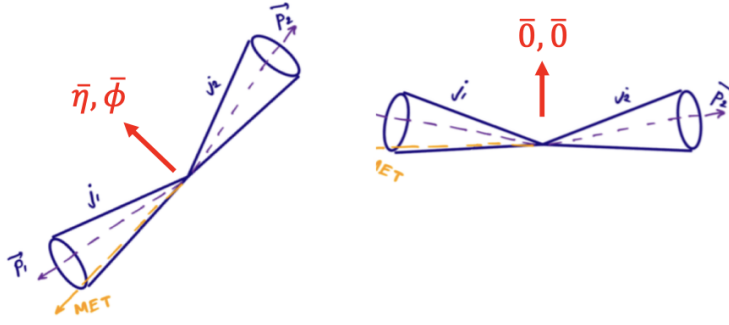


Figure 7.6: A diagram demonstrating how the two jet system is rotated in (ϕ, η) .

1458 preprocessing step that ensures the input data is bounded over a similar range, so that arbitrarily
 1459 large values don't develop an outsized impact on the model. Figure 7.7 show each of 6 track
 1460 variables before and after scaling and rotation have been applied, demonstrating the impact of
 1461 these procedures, as well as the track level similarities differences between the background SM
 1462 QCD processes and the signal SVJ processes. Figure 7.8 illustrates that the data is well modeled
 1463 by the MC at track level.

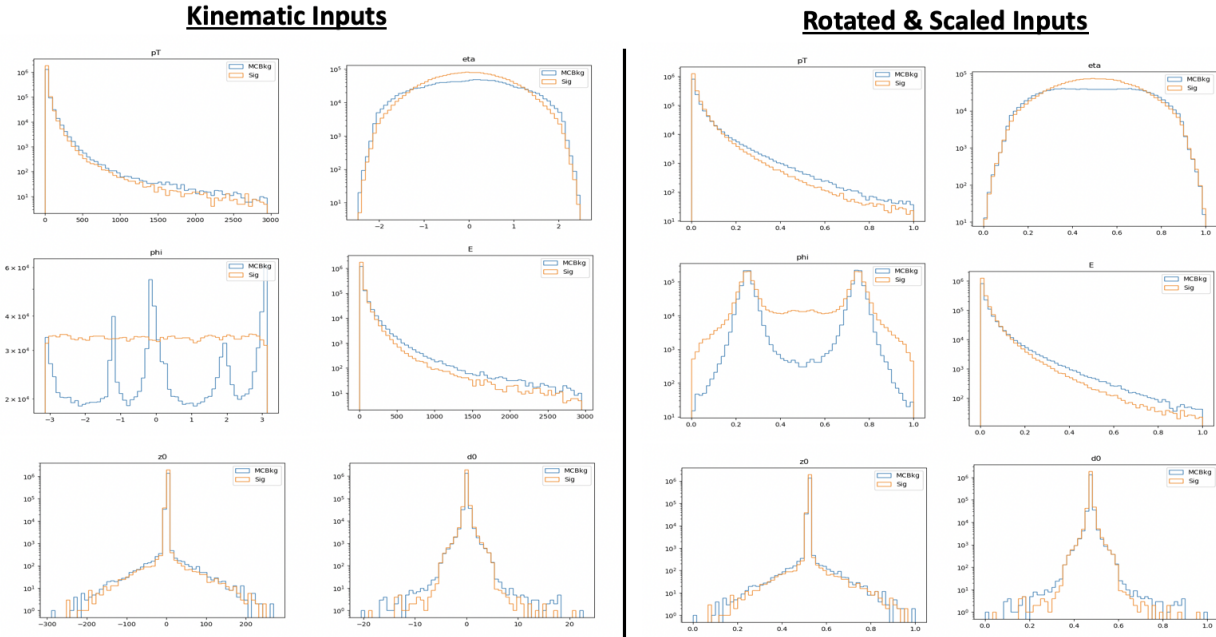


Figure 7.7: The 6 PFN track variables in background MC and signal MC. There are some differences between signal and background, but the track kinematics are largely similar.

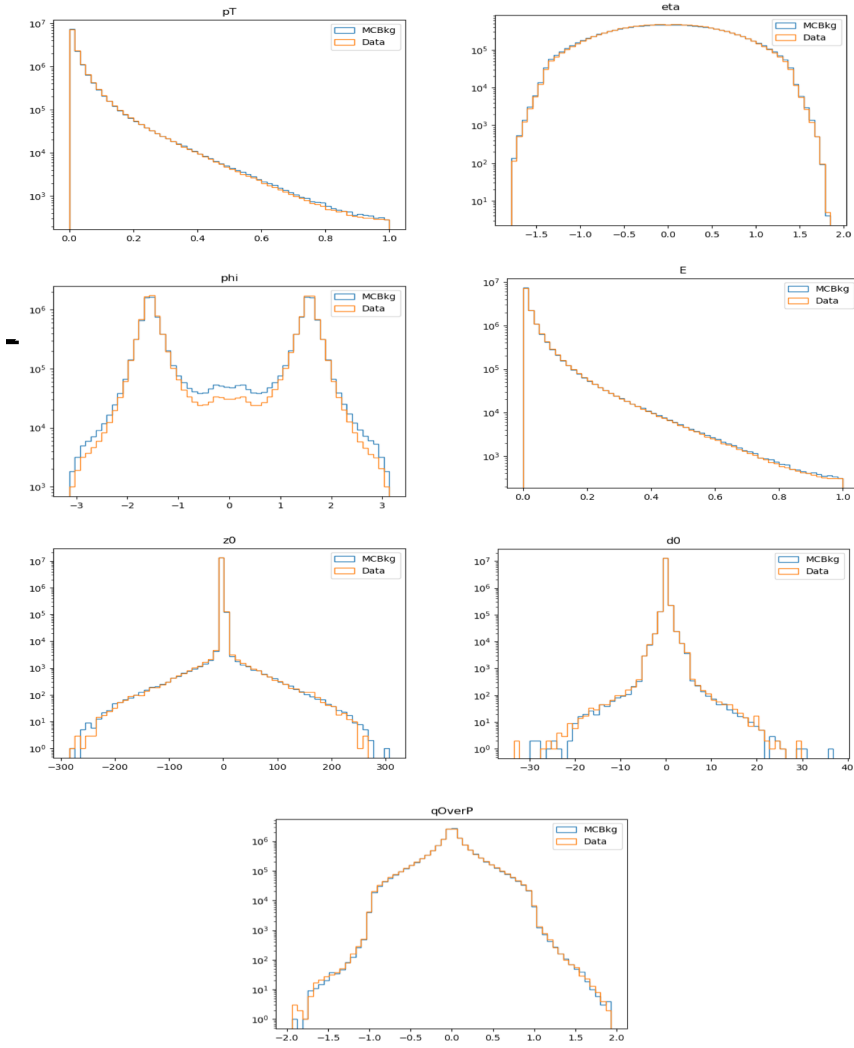


Figure 7.8: The 6 PFN track variables in data and background MC, after the scaling and rotation procedure is applied. There is excellent modeling of the data by the MC within the track variables. The slight discrepancy in the ϕ distribution is due to the modeling of dead TileCal cells by the QCD MC, which will be discussed in Chapter 8. The level of discrepancy is determined to be within tolerance given that the final result will be data driven and the QCD model is used in the PFN training only.

1464 **Training**

1465 As seen in Figure 7.2, two separate architectures are defined and combined to do the super-
1466 vised training. The PFN uses a masking layer to suppress any zero-padded inputs, making the
1467 architecture length agnostic. The masking layer ignores any all-zero inputs in the summation layer.
1468 Additionally, The summation layer in the PFN enforces permutation invariance, so the network is
1469 unordered. The Φ network has 3 dense layers of dimensionality 75 with RELU activation, with
1470 27.5k trainable parameters and an output Φ latent space dimension of 64.

1471 The classifier F network similarly has 3 dense layers with 75 nodes with RELU activation, and
1472 a final softmax layer to determine the event-level classification with a categorical cross-entropy
1473 loss. The Adam optimizer is used with an initial learning rate of 0.001.

1474 The PFN is trained in a fully supervised way using SVJ signal MC and QCD MC events. Al-
1475 though several SM processes are expected to contaminate the SR (see Chapter 8), QCD is the dom-
1476 inant background. Training against a QCD-only sample is determined to produced better results
1477 than training on a more complete background - when training with a background which repre-
1478 sents samples that are more enriched in E_T^{miss} , the ability of the PFN to identify high E_T^{miss} signals
1479 is reduced. When training with a QCD-only background, there is greater contamination from
1480 E_T^{miss} enhanced backgrounds in the final SR - however the increased signal acceptance means that
1481 overall sensitivity is still higher with a QCD-only training. This can be seen in the comparison of
1482 output classifier distributions in Figure 7.9.

1483 500k events from both background and signal are used in training, where the signal is a com-
1484 bined file of all simulated signal points and the full QCD background which is sampled according
1485 to it's MC weights to produce the proper p_T input shape. A study was done to check the optimality
1486 of the inclusive signal model PFN as compared to one trained on high and low R_{inv} points sepa-
1487 rately, to better capture the differences in high and low E_T^{miss} across signals and backgrounds, but
1488 a small effect is found and the decision is taken to keep the inclusive model (Appendix B.2).

1489 The network is trained for 100 epochs. A train/test/validation split of 78%, 20%, and 2% is used
1490 for the final PFN training. Figure 7.10 shows the loss during training, which is stable and flattens

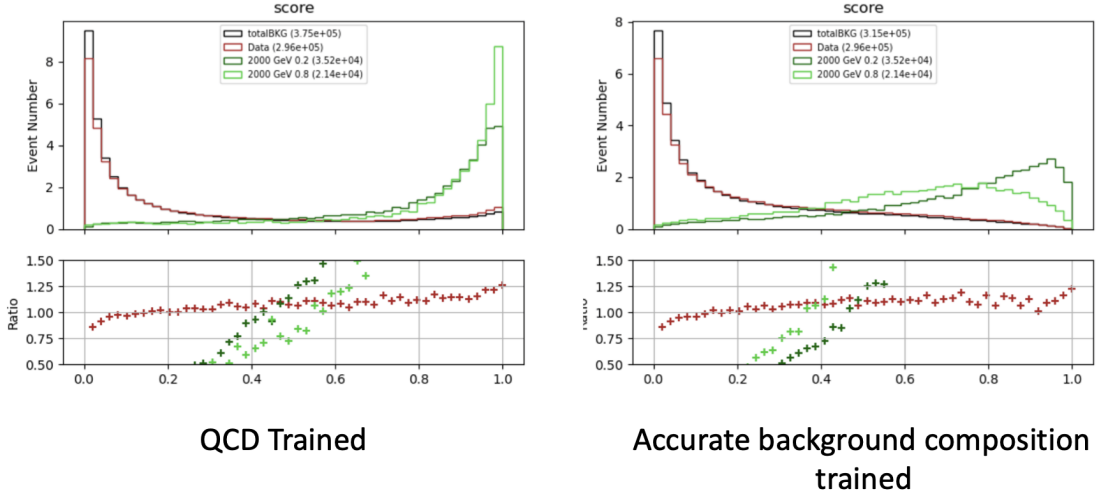


Figure 7.9: PFN score for background MC, data, and signal, comparing a PFN training on QCD-only vs all-background MC samples. The average AUC for the QCD-only training (left) is 0.93, while the average AUC for the mixed background training (right) is 0.84. The sensitivity estimate across the grid is better for the QCD-only training - from the distribution we can conclude that this is because the sensitivity to MET enhanced signals is greatly reduced.

1491 by the end of training, and the final evaluated losses that provide signal-background discrimination
 1492 over the test set.

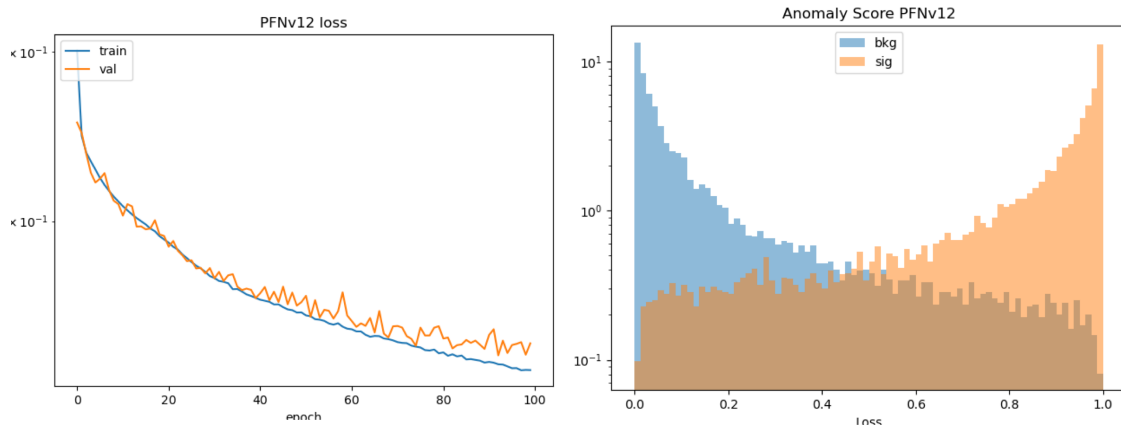


Figure 7.10: PFN architecture loss during training as a function of epoch (left) and the evaluated loss over the signal and background (right).

1493 Optimization studies were performed on the PFN, varying the number of training epochs, num-
 1494 ber of training events, batch size, learning rate, number of neurons, and dimension of the Φ space.
 1495 A summary of these studies is presented in Appendix B.2. The model presented here represents an
 1496 optimal choice across these parameters.

1497 **Performance**

1498 The performance of the PFN can be assessed via the area-under-curve (AUC) of the receiver
1499 operating characteristic (ROC) associated to evaluating the PFN on the test set of signal and back-
1500 ground events. Figure 7.11 shows the ROC curve of the PFN when classifying the QCD back-
1501 ground from the combined signal, with an AUC of 0.93. Figure 7.12 shows the AUC of the PFN
1502 across the SVJ signal grid, demonstrating strong discrimination capability even in the varying cor-
1503 ners of phase space. Figure 7.13 shows the output score distribution in two signals, data, and the
1504 total background MC. A selection of PFN score > 0.6 for all SR events is chosen to maximize
signal sensitivity across the grid.

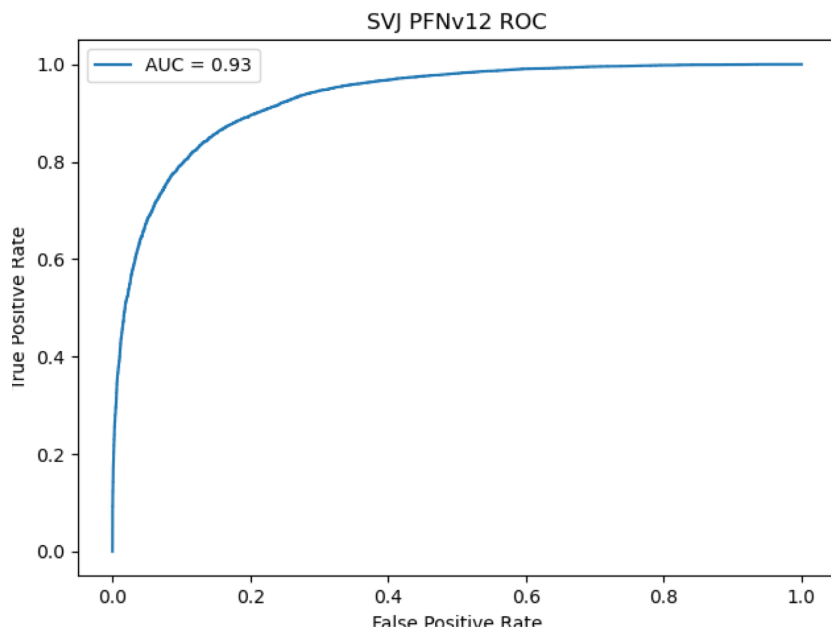


Figure 7.11: ROC the PFN score for combined signal (true positive) and QCD background (false positive).

1505

1506 Another supervised approach was studied using a BDT as the primary selection tool, trained
1507 over high-level variables describing each event. Studies comparing the PFN and BDT approaches
1508 are provided in Appendix B.3. Ultimately the low-level high-dimensional approach offered by the
1509 PFN was selected for its increased performance and lessened kinematic dependence.

1510 Appendix B shows more studies on the ML methods and comparisons of varying approaches.

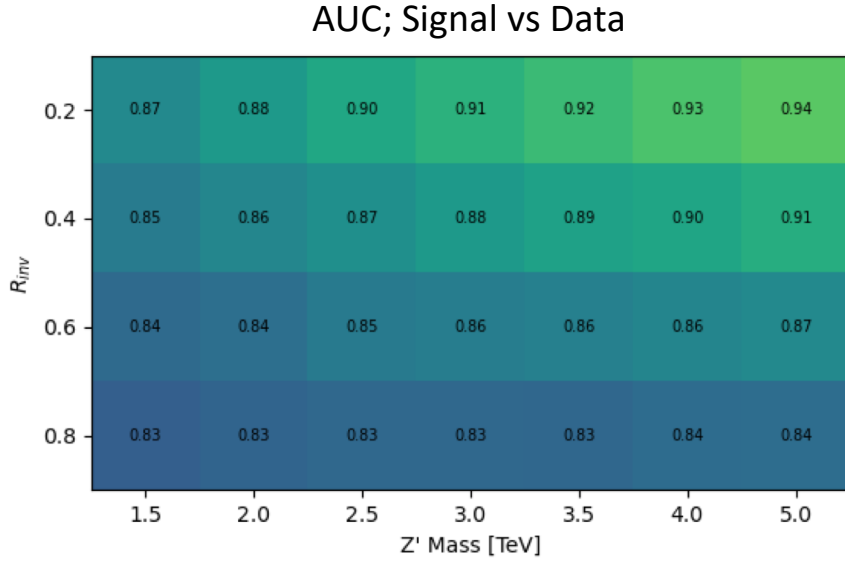


Figure 7.12: AUC from the PFN score for each signal in the SVJ grid, shown versus the QCD-only training sample.

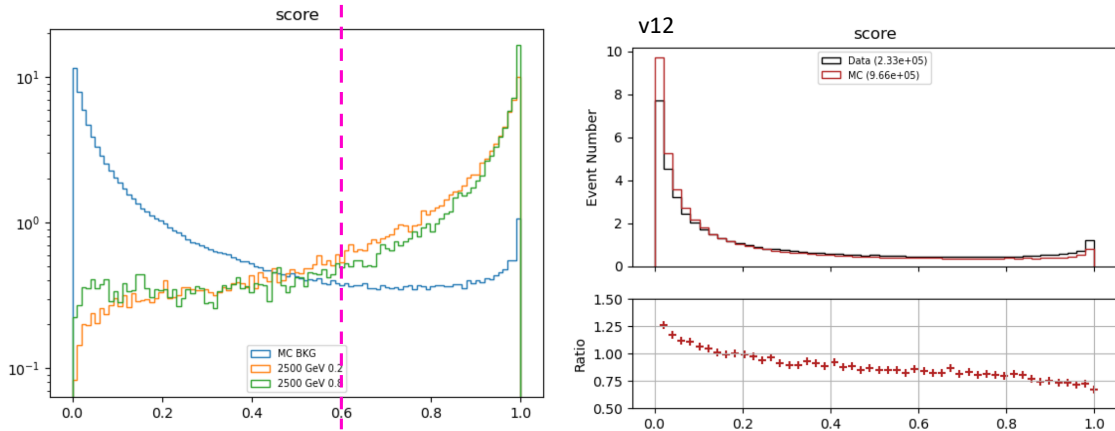


Figure 7.13: PFN score for two signals and the total background MC (top), and between data and MC (bottom). The difference between data and MC efficiency is minimal (< 5%).

1511 7.1.2 ANTELOPE (Semi-supervised)

1512 The semi-supervised analysis approach broadens the discovery sensitivity of the search through
1513 the use of semi-supervised ML, where training of the model is data-driven and labels are only
1514 partially provided during training. While broad sensitivity is a general key goal of LHC searches,
1515 it is particularly motivated in the case of dark QCD models, which can lead to widely varying
1516 topologies depending on the values of model parameters. In the case of SVJs, the R_{inv} fraction in
1517 the jet can dramatically vary the E_T^{miss} , shower shape, and other key features, making it difficult to
1518 find a single standard analysis variable that can distinguish all signal topologies from QCD.

1519 **Architecture Fundamentals**

1520 The model-independent search region of this analysis is implemented with a novel ML ap-
1521 proach that builds on the ANTELOPE architecture to construct a tool that is capable of performing
1522 low-level anomaly detection with permutation-invariant inputs. This tool, referred to as **ANomaly**
1523 **deTEction on particLe flOw latent sPacE (ANTELOPE)**, is a custom solution designed for this
1524 analysis.

1525 ANTELOPE uses the supervised signal vs. background training of the PFN network described
1526 in the previous section to generate a permutation invariant latent space that is representative of the
1527 original input variables, encodes the input events into these latent space variables O , and trains a
1528 *variational autoencoder* (VAE) over the events modeled as PFN latent space variables. A VAE
1529 is a common architecture used for anomaly detection and data-driven ML training. It has been
1530 used in previous ATLAS searched to model jet level information, such as the search presented
1531 in [77] using the recurrent architecture described in [76]. One of the limitations of a recurrent
1532 architecture is the need to order the low level inputs, which affects the performance of the tool. Jet
1533 constituent information is intrinsically unordered, and therefore a permutation invariant approach
1534 removes this element of arbitrary decision making from the modeling process. A visual example
1535 of the ANTELOPE inputs is given in Figure 7.14.

1536 The input to the model is the same 6 track variables for the leading 160 tracks of the leading

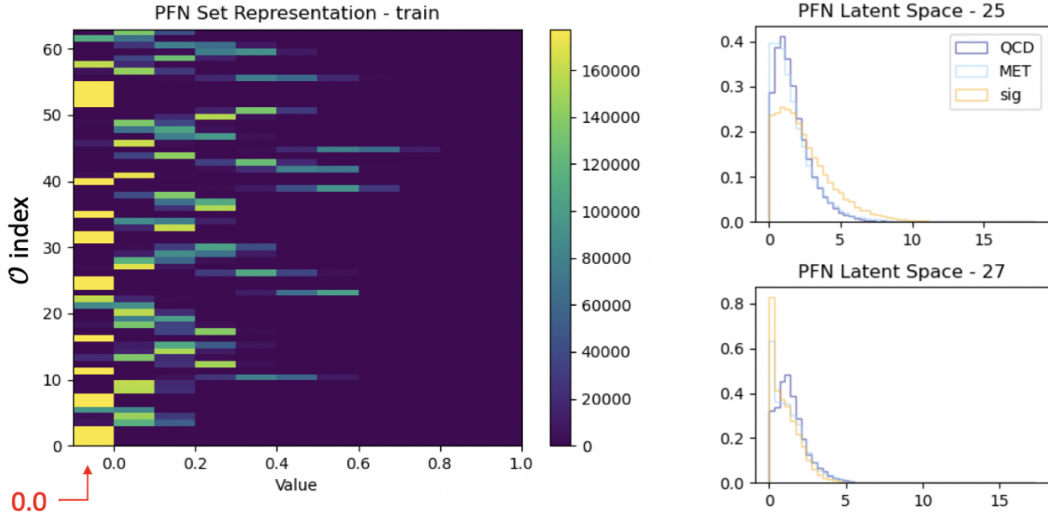


Figure 7.14: A visual representation of the 64 PFN latent space variables which create the input of the VAE component of ANTELOPE. The left shows a 2D histogram of the PFN latent space index (0-63) versus the value assumed by that index. The right shows 1D histograms of two particular PFN latent space variables.

1537 two jets, as presented in Section 7.1.1. The track information is encoded to the PFN Φ latent
 1538 space using the pre-trained Φ network (trained according to the steps outline in Section 7.1.1. The
 1539 resulting Φ basis is summed to created the fixed length symmetric representation O . The VAE is
 1540 then trained in an unsupervised way using inputs encoded to O from data events only. The VAE is
 1541 given no knowledge of the signal model during training. It is able to perform anomaly detection
 1542 through an encoder stage which does a lossy compression on the input to a lower-dimensional
 1543 latent space, and a decoder stage that samples from that latent space and generates an output of the
 1544 original dimensionality. By using the reconstruction error as a loss, this process enables the VAE
 1545 to develop a knowledge of the underlying data structure, thereby isolating new out-of-distribution
 1546 events by their high reconstruction error. This strategy is semi-supervised because the tool has
 1547 some knowledge of correct labels (eg. through the PFN latent space embedding) but is followed
 1548 by a data-driven unsupervised stage.

1549 Figure 7.15 provides a diagram of the ANTELOPE architecture.

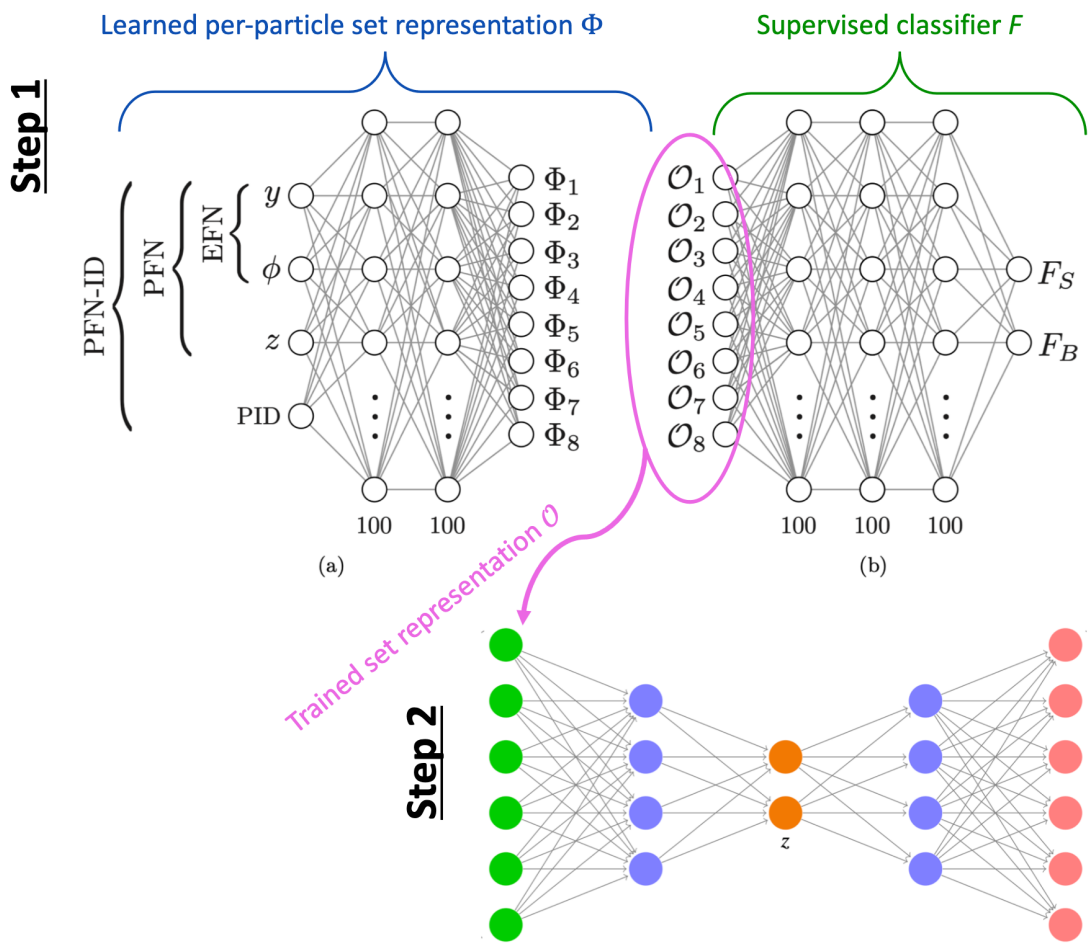


Figure 7.15: An annotated diagram of the ANTELOPE architecture.

1550 **Training**

1551 The VAE stage of the ANTELOPE network is trained directly over a subset of data events
1552 at preselection (6.7 million available, 500,000 used, with a 80% / 20% training/test split). The
1553 input dimensionality of the VAE has to match the encoded Φ dimension of the PFN, in this case
1554 64. The encoder has an encoding layer that brings the dimensionality to 32, and a final layer that
1555 compresses to the latent space dimension of 12. The network is trained for 50 epochs, with a
1556 learning rate of 0.00001. The loss \mathcal{L} is the sum of two terms, the mean-squared error (MSE) of
1557 input-output reconstruction, and the Kullback-Leibler divergence (KLD).

$$\mathcal{L} = \sum_i L_i = \sum_i |\Phi_i^2 - \Phi'_{\ell i}|^2 + \lambda D_{\text{KL}} \quad (7.2)$$

1558 As the PFN inputs are sufficiently normalized to remove any spurious information from train-
1559 ing, no additional normalization is applied to the PFN encoded inputs. The final ANTELOPE score
1560 used in the analysis is produced by applying a log + sigmoid transformation function to the total
1561 evaluated loss \mathcal{L} .

Figure 7.16 shows the loss during training.

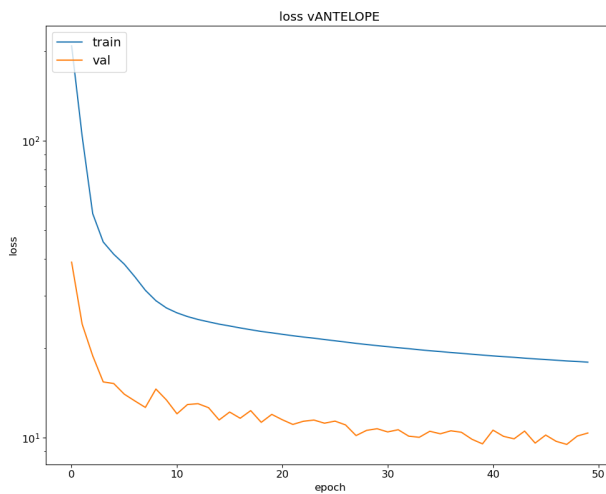


Figure 7.16: ANTELOPE architecture loss during training as a function of epoch.

1562

1563 **Performance**

1564 As with the PFN, the ANTELOPE performance is assessed via the area-under-curve (AUC) of
1565 the receiver operating characteristic (ROC) associated to evaluating the ANTELOPE on the test
1566 set of signal and background events. Figure 7.17 shows the output score distribution in data and
1567 total background MC, showing a very flat ratio and motivating the use of MC for studies of the
1568 ANTELOPE score.

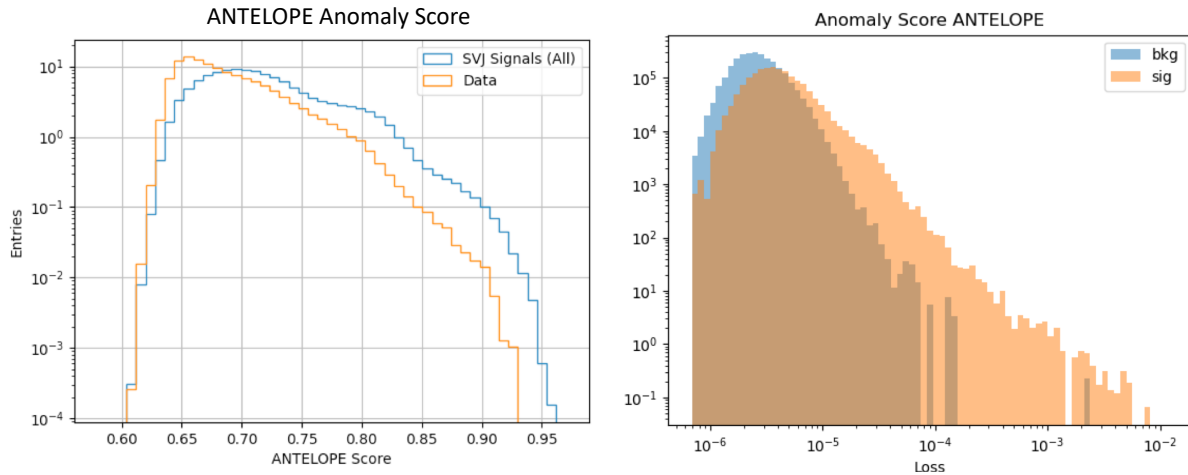


Figure 7.17: ANTELOPE score distribution comparing data and the total background MC (left), with good agreement observed between data and simulated background, and comparing all background MC to signals (right), revealing good discrimination power.

1569 Figure 7.18 shows the AUC of the ANTELOPE across the SVJ signal grid, demonstrating
1570 strong discrimination capability even in the varying corners of phase space. Compared to the
1571 supervised PFN method, the ANTELOPE is not as performant (as expected due to the absence of
1572 signal model in training). However, a selection on events with high ANTELOPE score nonetheless
1573 provides a 10-40% increase in signal significance by removing background and isolating the long
1574 tail of anomalous events.

1575 **Model Independence** The unsupervised component of training the ANTELOPE network is ex-
1576 pected to give it a more generalized sensitivity to new physics with E_T^{miss} and jet activity, beyond
1577 the scope of the SVJ grid. To assess this, alternative signal models are evaluated with the trained

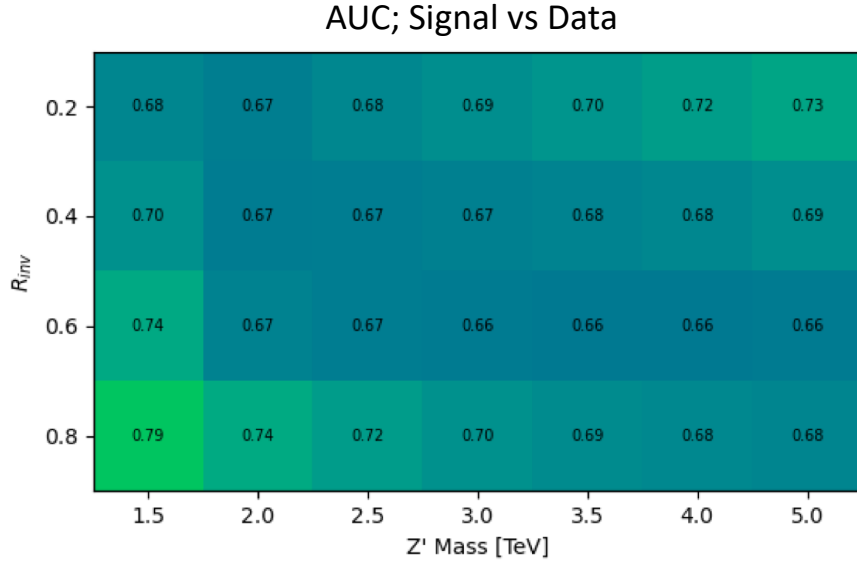


Figure 7.18: AUC from the ANTELOPE score for each signal in the SVJ grid.

1578 ANTELOPE network, as optimized for the SVJ grid, and their sensitivity in the analysis selection
1579 is evaluated.

1580 The following alternate signal models were considered:

- 1581 • $Z' \rightarrow t\bar{t}$
- 1582 • $W' \rightarrow WZ$
- 1583 • Gluino pair production \rightarrow R-hadron + LSP (E_T^{miss}) with gluino masses 2000/3000 GeV, LSP
1584 mass 100 GeV, and lifetime 0.03 ns (LSP = *lightest supersymmetric particle*)
- 1585 • Emerging jets s-channel with mass 1000 GeV and lifetime 1ns

1586 Figure 7.19 shows the distribution of these signals in the PFN score and the ANTELOPE score.
1587 This comparison reveals that ANTELOPE is sensitive to E_T^{miss} in the event; it classifies signals
1588 with no real E_T^{miss} , like the all-hadronic Z' and W' decays (given our imposed lepton veto) as
1589 data-like, but the distributions for signals with E_T^{miss} such as SVJs, R-hadrons, and emerging jets
1590 have distributions with higher anomaly score tails.

1591 Figure 7.20 shows a comparison of the sensitivity of the PFN and ANTELOPE regions across
1592 a variety of signals, including the combined SVJ signal used to train the PFN. The benefit of the

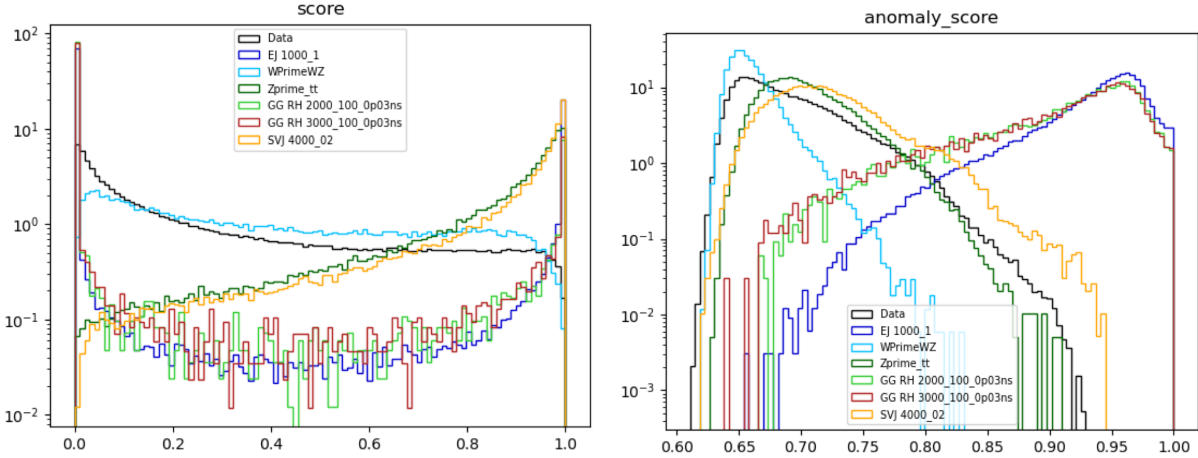


Figure 7.19: Comparing data and the alternate signal models for the PFN score (left) and ANTELOPE score (right). The emerging jet signal is an example of the gain of the model-independent ANTELOPE approach, where it has a bimodal shape in PFN score but is clearly tagged as anomalous by ANTELOPE.

1593 unsupervised stage of ANTELOPE in enhancing model independence is clearly seen through the
 1594 boost in performance for other signal models, namely the gluino and emerging jet signals, which
 1595 have more E_T^{miss} than the W' and Z' signals (all-hadronic) that were also tested. As commented
 1596 above, the PFN outperforms ANTELOPE as expected, because it was designed explicitly for the
 1597 task of classifying SVJs from background, demonstrating the power of supervised learning for the
 1598 model-specific approach.

$\text{sig eff} / \sqrt{\text{bkg eff}}$ for respective score cut (0.6 PFN, 0.7 ANTELOPE)

	EJ 1000	WprimeWZ	Zprime tt	GG RH 2000	GG RH 3000	SVJ
PFN	0.57	0.65	1.92	0.30	0.32	1.97
ANTELOPE	1.73	0.07	0.84	1.72	1.72	1.13

Figure 7.20: Comparing data and the alternate signal models in terms of sensitivity (S/\sqrt{B}) for the PFN and ANTELOPE tools, applying the selection that is used in the analysis. The ANTELOPE network is found to provide significant added sensitivity to alternate signals such as the gluino→R-hadron and emerging jets, which have higher E_T^{miss} than the SVJs.

1599 Studies on the ANTELOPE architecture and comparisons to other methods can be found in
 1600 Appendix B.1.

1601

1602

Chapter 8: Analysis Strategy

1603 This chapter will present the strategies used to isolate ATLAS data events most consistent with
1604 the SVJ model and to estimate the relevant background. The data and MC samples discussed in
1605 Chapter 6 are studied to create the analysis strategy, and the ML scores discussed in Chapter 7
1606 are used to isolate the most signal like events. A *preselection* selects events consistent with the
1607 SVJ topology based on basic features of the jets and E_T^{miss} . Preselected events are then split into
1608 a *control region* (CR), *validation region* (VR), and *signal region* (SR). The CR is used to estimate
1609 the estimate the background and the VR is used to validate that estimation. The SR is blinded
1610 during the development of the analysis strategy, and only unblinded to make the final measurements
1611 presented in Chapter 9. The final result is a polynomial fit of the *transverse mass* (m_T) spectrum
1612 in the SR. The preselection, region definitions, and polynomial fit will be discussed in detail in the
1613 following sections.

1614 **8.1 Preselection**

1615 The preselection isolates the phase space of events that most closely match the SVJ signal
1616 topology. Each cut was determined to reduced the background and enhance signal sensitivity. The
1617 list of preselection cuts and the motivation behind each cut are as follows. Here “jets” refer to
1618 anti- k_t R=0.4 jets, as discussed in Chapter 5.

- 1619 • At least 2 jets; in order to reconstruct the resonance mass
1620 • Leading jet $p_T > 450$ GeV; to ensure the use of the trigger in its efficiency plateau
1621 • Subleading jet $p_T > 150$ GeV; to mitigate the presence of non-collision background (Ap-
1622 pendix B.6.1)

- 1623 • $|\eta_{j1,j2}| < 2.1$; to ensure jets are fully within the tracker
- 1624 • $\Delta Y < 2.8$ (difference in rapidity between the two leading jets); to ensure central production
1625 associated to hard scatter
- 1626 • $E_T^{\text{miss}} > 200 \text{ GeV}$; to focus phase space on events with dark particles
- 1627 • $m_T > 1.2 \text{ TeV}$, to ensure a smoothly falling m_T distribution for fitting (Section 8.4)
- 1628 • At least 3 tracks for each of the two leading jets; to ensure good modeling
- 1629 • $\Delta\Phi(j_1, j_2) > 0.8$; to mitigate the presence of non-collision background (Appendix B.6.1).

A cutflow showing the impact of these cuts in data and signal is shown in Figure 8.1.

Data			Signals - All		
Cut	Statistics	Rel. Efficiency	Cut	Statistics	Rel. Efficiency
Initial	1.71E+10		Init	6.66E+05	
Trigger	3.45E+08	0.0202	Trigger	2.83E+05	0.4245
N. jets ≥ 2	2.84E+08	0.8233	N. jets ≥ 2	2.80E+05	0.9896
Leading Jet Pt $> 450 \text{ GeV}$	1.49E+08	0.5235	Leading Jet Pt $> 450 \text{ GeV}$	2.21E+05	0.7900
Lead Jet Eta < 2.1	1.42E+08	0.9528	Lead Jet Eta < 2.1	2.19E+05	0.9922
Subleading Jet Eta < 2.1	1.33E+08	0.9432	Subleading Jet Eta < 2.1	2.12E+05	0.9661
$dY < 2.8$	1.29E+08	0.9628	$dY < 2.8$	2.11E+05	0.9934
MET > 200	7.07E+05	0.0055	MET > 200	1.13E+05	0.5370
$mT > 1200$	5.38E+05	0.7613	$mT > 1200$	7.94E+04	0.7019
Jet2 pT > 150	5.03E+05	0.9343	Jet2 pT > 150	6.14E+04	0.7739
$d\Phi(j_1, j_2) > 0.8$	4.97E+05	0.9890	$d\Phi(j_1, j_2) > 0.8$	5.83E+04	0.9494

Figure 8.1: Preselection cutflow for data (left) and signal (right).

1630

1631 With the exception of the cuts necessary to reduce the non-collision background, all cuts were
1632 verified to enhance signal sensitivity by improving s/\sqrt{b} , a standard estimate of discovery sensi-
1633 tivity, where s is the number of signal events and b is the number of background events. The cuts
1634 on ΔY and E_T^{miss} were optimized to enhance s/\sqrt{b} , and the other cuts were informed by the physics
1635 motivations provided above.

1636 Vetos are applied to reject any events where an error for a subdetector is flagged. This covers
1637 Tile/LAr calorimeter errors, single event upsets in the SCT, and incomplete events. To reject non-
1638 collision backgrounds (NCB), such as calorimeter noise, beam halo interactions, or cosmic rays,

1639 the standard ATLAS event cleaning procedure is applied. As this analysis is very dependent on
1640 E_T^{miss} associated to jets, the TIGHT event cleaning working point is applied. Tight cleaning requires
1641 jets to pass a stricter set of quality requirements compare to the LOOSE cleaning option. Due to
1642 the alignment between jets and E_T^{miss} in this phase space, it was found that two additional cuts
1643 (indicated above) are needed to remove NCB. The process for selecting these cuts is presented in
1644 Appendix B.6.1.

1645 The two leading in p_T jets in the event are considered as the dark quark candidates. This choice
1646 was determined by truth studies matching the dark quark to reconstructed jets in simulation, which
1647 indicate that the leading p_T assignment allows for high accuracy in ΔR matching to dark quarks.
1648 These studies can be found in Appendix C.

1649 Figure 8.2 and Figure 8.3 show the distribution of signal and background MC in several key
1650 analysis variables after preselection is applied.

1651 **8.2 SVJ Fit and Discovery Analysis Strategies**

1652 As was introduced in Chapter 7 this analysis is interested in achieving dual goals: to make
1653 the best possible measurement of the SVJ signal model generated for this analysis, and to broadly
1654 search for any signals consistent with dark QCD behavior and inconsistent with a Standard-Model-
1655 only background hypothesis. To this end, two parallel analysis strategies are developed.

1656 The SVJ Fit strategy uses the supervised PFN ML score in defining the signal region. Recall,
1657 the PFN is trained over simulated MC background and a combination of all MC SVJ signals. This
1658 gives this ML tool high sensitivity to the particular nuances of the SVJ shower predicted by the
1659 modeled theory. In addition to using the supervised ML tool, the SVJ Fit analysis strategy sets
1660 limits on the expected cross-section of each signal point in the SVJ signal grid. To achieve this, the
1661 shape of the SVJ signals are considered in the final fit, as will be elaborated on Section 8.5.1. The
1662 combination of the supervised PFN ML score and the signal-shape sensitive fitting strategy allows
1663 for the greatest possible sensitivity to the modeled signal process, thus allowing the analysis the
1664 best chance at discovery of this model, or enabling the analysis to set the best possible limits on

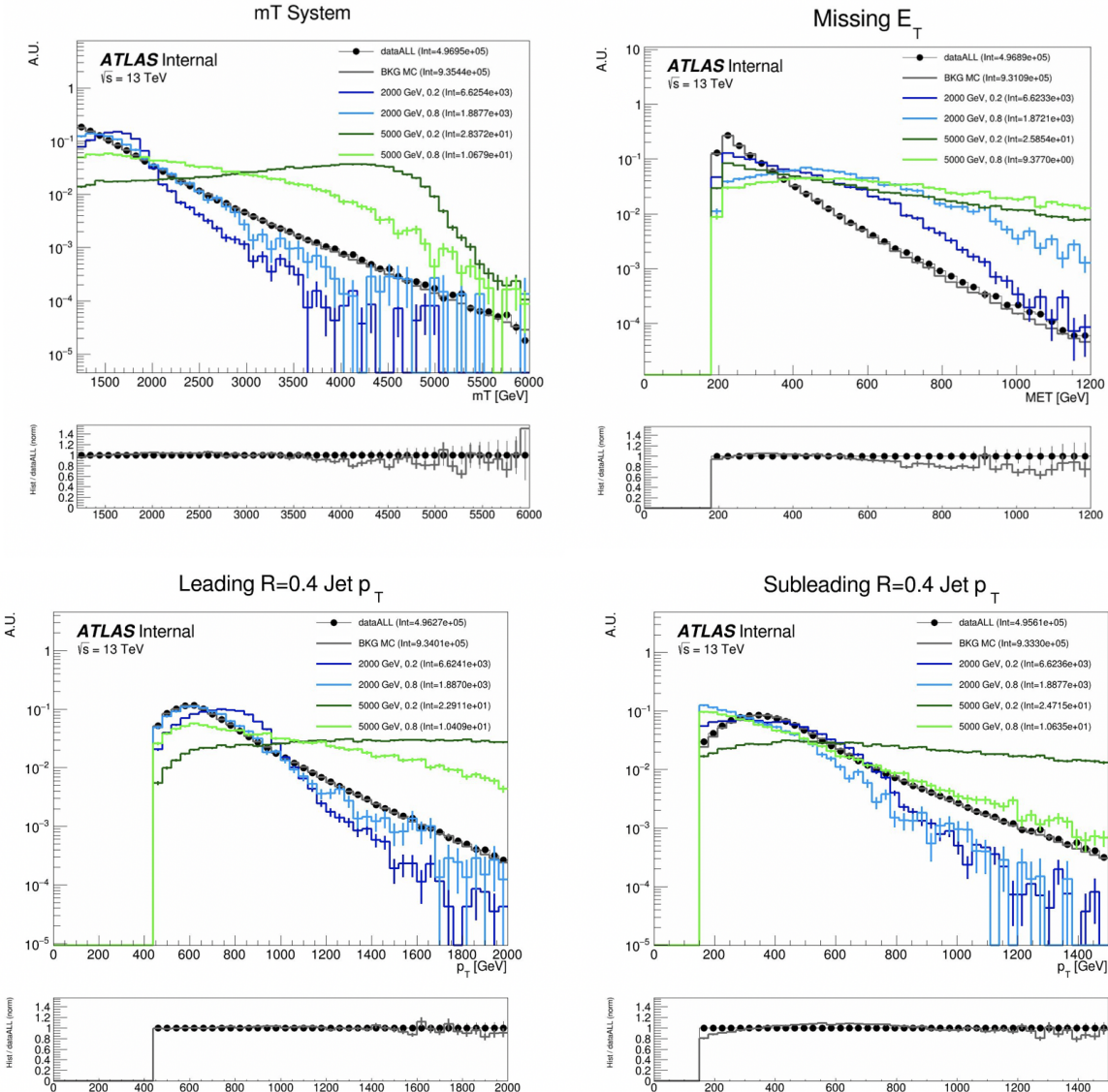


Figure 8.2: Energy and momentum analysis variables at preselection, for data, all background MC and representative signal models. m_T is the key fit variable, and this plot illustrates the smoothly falling background in comparison to the resonant shape of the signals. m_T is further illustrated in Figure 8.9.

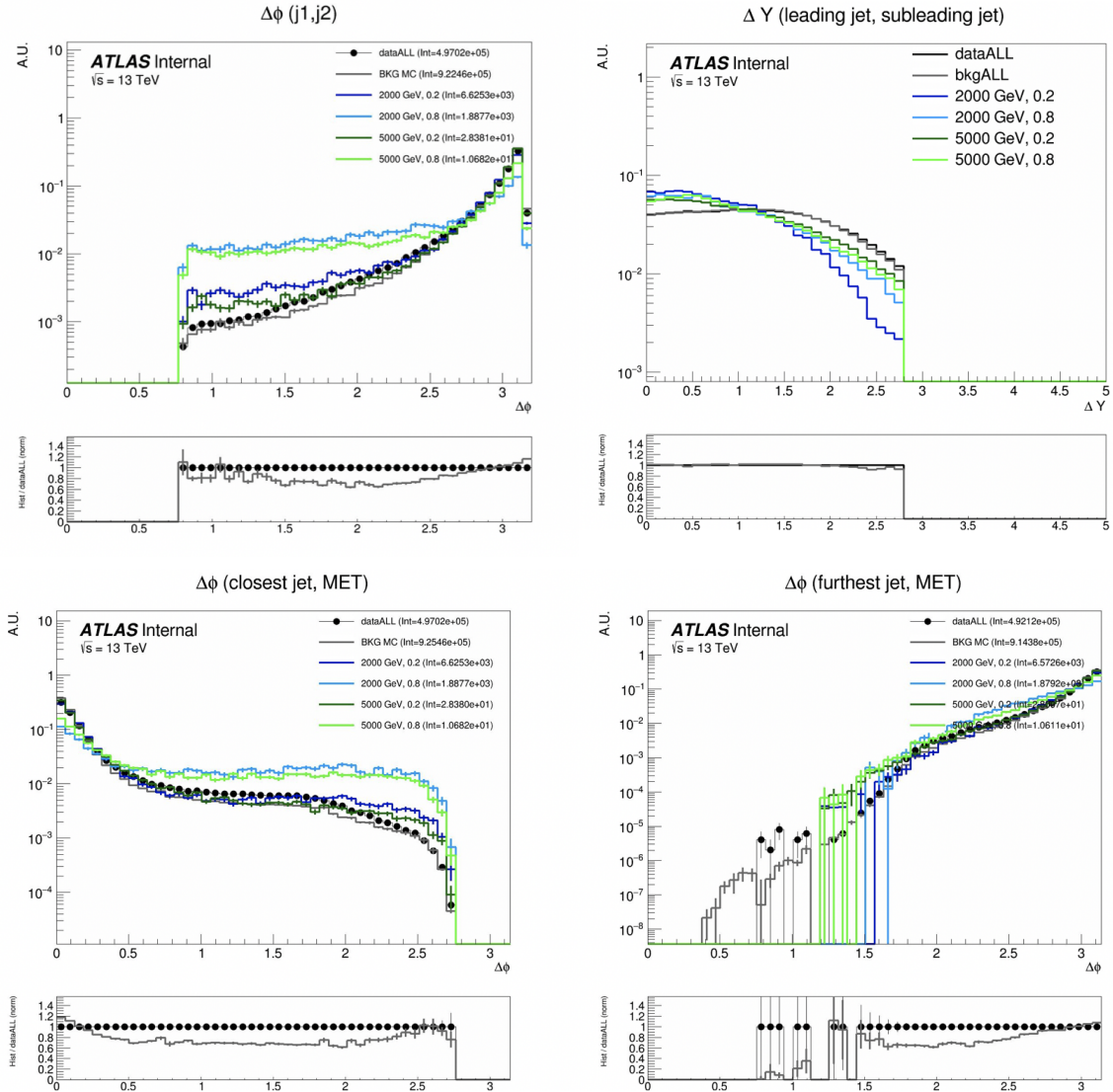


Figure 8.3: Orientation analysis variables at preselection, for data, all background MC and representative signal models. While $\Delta\phi(E_T^{\text{miss}}, j)$ variables are not used explicitly in the analysis flow, they help create a picture of the event.

1665 the observed cross-section.

1666 In contrast, the Discovery analysis strategy attempts to design a more general search, which
1667 could be sensitive to SVJs, but also to other possible hidden valley dark QCD models, such as
1668 fully dark jets or emerging jets [21]. The Discovery analysis strategy uses the semi-supervised
1669 ANTELOPE ML score in defining the signal region. Recall, the ANTELOPE is trained over AT-
1670 LAS data only, with no explicit knowledge of the SVJ signal behavior. The Discovery fit strategy
1671 is also signal model agnostic, by employing a bump hunt [78] strategy, which searches a smoothly
1672 falling template for any bumps inconsistent with a background only hypothesis. Therefore any
1673 signal which could present a resonant signature in m_T could show up as an excess in this strategy.

1674 The details of both strategies will be explored in the follow sections which detail the design
1675 of the signal regions and fit strategies. A diagram demonstrating the analysis flows can be seen in
Figure 8.4. Details on each selection and region can be found in the following subsections.

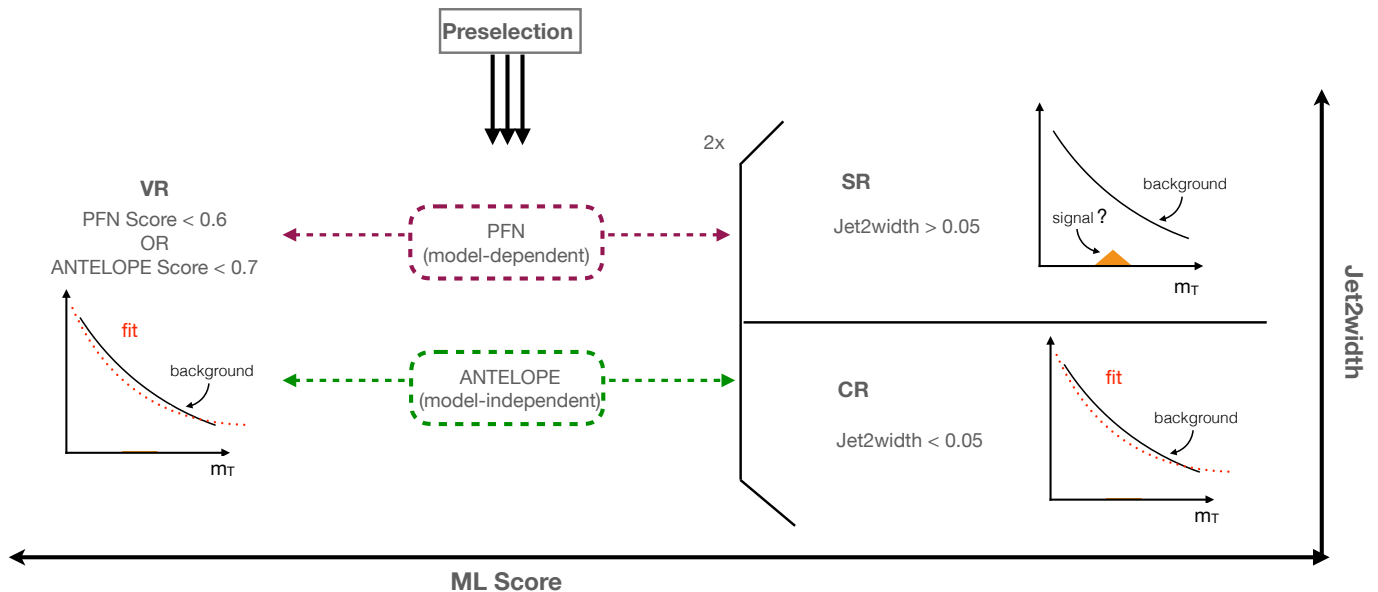


Figure 8.4: Flow of analysis selections, regions, and background estimation/validation fitting strat-
egy. TODO: diagram needs to be corrected

1676

1677 **8.3 Analysis Regions**

1678 **8.3.1 Control and Validation Regions**

1679 The final background estimation will come from a polynomial fit to the m_T distribution in the
1680 signal region. The control and validation regions are needed to develop and test this fit in data.

1681 To define the CR selection, a variable is needed that isolates background from all signals across
1682 the (R_{inv}, m_Z) grid, which is challenging due to the varying nature of the signal models in quantities
1683 such as E_T^{miss} and p_T balance, as illustrated in Figure 8.2. The variable *jet width* is chosen, which
1684 is the calorimeter measurement of the width of a small-R jet as defined by the distance between
1685 the cluster and the jet axis scaled by the jet energy [79]. Figure 8.5 shows this variable specifically
1686 for the subleading jet width, in data, background MC and signal at preselection. The leading jet
1687 width, which was determined to be less useful for isolating signal from background is also shown.
1688 The subleading jet is more likely to be the jet aligned with MET, which is why the signal jet width
1689 is consistently wider in the subleading jet, but not the leading jet. A selection of $\text{width}_{j2} < 0.05$ is
1690 chosen for the CR, with the VR and SR therefore having a selection of $\text{width}_{j2} \geq 0.05$.

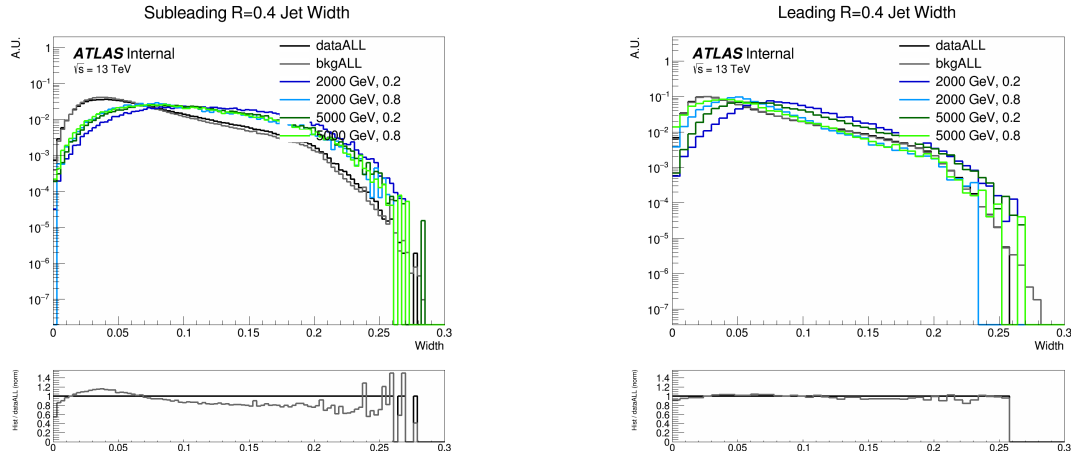


Figure 8.5: Distributions of the subleading jet width width_{j2} (left) and leading jet width width_{j1} (right) in data, background MC and signals at preselection. All SVJ signals are seen to be wider than the background in width_{j2} . The same is not true for width_{j1} , where some signals are observed to closely match the background.

1691 While the CR was used to develop the polynomial strategy, and is the primary region used in

1692 many of the fit studies, a validation region is used as an additional check of the estimation strategy
 1693 in data. The VR is defined using the region of events with low ML score by either the PFN or
 1694 ANTELOPE networks. Here the analysis strategy splits into the two parallel strategies presented
 1695 in Section 8.2: the SVJ fit strategy and the Discovery strategy. A selection of [PFN score ≤ 0.6
 1696 & $\text{width}_{j2} \geq 0.05$] defines the SVJ Fit VR, while [ANTELOPE score ≤ 0.7 & $\text{width}_{j2} \geq 0.05$]
 1697 defines the discovery VR.

1698 There are therefore three variables that are crucial to the analysis strategy: width_{j2} , ML score,
 1699 and m_T . Figure 8.6 shows the correlations of all three variables to one another. Any outstanding
 1700 correlations are shown in Figure 8.7 to not sculpt the m_T distribution and only affect its slope,
 1701 making these variables trustworthy for extrapolation across background/signal regions and final
 fitting procedures.

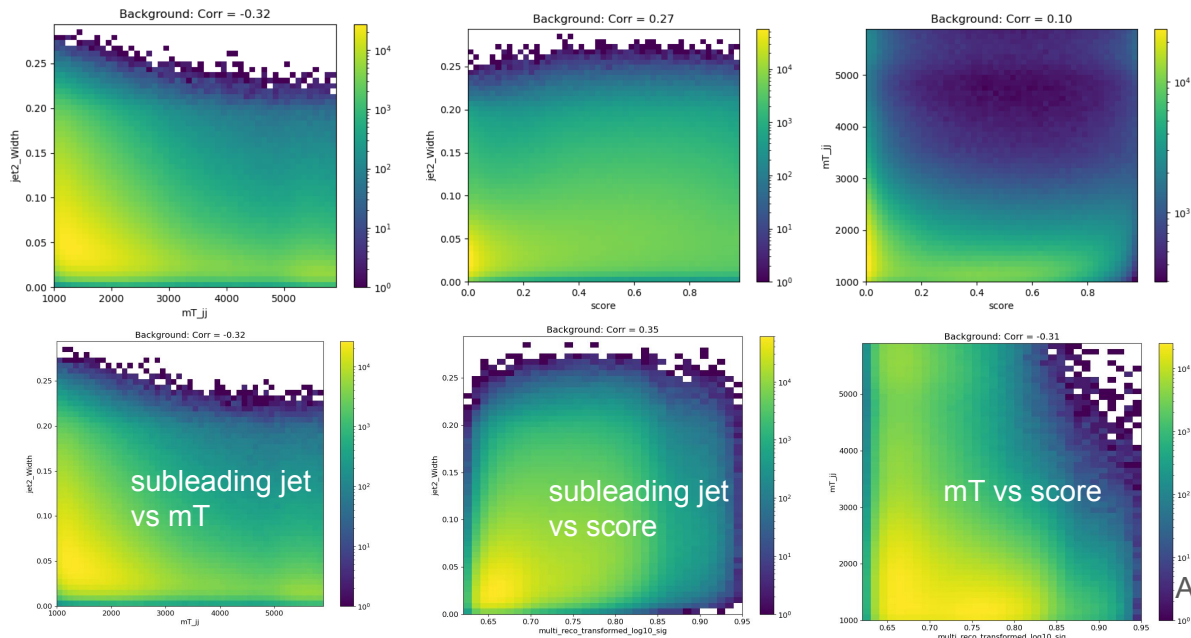


Figure 8.6: 2D plots revealing correlations between width_{j2} and m_T (left), width_{j2} and ML score (middle), and m_T with ML score (right). For the top row, the ML score is the PFN score, and for the bottom three, the ML score is the ANTELOPE score. Minimal correlations are observed and are shown to not sculpt m_T , validating these variables for analysis region construction and statistical treatment.

1702
 1703 The most important variable for shape robustness across the CR, VR, and SR is m_T , as this
 1704 is the variable that is fit for the statistical results. Figure 8.7 shows the distribution of m_T across

1705 the CR, VR, and SR, for both the PFN (supervised) and ANTELOPE (semi-supervised) strategies.
 1706 Some slope is observed in the ratio of the CR to the VR/SR shapes; however, the chosen back-
 1707 ground estimation strategy of polynomial fitting is expected to accommodate this slope. Further,
 1708 the ability of the background polynomial to fit both tail shapes will flex the fit framework in a
 1709 way that will generate higher confidence in the final ability to fit the SR. No significant bumps or
 sculpting are observed.

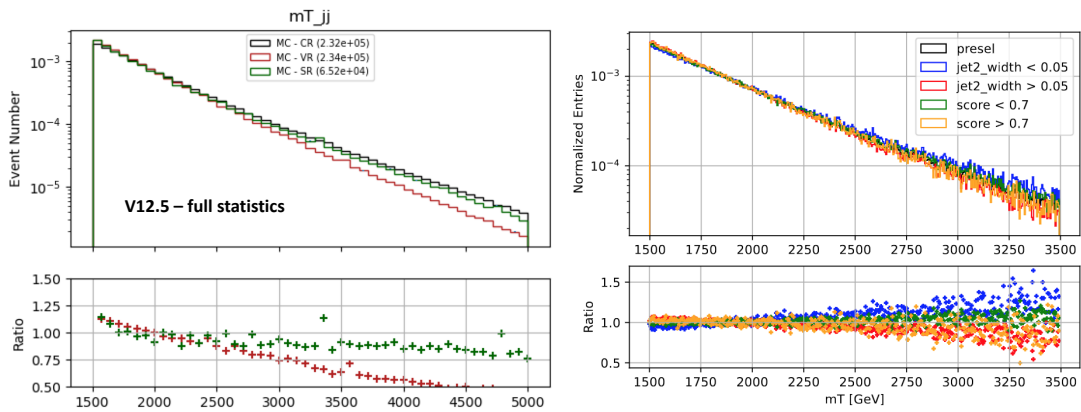


Figure 8.7: m_T in simulation across the CR, VR, and SR for both PFN (left) and ANTELOPE (right) selections.

1710

1711 8.3.2 Signal Region

1712 A selection of PFN score > 0.6 in the SVJ Fit region and ANTELOPE score > 0.7 in the
 1713 Discovery region is made to provide the primary signal-to-background enrichment, as motivated
 1714 by Section 7.1.1. These values are determined to maximize s/\sqrt{b} in each region. The additional
 1715 selection of $\text{width}_{j2} \geq 0.05$ orthogonalizes the SR to the CR. Note that the PFN and ANTELOPE
 1716 regions are not orthogonal; this is because the two analysis flows serve different purposes, their
 1717 statistical treatments are different, and they will not be combined.

1718 A summary of the SR, CR, and VR definitions can be seen in Figure 8.8, along with the relative
 1719 data statistics in each region.

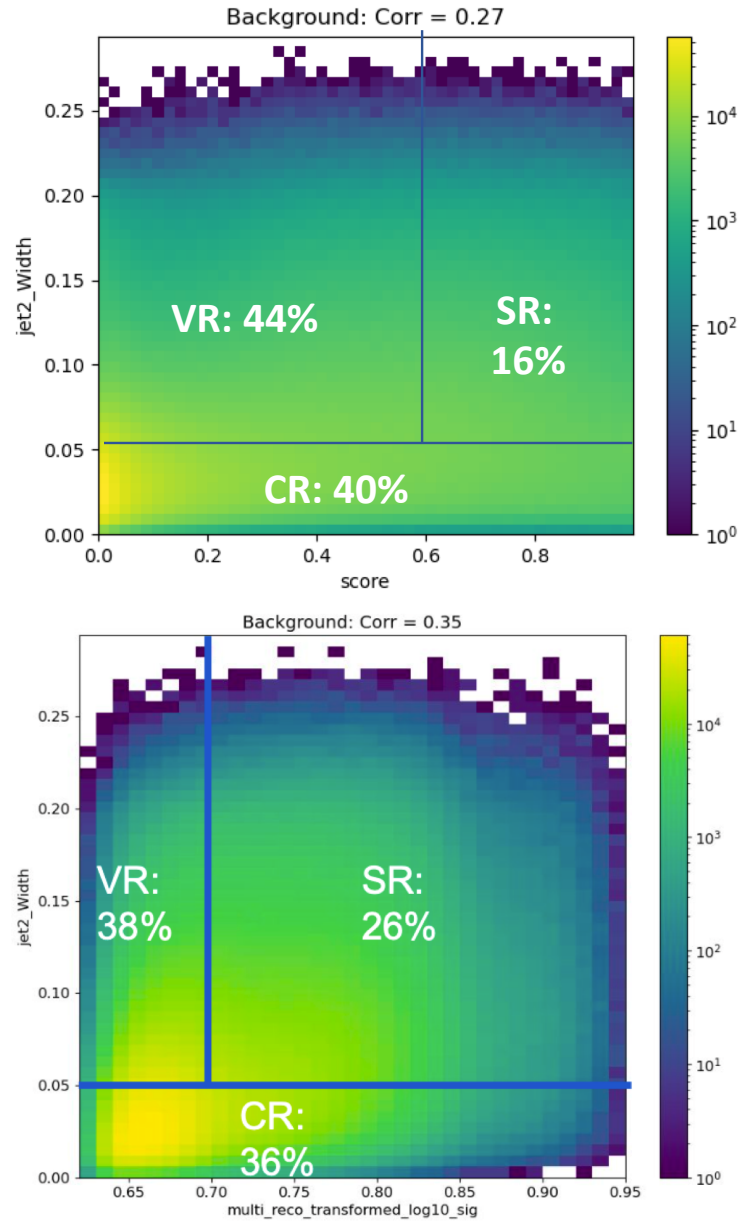


Figure 8.8: Definition of CR, VR, and SR regions using width_{j2} and the ML score, along with the population of each region in data statistics. The SVJ Fit region is shown on top with the PFN score on the x-axis, and Discovery region is shown on the bottom, with the ANTELOPE score on the x-axis.

1720 8.4 Background Estimation

1721 The transverse mass m_T is chosen as the search variable due to the potential for the SVJ signal
 1722 to create a resonant shape around the mass of the Z' . m_T is the total transverse mass of the two
 1723 leading jets and the E_T^{miss} , expressed in Equation 8.1 as:

$$m_T^2 = [E_{T,jj} + E_T^{\text{miss}}]^2 - [\vec{p}_{T,jj} + \vec{p}_T^{\text{miss}}]^2 \quad (8.1)$$

1724 where $E_{T,jj}$ is the transverse energy of the dijet system. We take $E_{T,jj} = m_{jj}^2 + |\vec{p}_{T,jj}|^2$, where
 1725 m_{jj}^2 is the invariant mass of the two leading jets, and $\vec{p}_{T,jj}$ is the vector sum of the p_T of the two
 1726 leading jets. m_T is selected as the search variable in place of simpler invariant mass m_{jj} because
 1727 substantial energy from the Z' decay is captured in the E_T^{miss} . Therefore incorporating E_T^{miss} into
 1728 m_T improves the resonance around the mass of the Z' .

Figure 8.9 illustrates the resonance in m_T of the SVJ signals.

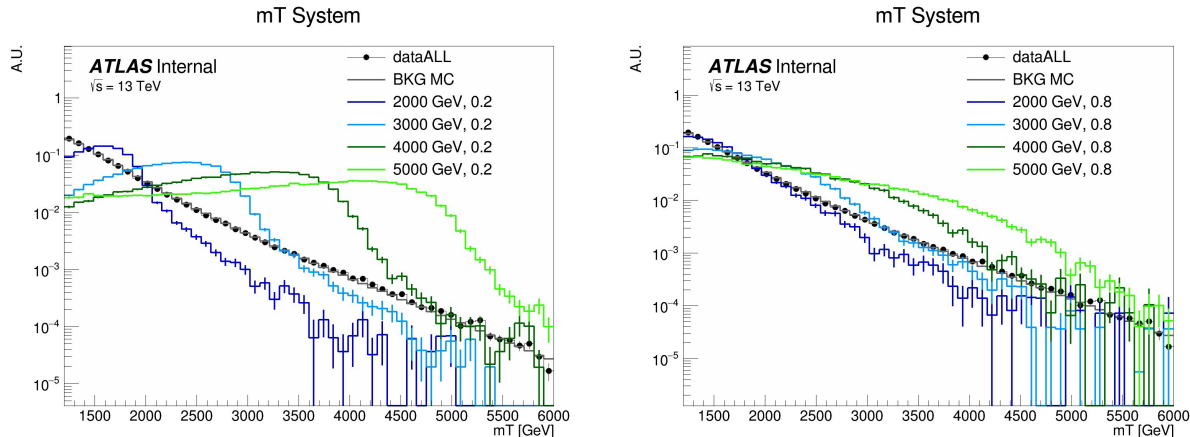


Figure 8.9: The resonant shape of the SVJ signals in m_T , in contrast to the smoothly falling m_T background. The high R_{inv} signals (right) boast a wider shape, making them more difficult to detect, while the low R_{inv} signals (left) produce a more narrow resonance in m_T .

1729
 1730 The SM background in the SR is predominantly composed of QCD events, and due to the poor
 1731 modeling of QCD at high energies by MC, it is estimated in a fully data-driven way. An empirical
 1732 functional form is used for the background shape of m_T . The ability of this function to model
 1733 the background behavior is tested both the CR and the VR for each analysis strategy. The shape

1734 parameters are left free in all the fits.

1735 The fits are performed for $1500 \text{ GeV} < m_T < 6000 \text{ GeV}$. The polynomial chosen is a standard

1736 5-parameter function used in several similar dijet search analyses such as [80] [81] [70] and shown

1737 in Equation 8.2:

$$f(x) = p_1(1 - x)^{p_2}x^{p_3+p_4\ln x+p_5\ln^2 x} \quad (8.2)$$

1738 Here $x = m_{jj}/\sqrt{s}$ and the p_i are free parameters. The fit function is required to be fully positive, and

1739 the m_T distribution is fit to 90 even-width bins. The resulting fit shape is used as the background

1740 estimation for both the SVJ Fit strategy and the Discovery strategy. Validation of the fit and its

1741 ability to both model the background and detect signal are shown in Section 8.5. Higher order

1742 polynomials were also considered, but an F-test was performed and the five parameter function

1743 was determined to be adequate and optimal for capturing the shape of the background.

1744 **8.5 Fit Strategy and Validation**

1745 The steps taken to validate the fitting approach for both the SVJ Fit strategy and the Discovery

1746 strategy will be outlined in the following sections. The signal region fits which comprise the final

1747 result will be presented in Chapter 9.

1748 **8.5.1 SVJ Fit Strategy**

1749 The ability of the five parameter fit function to capture the shape of the background is studied

1750 extensively, using data from the CR and VR. Signal injection tests are performed to determine the

1751 ability of the fit to recover and quantify any SVJ signal excess. Estimates of the expected sensitivity

1752 and the ability to set upper limits on the cross-section of the signal process are also verified.

1753 **Background Only Fits**

1754 Three validations are used for the background fit polynomial: MC across all analysis regions,

1755 data in the CR and VR, and pseudo-data in the CR and VR.

1756 Figure 8.10 shows the ability of this polynomial to fit the smoothly falling m_T background in
 1757 simulation across all 3 analysis regions (CR, VR, SR). The m_T spectrum is fit in 90 even bins.
 1758 These distributions are obtained by downsampling the MC statistics to match the relevant statis-
 1759 tics of the data region, in accordance with the MC weights. The high background-only p -value
 indicates a good fit.

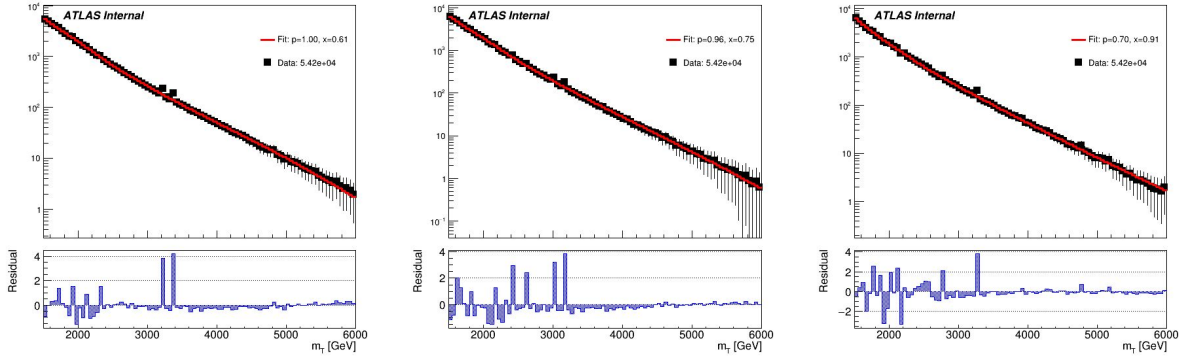


Figure 8.10: Background-only m_T fits using representative MC in the CR (left), VR (middle), and SR (right).

1760
 1761 A slight sinusoidal pattern in the residuals may be observed. This arises due to the “stitching”
 1762 of the p_T slices for the QCD MC (as shown in Figure 6.2), which is picked up by the fit. For this
 1763 reason, fitting to MC is only checked to verify that the differences in the slope of m_T between the
 1764 three regions (as shown in Figure 8.7) do not pose a problem for the fitting strategy.

1765 The nature of the functional fitting method allows it to easily adapt to changes in slope of a
 1766 smoothly falling distribution. Thus validation of the fit can be performed in data using the CR and
 1767 the VR distributions to model the expected behavior in the SR. Figure 8.11 shows the a successful
 1768 fit performed on the full statistics CR and VR regions.

1769 Table 8.1 shows the post-fit values of the fit parameters and their uncertainties for each fit.
 1770 To further validate the fit stability of the fit against potential statistical fluctuations, *pseudo-data*
 1771 (also known as *toy datasets*) are created from the CR data distribution. The pseudo-data is created
 1772 following an *Asimov* prescription [82], using a template to generate a set of toys representing
 1773 different possible statistical fluctuations. When studied as a group, the performance of the pseudo-
 1774 data collection represents the range of possible behavior for an unknown distribution (the SR data

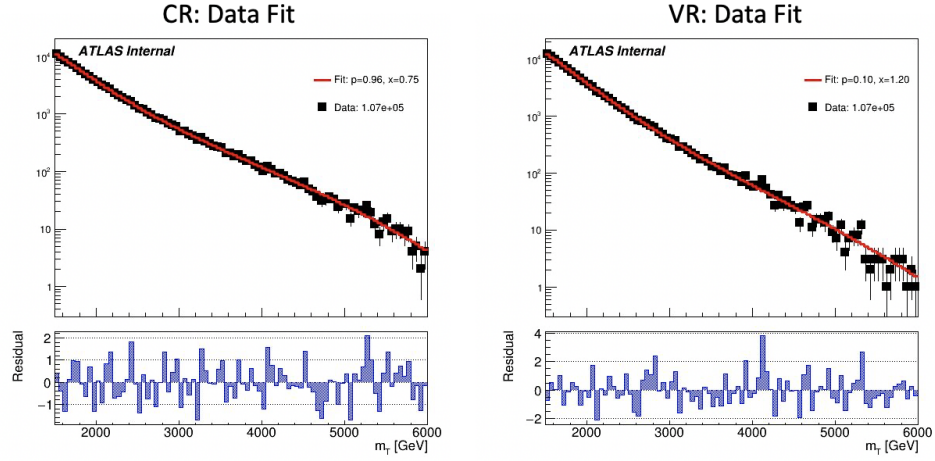


Figure 8.11: Background-only m_T fits using data in the full statistics CR and VR regions.

Parameter	CR		VR	
	Value	Error	Value	Error
p1	1.0716e+05	4.64e+02	1.0686e+05	4.63e+02
p2	4.2479e+01	2.97e+00	3.4279e+01	3.71e+00
p3	5.3888e+01	3.81e+00	4.0798e+01	4.50e+00
p4	2.3804e+01	1.47e+00	1.9424e+01	1.71e+00
p5	3.6683e+00	2.18e-01	3.1583e+00	2.51e-01

Table 8.1: Post-fit parameters for the PFN CR and VR. $p1$ can also be considered N_{bkg} or the normalization factor.

1775 in this case), given its statistical uncertainties.

1776 The template used to generate the pseudo-data is a *smoothed* and *scaled* version of the CR.

1777 The smoothing applied follows the procedure for functional decomposition described in Ref. [83].

Figure 8.12 shows the impact of smoothing on the source data distribution in the CR.

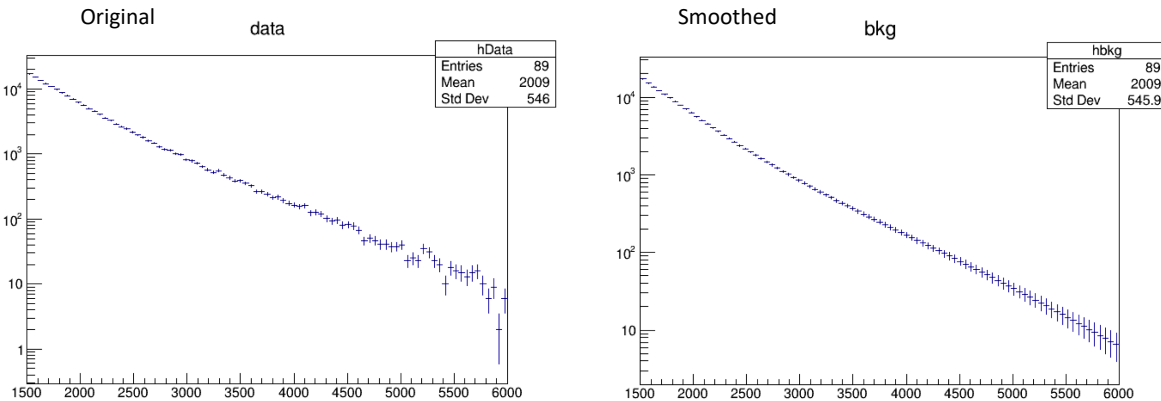


Figure 8.12: m_T distribution in the data CR, before (left) and after (right) smoothing.

1778

1779 The scaling adjusts the statistics of the smoothed template to the expected statistics of the SR.

1780 Recall Figure 8.8, which illustrates that the statistics of the CR and the VR are almost 3x the
1781 expected statistics of the SR. The polynomial fitting strategy is sensitive to the statistics of the
1782 fitted template, so its performance can very substantially depending on the statistical power of the
1783 fitted distribution. To mitigate this, the smoothed template is scaled to the expected statistics of
1784 the SR. Toys are then generated from the smoothed distribution, by varying each bin within its
1785 statistical uncertainty according to a Poisson distribution. Each toy has the same statistical power
1786 as the SR, within statistical uncertainty.

1787 Figure 8.13 shows example fits to three such toy datasets. Figure 8.14 shows the resulting
1788 p-values after an ensemble of 100 Asimov pseudo-datasets are each individually fit. This test
1789 determines the likelihood of exceptionally good (high p-value) or poor (low p-value) fits due to
1790 random statistical fluctuations in the data. A flat distribution is observed, indicating good statisti-
1791 cal behavior.

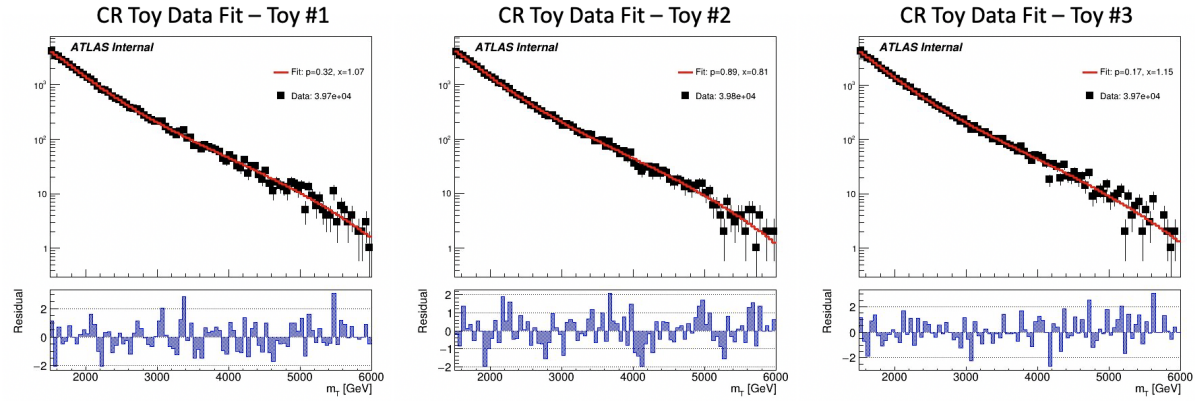


Figure 8.13: Background-only m_T fits using pseudo-data from the CR template.

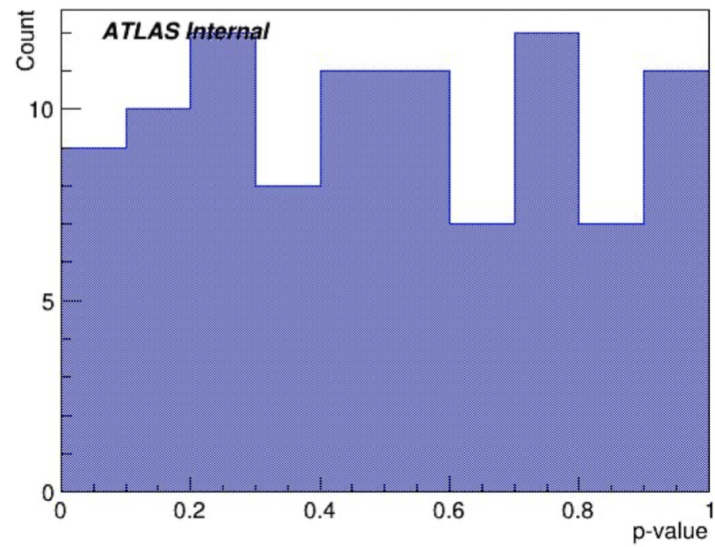


Figure 8.14: p -value histograms from 100 fits to Asimov data in the CR.

1792 **Signal + Background Fits**

1793 Figure 8.15 shows an example of an injected signal into the exclusion region m_T spectrum, and
the ability of the fit framework to accurately fit the number of signal events.

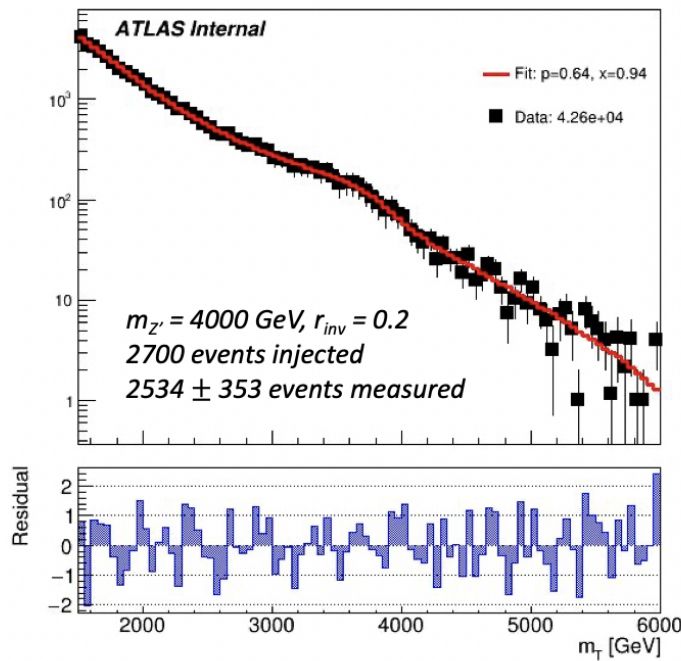


Figure 8.15: Example S+B fit on a background m_T spectrum with injected signal from the point (4000 GeV , $R_{inv}=0.2$).

1794

1795 Signal injection tests demonstrate the a linear relationship between the amount of signal in-
1796 jected and the amount of signal measured by the fit. The signal injection tests are performed in
1797 Asimov datasets to counter the impact of statistical fluctuations in any given template. 50 Asimov
1798 trials are run for all signal points across Z' mass and R_{inv} .

1799 Figure 8.16 provides the results of these tests. The uncertainty of the measurement varies
1800 according to the Z' mass, due to the larger relative background for lower mass points. However,
1801 a strong linear relationship between amount of signal injected and amount of signal measured is
1802 observed for all signal points, which is the key feature.

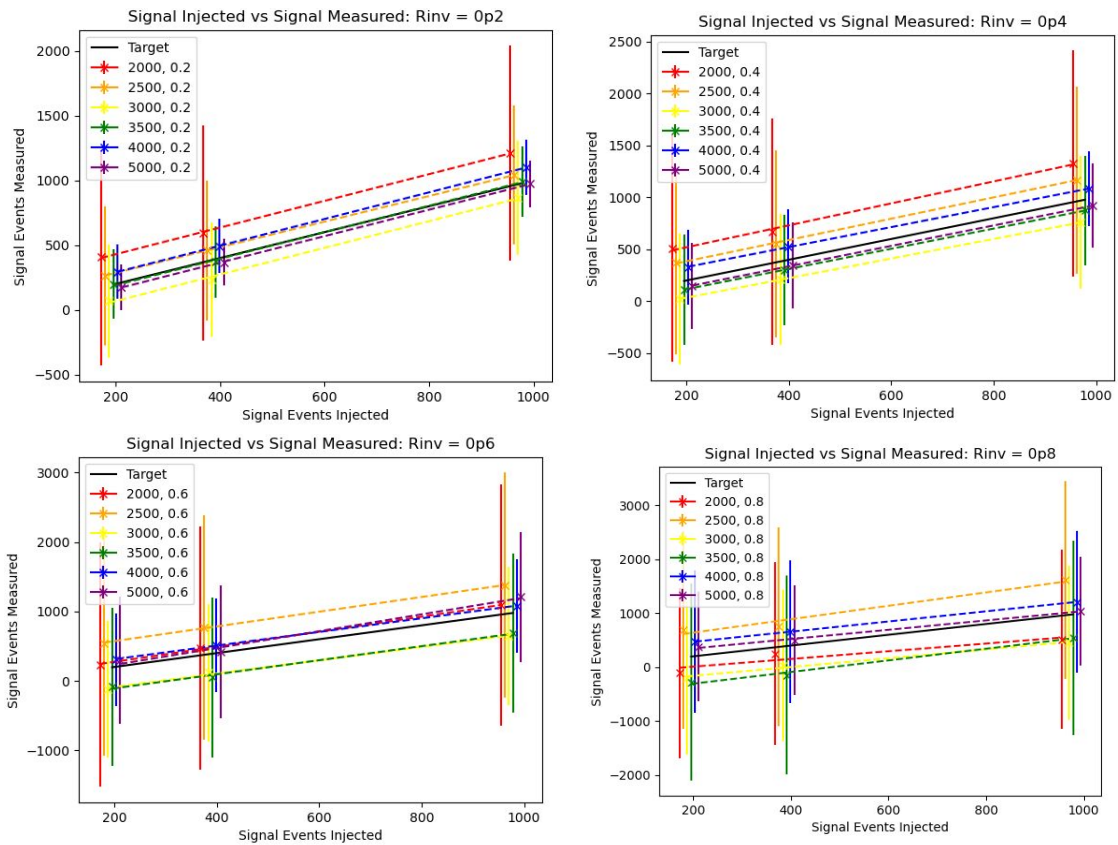


Figure 8.16: Measured signal at a variety of injected values ($1x$, $2x$, and $5x\sqrt{b}$), for all signal points in the grid, $R_{inv}=0.2$ (top left), 0.4 (top right), 0.6 (bottom left), and 0.8 (bottom right).

1803 Expected Sensitivity

1804 Limits on the signal process are obtained by determining the cross section of the signal that can
 1805 be excluded to 95% confidence. Figure 8.17 shows the expected limits obtained from an average
 1806 of 50 Asimov data fits. The limits shown do not include systematics uncertainties in the fit, the
 1807 impacts of which are discussed in Chapter 9.

1808 Considerable exclusion power is predicted for low R_{inv} signal points and lower mass points.
 1809 Higher R_{inv} points present more difficulty due to the very broad signal bump. Higher Z' mass
 1810 points are more difficult to exclude due to the low theory cross-sections.

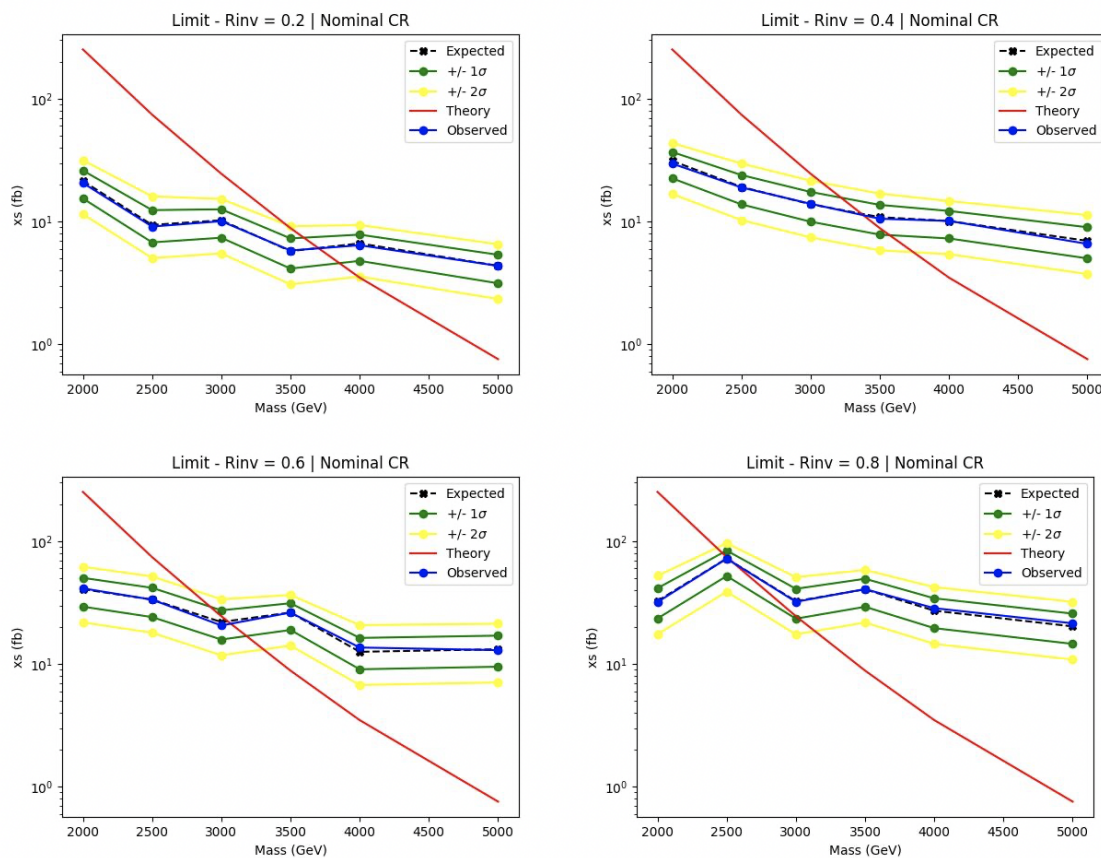


Figure 8.17: 95% C.L. upper limits for signal models across Z' mass, for four different R_{inv} fractions, from the CR region (without systematics). TODO - ATLAS style

1811 The ability of the fit to identify a significant excess is tested by calculating the limits on
 1812 signal injected toys. 2σ and 5σ of signal is injected for each signal point into 50 Asimov data

1813 toys. Figure 8.18 demonstrates the impact of this signal injection on the limit for $R_{inv} = 0.2$.
 1814 The observed limit rises as more signal is injected, indicating the ability of the fit to identify a
 1815 significant signal excess.

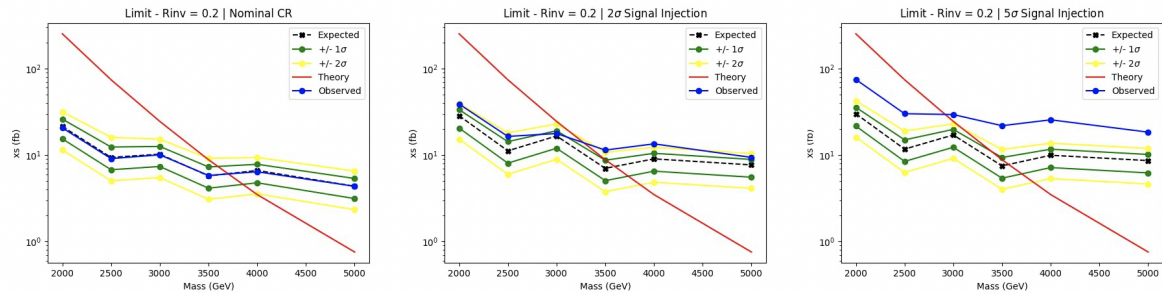


Figure 8.18: 95% C.L. upper limits and observed limit for signal models across Z' mass, with varying amounts of signal injected. TODO - ATLAS style

1816 8.5.2 Discovery Strategy

1817 Model-independent fits for the discovery region are performed using PYBUMPHUNTER [78].
 1818 The strategy consists of comparing the data in a given m_T spectrum of interest to a background
 1819 estimation derived by performing the polynomial fit and sampling from the post-fit function into a
 1820 histogram.

1821 The polynomial fit is done to an m_T distribution with 180 bins (25 GeV wide), half the width
 1822 of the fits in the SVJ Fit region (50 GeV wide). The narrower bins allow for rebinning based on
 1823 the *signal mass resolution* of the SVJ signals. The binning strategy is outlined in Appendix D.1.

1824 Figure 8.19 shows the fit and residuals with of the polynomial with the narrower binning in the
 1825 CR and the Discovery VR data. Table 8.2 shows the post-fit values of the fit parameters and their
 1826 uncertainties for the CR and VR. These results indicate good ability of the 5-parameter polynomial
 1827 to model the ANTELOPE selected data.

1828 The studies shown in Section 8.5.1 validate the robustness of the background polynomial fit.
 1829 The narrower bins are the only difference for polynomial fitting between the SVJ Fit and Discovery
 1830 Fit strategies, and they are not observed to reduce the quality or consistency of the fit.

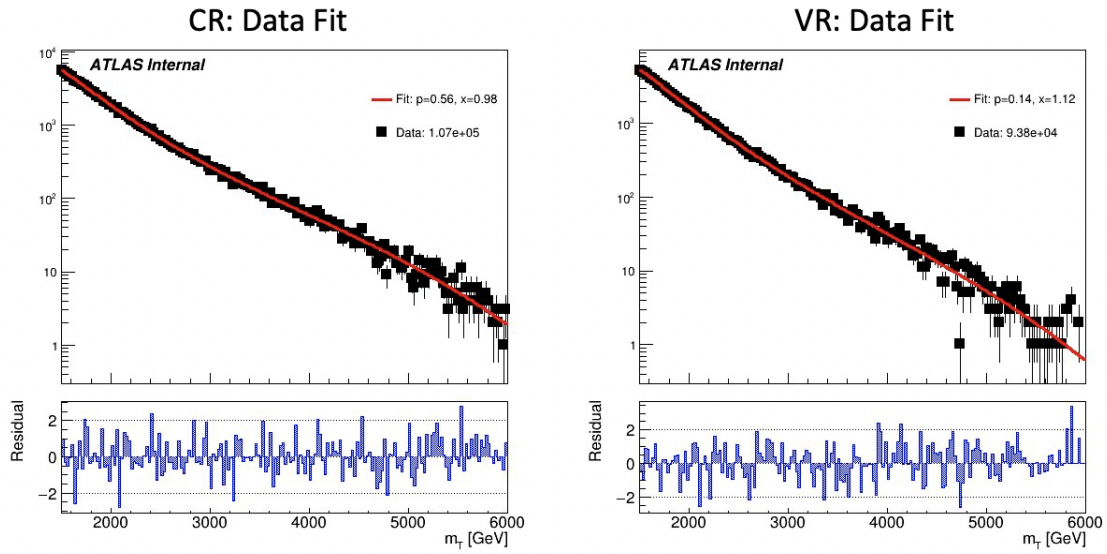


Figure 8.19: Post-fit function and residuals for the ANTELOPE CR and VR.

Parameter	CR		VR	
	Value	Error	Value	Error
p1	1.0709e+05	4.65e+02	9.3776e+04	4.34e+02
p2	4.5945e+01	3.03e+00	4.5787e+01	3.78e+00
p3	5.8566e+01	3.88e+00	5.6014e+01	4.58e+00
p4	2.5593e+01	1.50e+00	2.4914e+01	1.73e+00
p5	3.9196e+00	2.22e-01	3.8809e+00	2.53e-01

Table 8.2: Post-fit parameters for the ANTELOPE CR and VR.

1831 **BumpHunter Fits**

1832 The signal mass resolution binning strategy described in Appendix D.1 creates a monotonically
1833 increasing set of bins. While the SVJ signals help inform the binning, the binning is still broadly
1834 applicable to a variety of potential signal models. The mass resolution of any resonant signal
1835 generally widens as the mass of the mediator particle increases. A similar strategy and binning
1836 was used in the generic heavy resonance search presented in Ref. [77]. The resulting set of 15 bins
1837 to be used in the BumpHunter fits varies in width from 100 GeV at the m_T core to 925 GV in the
1838 m_T tail.

1839 Figure 8.20 shows the result of running BumpHunter over the rebinned CR and VR m_T spectra.
1840 The background estimation is given by polynomial fit function. The high p-values (>0.01) indicate
good agreement with the background estimation.

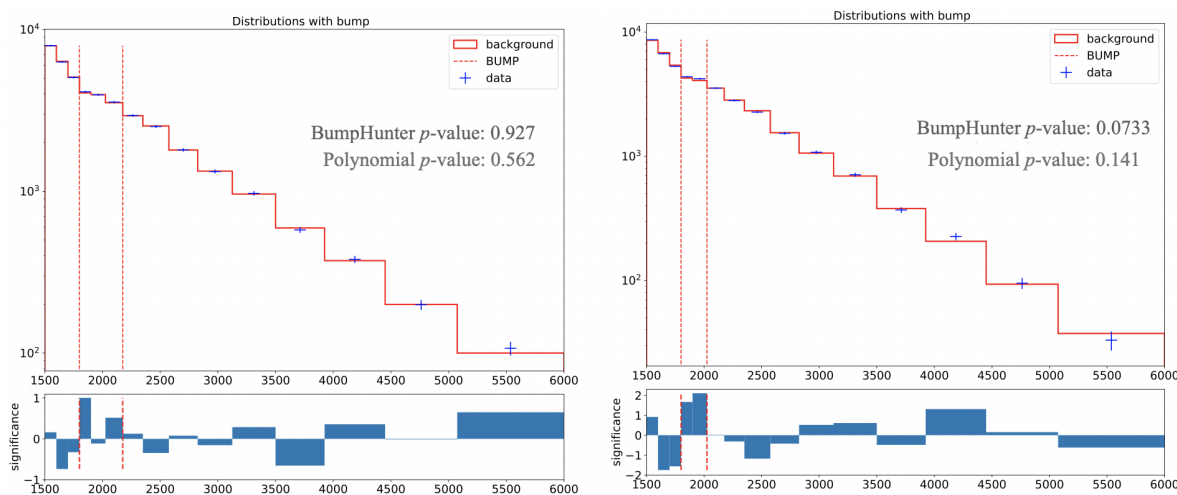


Figure 8.20: BumpHunter fits on the ANTELOPE m_T spectra for both the CR (left) and VR (right). In a signal-depleted region, good agreement with the background estimation is observed.

1841

1842 Figure 8.21 shows BumpHunter p-values over 100 Asimov trials, where each toy is scaled to
1843 the statistics of the SR. The agreement is generally very good, as the p-values trend towards higher
1844 values. No fits with a *spurious signal* are found. A spurious signal would be indicated by a fit with
1845 a p-value < 0.01 , indicating a bump of at least 2σ significance.

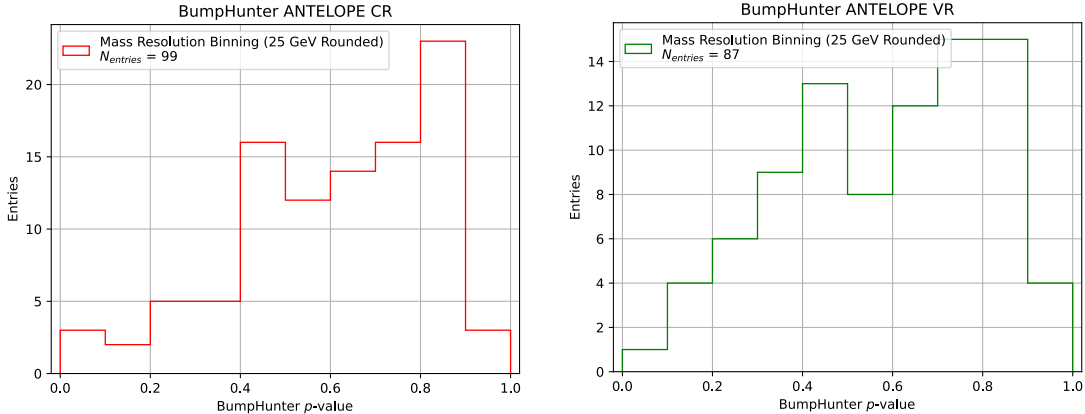


Figure 8.21: BumpHunter p-values extracted for 100 Asimov toys for both the ANTELOPE CR (left) and VR (right).

1846 BumpHunter Signal Injection

1847 To explore a model independent signal hypothesis, signal injection tests in the ANTELOPE re-
 1848 gion are done with generic Gaussian shapes. Two Gaussian models are built with a mean ranging
 1849 from 2000 GeV to 5000 GeV and a standard deviation equal to 10 or 20% the mean value. Fig-
 1850 ure 8.22 illustrates an injected Gaussian and its effect on the m_T distribution. The 20% gaussian
 1851 represents the widest possible signals we might be sensitive to with a BH strategy, while the 10%
 1852 injection represents a narrower signal peak.

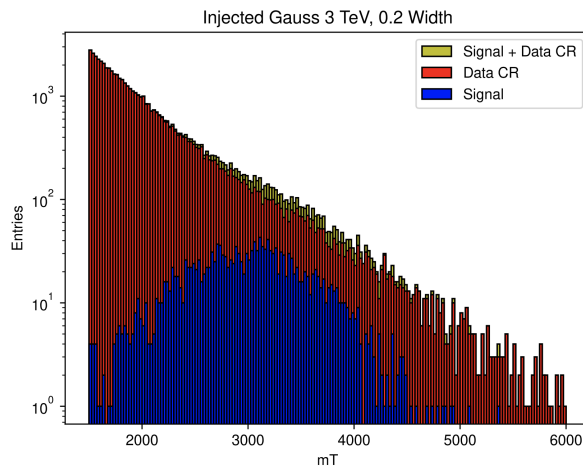


Figure 8.22: Example injected gaussian signal.

1853 An estimated 5σ of signal is injected for these tests. The estimate is derived from the polyno-

1854 mial fitting framework, and is therefore an underestimate, as the flexibility of the polynomial fit
1855 absorbs some of the signal. Therefore we do not expect to measure 5σ significance with the BH
1856 approach, but rather hope to see that some level of signal (at least $\geq 2\sigma$ significance) is observed
1857 by the BumpHunter framework.

1858 Results are obtained by averaging over 100 toys for each injection. Figure 8.23 shows the
1859 resulting max local significance (in an m_T bin) and the location of the determined bump, indicating
1860 a good response of the BumpHunter framework for detecting generic m_T resonances at the right
1861 location. Only the 5000 GeV 20% width point is not properly identified by the framework. While
1862 some sensitivity is lost due to the flexible nature of the fitting framework, the ability to identify a
1863 bump with substantial local significance in the correct location is observed. Figure 8.24 shows an
1864 example of the identified bump.

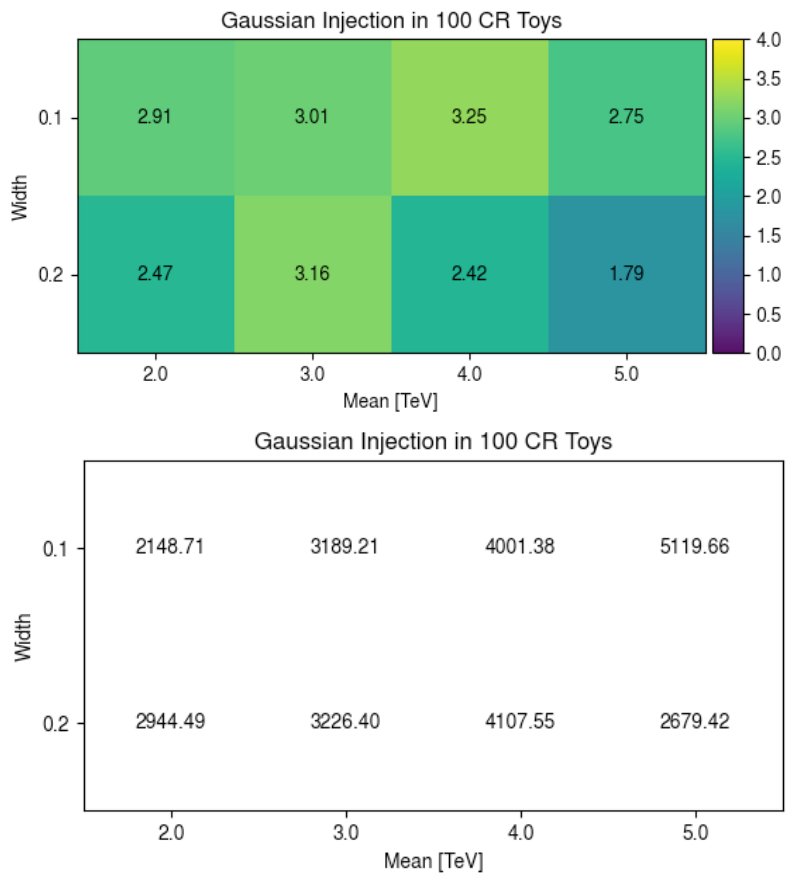


Figure 8.23: Response of the BumpHunter framework to signal injection of 5σ significance to the model-dependent polynomial fit framework. The local significance (top) and bump location (bottom) are shown.

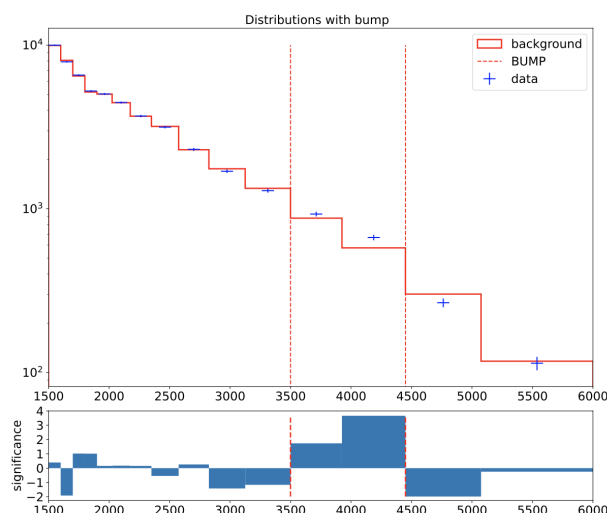


Figure 8.24: Example BH response to gaussian signal injection at 4000 GeV with width of 10%.

Chapter 9: Results

1867 The final results of this analysis are the polynomial fit to the m_T distribution in the SVJ Fit
 1868 SR, and the BumpHunter evaluation of the m_T distribution in the Discovery SR. In the SVJ Fit
 1869 region, systematic uncertainties are evaluated on the signal model, and *limits*¹ on the observed Z'
 1870 production cross-section are set.

1871 **9.1 SVJ Fit Result**

1872 Figure 9.1 shows the unblinded m_T spectrum in the SVJ Fit SR with a background-only fit. The
 1873 fit is successful and has a p-value of 0.265, indicating the data is compatible with the background
 1874 hypothesis. Table 9.1 gives the values and uncertainties for the five parameters of the polynomial
 fit.

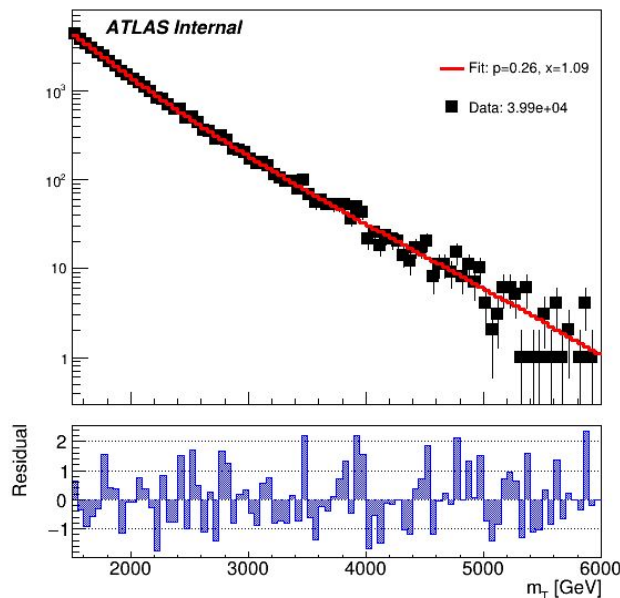


Figure 9.1: m_T in the unblinded SVJ Fit SR with a background-only fit (p-value = 0.265).

¹A limit is an upper bound of the branching ratio of a signal process

Parameter	SR	
	Value	Error
p1	3.9952e+04	2.83e+02
p2	1.8517e+01	9.08e-01
p3	1.4883e+01	4.43e-01
p4	8.0513e+00	1.21e-01
p5	1.3469e+00	3.62e-02

Table 9.1: Post-fit parameters for the PFN SR. $p1$ can also be considered N_{bkg} or the normalization factor.

1876 9.1.1 Systematics

1877 As is typically done in dijet resonance searches using a polynomial fit [84], the systematic un-
 1878 certainties in this analysis are applied only to the signal and not to the background. This is because
 1879 the background expectation is determined entirely from the data in the SR via the polynomial fit.
 1880 Therefore the only uncertainty on the background is the statistical uncertainty, which is reflected
 1881 in the uncertainty associated to each of the five freely floating parameters determined in the fit.

1882 A variety of systematics on the signal shape and yield are considered. The most significant of
 1883 these is the *spurious signal* systematic, which quantifies the level of signal observed in the absence
 1884 of signal injection. Experimental uncertainties on the luminosity and jet reconstruction are studied.
 1885 Finally, uncertainties on the MC simulation of the SVJ theory model are also considered.

1886 Spurious Signal

1887 The spurious signal uncertainty is assessed following the prescription in Ref.[81]. In this pro-
 1888 cedure, the spurious signal is defined using pseudo-data experiments, which are drawn from a
 1889 smoothed template as described in Section 8.5.1. A spurious signal uncertainty is included in the
 1890 fit as a *yield* uncertainty on each signal point.

1891 The spurious signal μ_{spur} is quantified for each signal as the mean number of signal events fitted
 1892 across 100 signal-free pseudo-data experiments. To determine if the amount of spurious signal is

tolerable, the threshold $\mu_{\text{spur}}/\sigma_{\text{spur}} < 0.5$ is used [81]. σ_{spur} for each signal point is the standard deviation on the number of fitted signal events across the 100 pseudo-data experiments. Figure 9.2 gives examples of these pseudo-data experiments, revealing Gaussian distributions from which the mean and standard deviation used for this measurement are taken.

Figure 9.3 shows the $\mu_{\text{spur}}/\sigma_{\text{spur}}$ metric. The requirement for $\mu_{\text{spur}}/\sigma_{\text{spur}} < 0.5$ is easily satisfied across the signal grid.

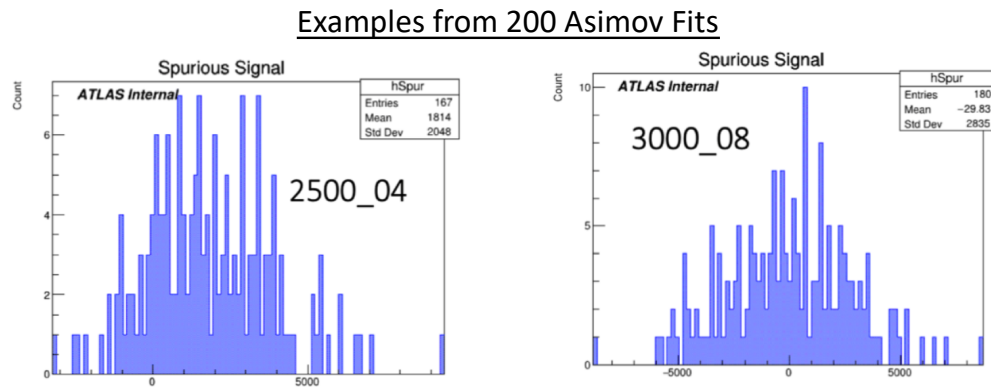


Figure 9.2: Example spurious signal fits, indicating a Gaussian distribution around the mean of spurious signal events.

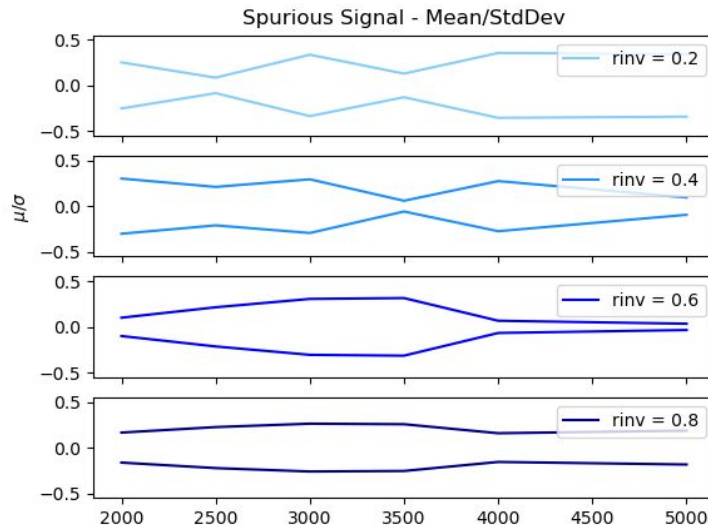


Figure 9.3: Spurious signal as a function of resonance mass. The requirement $\mu/\sigma < 0.5$ is satisfied for all signal points, where μ is the mean number of spurious signal events and σ is the standard deviation of the number of spurious signal events from 100 pseudo-data experiments.

1898

Uncertainty	Effect on Yield [%]
Luminosity	0.83
JES	0.04 - 1.39
JER	0.01 - 0.64

Table 9.2: Summary of Experimental Uncertainties and their impact on the yield of MC signal events.

1899 **Experimental Uncertainties**

1900 The main experimental uncertainties are on the recorded luminosity, *jet energy scale*, and *jet*
 1901 *energy resolution*. The jet energy scale (JES) corrects for the non-compensating calorimeter re-
 1902 sponse and jet energy losses in passive detector material [85]. The jet energy resolution (JER)
 1903 applies a correction based on the ratio between a jet’s true energy and its reconstructed energy,
 1904 as determined in simulation. Systematics uncertainties on the JES and JER processes must be
 1905 considered for any analysis using reconstructed jets.

1906 A flat yield uncertainty of 0.83% is applied for all signals, corresponding to the uncertainty
 1907 reported on the luminosity measurement by the LUCID detector [86].

1908 The JES and JER uncertainties are evaluated on each signal point for their impact on both the
 1909 yield and shape of the m_T distribution. Table 9.2 summarizes the range impact on the yield for
 1910 each uncertainty. The impact of these uncertainties on the signal yield is generally negligible in
 1911 comparison to the spurious signal systematic, which ranges from 4.2% in the case of the lowest
 1912 Z' mass points to >100% in the case of the highest Z' mass points. In the 2000 GeV Z' mass
 1913 case (which has the lowest relative spurious signal uncertainty), the maximum yield difference due
 1914 to experimental uncertainty is 0.53%, or almost an order of magnitude reduced compared to the
 1915 spurious signal uncertainty.

1916 The impact of the JES and JER uncertainties on the shape of the m_T distribution is also consid-
 1917 ered. An example individual JES variation is shown in Figure 9.4, illustrating the minimal impact
 1918 of this uncertainty on the shape of m_T .

1919 To make a conservative estimate of their impact on the shape, all shape uncertainty sources
 1920 are summed in quadrature, bin-by-bin. This results in a maximum “up” variation and a maximum

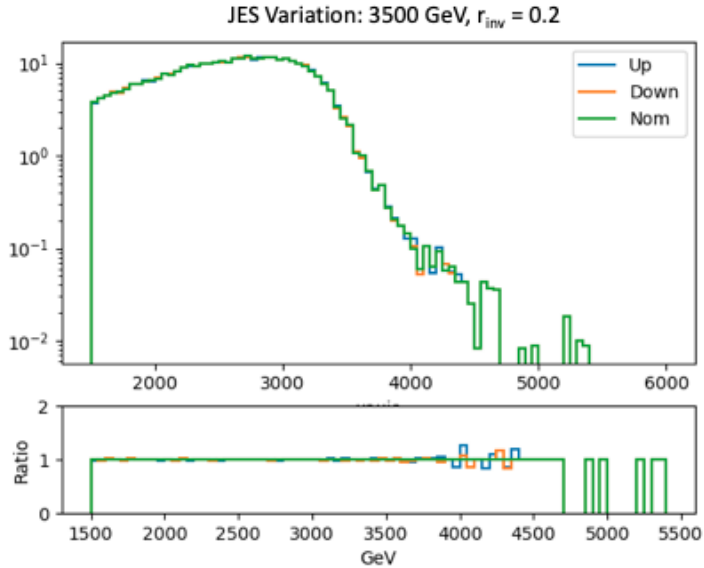


Figure 9.4: m_T of the 3500 GeV Z' , $R_{inv} = 0.2$ signal point, shown with an example JES variation. The nominal shape (“Nom”), 1σ up (“Up”), and 1σ down (“down”) variations are shown. The variation is seen to have a negligible impact on the signal shape.

1921 “down” variation. The the impact of these maximal shape variations on the Z' production cross-
 1922 section limit is evaluated, and uncertainty on this limit is propagated to the final limit bands. The
 1923 impact is generally seen to be quite small, changing the limit variation by 0.2 fb at most. An
 1924 example of the variations summed in quadrature is shown in Figure 9.5.

1925 Theory Uncertainty

1926 Uncertainty on the parameters of the signal model are also considered. The primary theory
 1927 uncertainty source is the tuning of the parton shower in PYTHIA8 [87]. Jet structure and extra
 1928 jet production within the event depend on the modeling of initial state radiation (ISR), final state
 1929 radiation (FSR) and behavior of multiple parton interactions (MPI) within an event. A variety of
 1930 MC generation tuning parameters govern the behavior of ISR, FSR and MPI in the signal genera-
 1931 tion. Ref [88] describes how these parameters are condensed into 10 variations which capture the
 1932 maximal range of impact for these tuning parameters.

1933 The 10 variations (representing 5 up/down variation pairs) are evaluated for the SVJ signal
 1934 shapes. Figure 9.6 provides a look at the effect of these variations on the SVJ m_T signal shape.

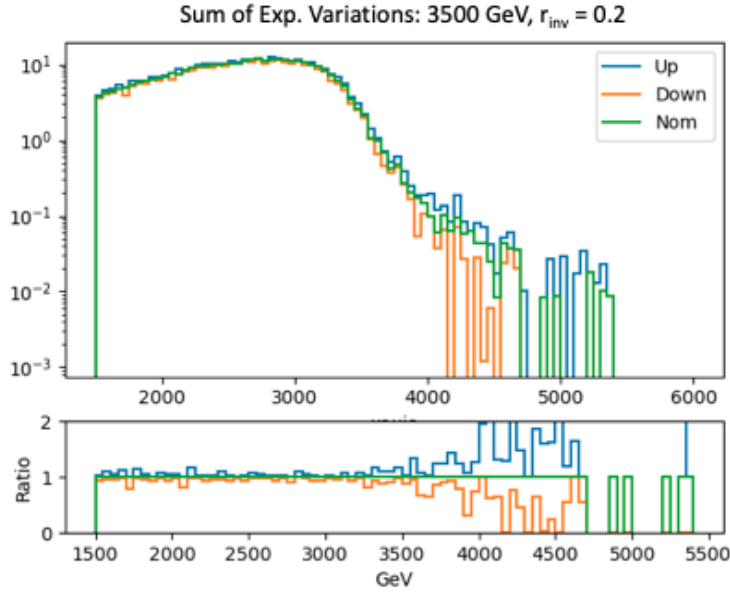


Figure 9.5: m_T of the 3500 GeV Z' , $R_{inv} = 0.2$ signal point, shown with the sum in quadrature of all JES and JER variations. The nominal shape (“Nom”), 1σ up (“Up”), and 1σ down (“down”) variations are shown.

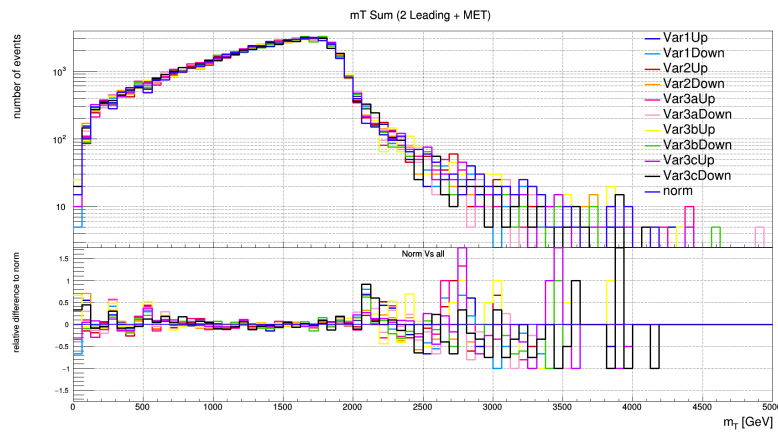


Figure 9.6: Signal distribution of m_T , varying the ISR, FSR and MPI configuration.

1935 All 10 variations are determined to be flat within uncertainty, and thus the systematic is con-
1936 sidered for its impact on the signal yield. The variation in the signal yield is at most 5% (TODO
1937 - determine exactly), which is incorporated into the fitted systematics. The spurious signal uncer-
1938 tainty is dominant for all but the lowest mass signal points.

1939 **9.1.2 Interpretation**

1940 Using a modified frequentist approach [89], *exclusion limits* at the 95% confident level (CL)
1941 are derived. Exclusion limits refer to determining the maximum (or *limiting*) signal cross-section
1942 compatible with the observed data spectrum, such that any theory resulting in a signal cross-section
1943 above the limit is excluded with 95% confidence. The limit is determined from a maximum like-
1944 lihood test statistic [90], which determines the likelihood of observing the given data spectrum
1945 using the background hypothesis, signal hypothesis, and uncertainty parameters. Compatibility
1946 of the signal model with the observed distribution is tested by generating pseudo-data based on
1947 the background estimation and including varying amounts of signal. Through analysis of these
1948 pseudo-data experiments, the maximum number of signals events that is compatible with the ob-
1949 served data distribution can be determined. The 95% confidence level is enforced by dictating that
1950 the number of signal events must be compatible with the observed data within 2σ of uncertainty.

1951 The final limits on the Z' cross section after the implementation of the systematic uncertainties
1952 are shown in Figure 9.7. Exclusion of the theoretical model is observed for the 2000 GeV Z'
1953 mass point for all R_{inv} values. We are unable to exclude the highest mass points due to their low
1954 theoretical cross section, and relatively high spurious signal uncertainty. The most mass points are
1955 excluded for $R_{inv} = 0.2$, which excludes Z' masses up to 3500 GeV.

1956 **9.2 Discovery Result**

1957 Figure 9.8 shows the unblinded m_T spectrum in the Discovery SR with a background-only fit,
1958 and the resulting BumpHunter test. The polynomial fit is successful and has a B-only p-value
1959 of 0.74, indicating the data is compatible with the background hypothesis. The BumpHunter test

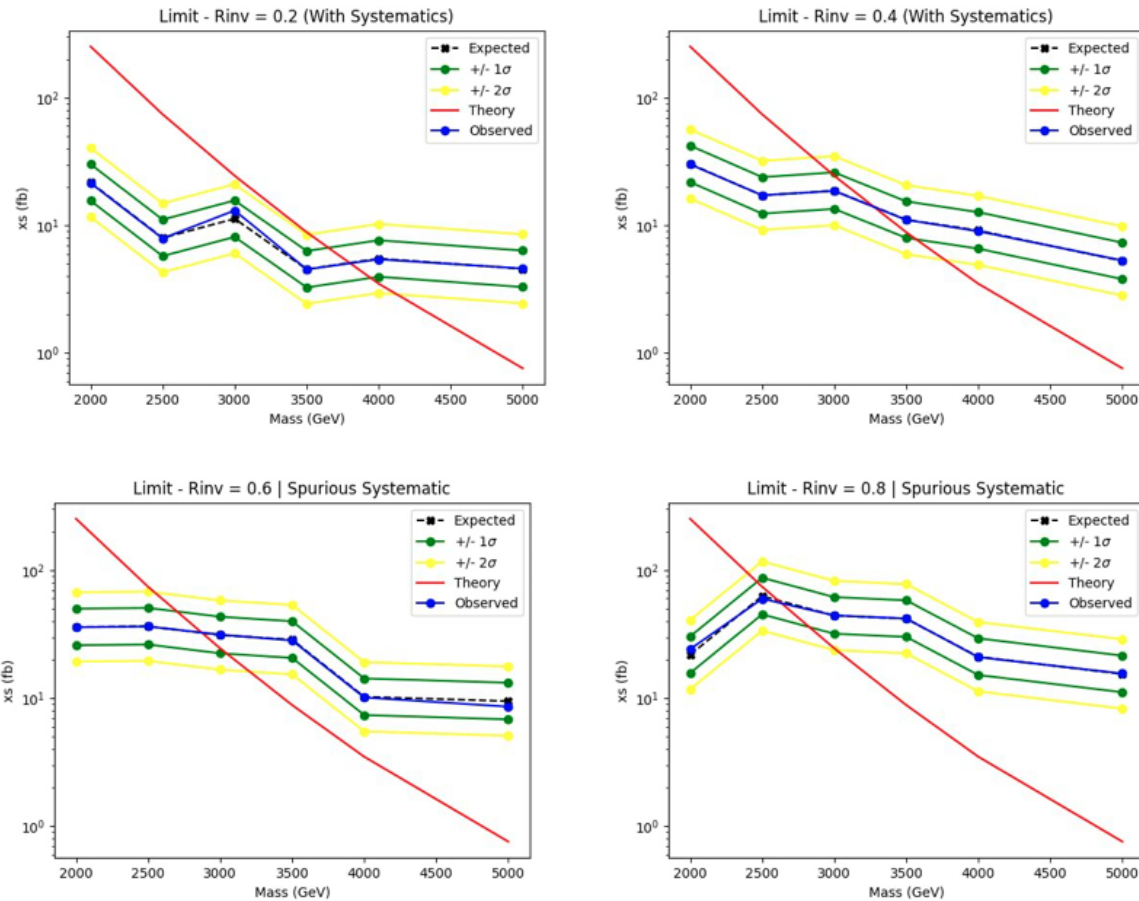


Figure 9.7: Expected and observed 95% CL limits in the unblinded SR, as a function of Z' masses for $R_{inv}=0.2$ (top left), 0.4 (top right), 0.6 (bottom left), 0.8 (bottom right); no systematics.

1960 gives a p-value of 0.8098, indicating no significant excess. The maximum local significance is
 0.877σ .

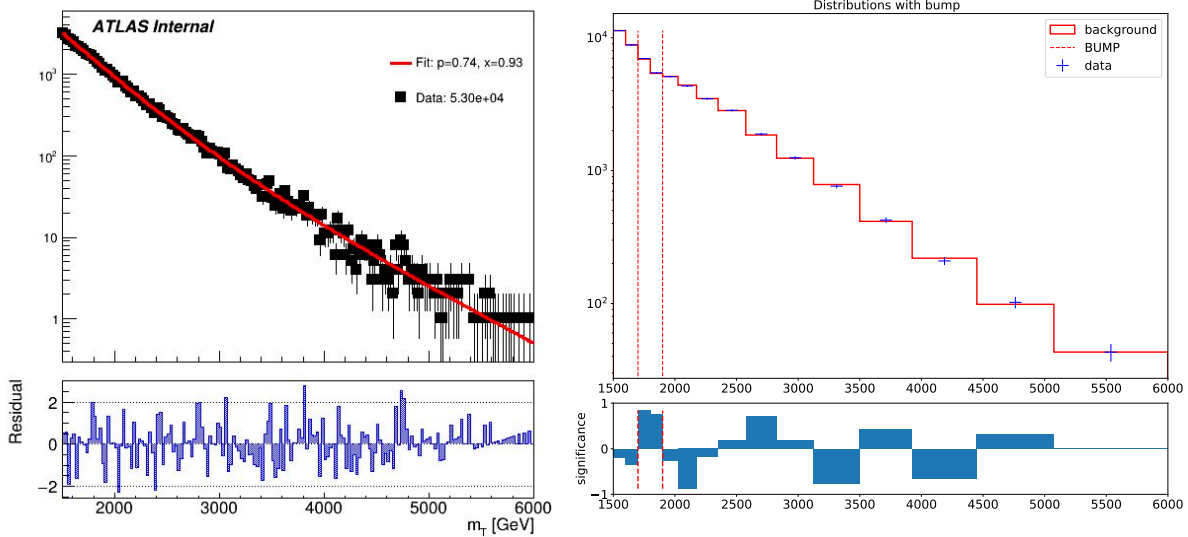


Figure 9.8: m_T in the unblinded ANTELOPE SR with a background-only fit (p-value = 0.74), left. BumpHunter test selecting the most significant data excess with a p-value of 0.8098, right.

1961

1962 Because there is no specific signal interpretation for the Discovery region and both the poly-
1963 nomial fit and BH analysis are entirely data driven, there are no systematics to consider in the
1964 interpretation of the BH result.

1965

Conclusion or Epilogue

1966 Use this page for your epilogue or conclusion if applicable; please use only one of the titles
1967 for this page. Otherwise, you may delete it. Use this page for your epilogue or conclusion if
1968 applicable; please use only one of the titles for this page. Otherwise, you may delete it. Use this
1969 page for your epilogue or conclusion if applicable; please use only one of the titles for this page.
1970 Otherwise, you may delete it. Use this page for your epilogue or conclusion if applicable; please
1971 use only one of the titles for this page. Otherwise, you may delete it. Use this page for your
1972 epilogue or conclusion if applicable; please use only one of the titles for this page. Otherwise,
1973 you may delete it. Use this page for your epilogue or conclusion if applicable; please use only one
1974 of the titles for this page. Otherwise, you may delete it. Use this page for your epilogue or
1975 conclusion if applicable; please use only one of the titles for this page. Otherwise, you may delete
1976 it. Use this page for your epilogue or conclusion if applicable; please use only one of the titles for
1977 this page. Otherwise, you may delete it. Use this page for your epilogue or conclusion if
1978 applicable; please use only one of the titles for this page. Otherwise, you may delete it. Use this
1979 page for your epilogue or conclusion if applicable; please use only one of the titles for this page.
1980 Otherwise, you may delete it. Use this page for your epilogue or conclusion if applicable; please
1981 use only one of the titles for this page. Otherwise, you may delete it. Use this page for your
1982 epilogue or conclusion if applicable; please use only one of the titles for this page. Otherwise,
1983 you may delete it. Use this page for your epilogue or conclusion if applicable; please use only one
1984 of the titles for this page. Otherwise, you may delete it. Use this page for your epilogue or
1985 conclusion if applicable; please use only one of the titles for this page. Otherwise, you may delete

1986 it. Use this page for your epilogue or conclusion if applicable; please use only one of the titles for
1987 this page. Otherwise, you may delete it. Use this page for your epilogue or conclusion if
1988 applicable; please use only one of the titles for this page. Otherwise, you may delete it. Use this
1989 page for your epilogue or conclusion if applicable; please use only one of the titles for this page.
1990 Otherwise, you may delete it. Use this page for your epilogue or conclusion if applicable; please
1991 use only one of the titles for this page. Otherwise, you may delete it. Use this page for your
1992 epilogue or conclusion if applicable; please use only one of the titles for this page. Otherwise,
1993 you may delete it. Use this page for your epilogue or conclusion if applicable; please use only one
1994 of the titles for this page. Otherwise, you may delete it. Use this page for your epilogue or
1995 conclusion if applicable; please use only one of the titles for this page. Otherwise, you may delete
1996 it. Use this page for your epilogue or conclusion if applicable; please use only one of the titles for
1997 this page. Otherwise, you may delete it. Use this page for your epilogue or conclusion if
1998 applicable; please use only one of the titles for this page. Otherwise, you may delete it. Use this
1999 page for your epilogue or conclusion if applicable; please use only one of the titles for this page.
2000 Otherwise, you may delete it. Use this page for your epilogue or conclusion if applicable; please
2001 use only one of the titles for this page. Otherwise, you may delete it. Use this page for your
2002 epilogue or conclusion if applicable; please use only one of the titles for this page. Otherwise,
2003 you may delete it. Use this page for your epilogue or conclusion if applicable; please use only one
2004 of the titles for this page. Otherwise, you may delete it. Use this page for your epilogue or
2005 conclusion if applicable; please use only one of the titles for this page. Otherwise, you may delete
2006 it. Use this page for your epilogue or conclusion if applicable; please use only one of the titles for
2007 this page. Otherwise, you may delete it. Use this page for your epilogue or conclusion if
2008 applicable; please use only one of the titles for this page. Otherwise, you may delete it. Use this
2009 page for your epilogue or conclusion if applicable; please use only one of the titles for this page.
2010 Otherwise, you may delete it. Use this page for your epilogue or conclusion if applicable; please
2011 use only one of the titles for this page. Otherwise, you may delete it. Use this page for your
2012 epilogue or conclusion if applicable; please use only one of the titles for this page. Otherwise,

2013 you may delete it. Use this page for your epilogue or conclusion if applicable; please use only one
2014 of the titles for this page. Otherwise, you may delete it. Use this page for your epilogue or
2015 conclusion if applicable; please use only one of the titles for this page. Otherwise, you may delete
2016 it. Use this page for your epilogue or conclusion if applicable; please use only one of the titles for
2017 this page. Otherwise, you may delete it. Use this page for your epilogue or conclusion if
2018 applicable; please use only one of the titles for this page. Otherwise, you may delete it. Use this
2019 page for your epilogue or conclusion if applicable; please use only one of the titles for this page.
2020 Otherwise, you may delete it. Use this page for your epilogue or conclusion if applicable; please
2021 use only one of the titles for this page. Otherwise, you may delete it. Use this page for your
2022 epilogue or conclusion if applicable; please use only one of the titles for this page. Otherwise,
2023 you may delete it. Use this page for your epilogue or conclusion if applicable; please use only one
2024 of the titles for this page. Otherwise, you may delete it. Use this page for your epilogue or
2025 conclusion if applicable; please use only one of the titles for this page. Otherwise, you may delete
2026 it. Use this page for your epilogue or conclusion if applicable; please use only one of the titles for
2027 this page. Otherwise, you may delete it. Use this page for your epilogue or conclusion if
2028 applicable; please use only one of the titles for this page. Otherwise, you may delete it. Use this
2029 page for your epilogue or conclusion if applicable; please use only one of the titles for this page.
2030 Otherwise, you may delete it. Use this page for your epilogue or conclusion if applicable; please
2031 use only one of the titles for this page. Otherwise, you may delete it. Use this page for your
2032 epilogue or conclusion if applicable; please use only one of the titles for this page. Otherwise,
2033 you may delete it. Use this page for your epilogue or conclusion if applicable; please use only one
2034 of the titles for this page. Otherwise, you may delete it. Use this page for your epilogue or
2035 conclusion if applicable; please use only one of the titles for this page. Otherwise, you may delete
2036 it. Use this page for your epilogue or conclusion if applicable; please use only one of the titles for
2037 this page. Otherwise, you may delete it. Use this page for your epilogue or conclusion if
2038 applicable; please use only one of the titles for this page. Otherwise, you may delete it. Use this
2039 page for your epilogue or conclusion if applicable; please use only one of the titles for this page.

2040 Otherwise, you may delete it. Use this page for your epilogue or conclusion if applicable; please
2041 use only one of the titles for this page. Otherwise, you may delete it. Use this page for your
2042 epilogue or conclusion if applicable; please use only one of the titles for this page. Otherwise,
2043 you may delete it. Use this page for your epilogue or conclusion if applicable; please use only one
2044 of the titles for this page. Otherwise, you may delete it. Use this page for your epilogue or
2045 conclusion if applicable; please use only one of the titles for this page. Otherwise, you may delete
2046 it. Use this page for your epilogue or conclusion if applicable; please use only one of the titles for
2047 this page. Otherwise, you may delete it. Use this page for your epilogue or conclusion if
2048 applicable; please use only one of the titles for this page. Otherwise, you may delete it. Use this
2049 page for your epilogue or conclusion if applicable; please use only one of the titles for this page.
2050 Otherwise, you may delete it. Use this page for your epilogue or conclusion if applicable; please
2051 use only one of the titles for this page. Otherwise, you may delete it. Use this page for your
2052 epilogue or conclusion if applicable; please use only one of the titles for this page. Otherwise,
2053 you may delete it. Use this page for your epilogue or conclusion if applicable; please use only one
2054 of the titles for this page. Otherwise, you may delete it. Use this page for your epilogue or
2055 conclusion if applicable; please use only one of the titles for this page. Otherwise, you may delete
2056 it. Use this page for your epilogue or conclusion if applicable; please use only one of the titles for
2057 this page. Otherwise, you may delete it. Use this page for your epilogue or conclusion if
2058 applicable; please use only one of the titles for this page. Otherwise, you may delete it. Use this
2059 page for your epilogue or conclusion if applicable; please use only one of the titles for this page.
2060 Otherwise, you may delete it. Use this page for your epilogue or conclusion if applicable; please
2061 use only one of the titles for this page. Otherwise, you may delete it. Use this page for your
2062 epilogue or conclusion if applicable; please use only one of the titles for this page. Otherwise,
2063 you may delete it. Use this page for your epilogue or conclusion if applicable; please use only one
2064 of the titles for this page. Otherwise, you may delete it. Use this page for your epilogue or
2065 conclusion if applicable; please use only one of the titles for this page. Otherwise, you may delete
2066 it.

References

- [1] Jens Erler and Paul Langacker. “Electroweak model and constraints on new physics”. In: (July 2004). arXiv: hep-ph/0407097.
- [2] David J Griffiths. *Introduction to elementary particles; 2nd rev. version*. Physics textbook. New York, NY: Wiley, 2008.
- [3] M. Tanabashi et al. “Review of Particle Physics”. In: *Phys. Rev. D* 98 (3 2018), pp. 847–851.
- [4] E. Noether. “Invariante Variationsprobleme”. In: *Nachr. d. König. Gesellsch. d. Wiss. zu Göttingen, Math-phys. Klasse*, Seite 235-157 (1918). eprint: www.physics.ucla.edu/\sim\cwp/articles/noether.trans/german/emmy235.html.
- [5] J. H. Christenson et al. “Evidence for the 2π Decay of the K_2^0 Meson”. In: *Phys. Rev. Lett.* 13 (1964), pp. 138–140.
- [6] Michael Gronau. “CP Violation in B Meson Decays”. In: *Nuclear Physics B - Proceedings Supplements* 142 (May 2005), 263–270.
- [7] J. E. Augustin et al. “Discovery of a Narrow Resonance in e^+e^- Annihilation”. In: *Phys. Rev. Lett.* 33 (1974), pp. 1406–1408.
- [8] J. J. Aubert et al. “Experimental Observation of a Heavy Particle J ”. In: *Phys. Rev. Lett.* 33 (1974), pp. 1404–1406.
- [9] Martin L. Perl et al. “Evidence for Anomalous Lepton Production in e+ - e- Annihilation”. In: *Phys. Rev. Lett.* 35 (1975), pp. 1489–1492.
- [10] S. W. Herb et al. “Observation of a Dimuon Resonance at 9.5-GeV in 400-GeV Proton-Nucleus Collisions”. In: *Phys. Rev. Lett.* 39 (1977), pp. 252–255.
- [11] F. Abe et al. “Observation of top quark production in $\bar{p}p$ collisions”. In: *Phys. Rev. Lett.* 74 (1995), pp. 2626–2631. arXiv: hep-ex/9503002.
- [12] S. Abachi et al. “Observation of the top quark”. In: *Phys. Rev. Lett.* 74 (1995), pp. 2632–2637. arXiv: hep-ex/9503003.
- [13] K. Kodama et al. “Observation of tau neutrino interactions”. In: *Phys. Lett. B* 504 (2001), pp. 218–224. arXiv: hep-ex/0012035.

- 2094 [14] G. Arnison et al. “Experimental Observation of Lepton Pairs of Invariant Mass Around 95-
 2095 GeV/c**2 at the CERN SPS Collider”. In: *Phys. Lett. B* 126 (1983), pp. 398–410.
- 2096 [15] P. Bagnaia et al. “Evidence for $Z^0 \rightarrow e^+e^-$ at the CERN $\bar{p}p$ Collider”. In: *Phys. Lett. B* 129
 2097 (1983), pp. 130–140.
- 2098 [16] Serguei Chatrchyan et al. “Observation of a New Boson at a Mass of 125 GeV with the
 2099 CMS Experiment at the LHC”. In: *Phys. Lett. B* 716 (2012), pp. 30–61. arXiv: 1207.7235
 2100 [hep-ex].
- 2101 [17] Georges Aad et al. “Observation of a new particle in the search for the Standard Model
 2102 Higgs boson with the ATLAS detector at the LHC”. In: *Phys. Lett. B* 716 (2012), pp. 1–29.
 2103 arXiv: 1207.7214 [hep-ex].
- 2104 [18] K. G. Begeman, A. H. Broeils, and R. H. Sanders. “Extended rotation curves of spiral galaxies:
 2105 Dark haloes and modified dynamics”. In: *Mon. Not. Roy. Astron. Soc.* 249 (1991), p. 523.
- 2106 [19] Y. Ashie et al. “Evidence for an oscillatory signature in atmospheric neutrino oscillation”.
 2107 In: *Phys. Rev. Lett.* 93 (2004), p. 101801. arXiv: hep-ex/0404034.
- 2108 [20] C. Abel et al. “Measurement of the Permanent Electric Dipole Moment of the Neutron”. In:
 2109 *Phys. Rev. Lett.* 124.8 (2020), p. 081803. arXiv: 2001.11966 [hep-ex].
- 2110 [21] Guillaume Albouy et al. “Theory, phenomenology, and experimental avenues for dark showers:
 2111 a Snowmass 2021 report”. In: *The European Physical Journal C* 82.12 (Dec. 2022).
- 2112 [22] Timothy Cohen et al. “LHC searches for dark sector showers”. In: *Journal of High Energy
 2113 Physics* 2017.11 (Nov. 2017).
- 2114 [23] Lyndon Evans and Philip Bryant. “LHC Machine”. In: *Journal of Instrumentation* 3.08
 2115 (2008), S08001.
- 2116 [24] “The ATLAS Experiment at the CERN Large Hadron Collider”. In: *JINST* 3 (2008). Also
 2117 published by CERN Geneva in 2010, S08003.
- 2118 [25] “The CMS experiment at the CERN LHC”. In: *Journal of Instrumentation* 3.08 (2008),
 2119 S08004.
- 2120 [26] “The ALICE experiment at the CERN LHC”. In: *Journal of Instrumentation* 3.08 (2008),
 2121 S08002.
- 2122 [27] “The LHCb Detector at the LHC”. In: *Journal of Instrumentation* 3.08 (2008), S08005.
- 2123 [28] Ana Lopes and Melissa Loyse Perrey. *FAQ-LHC The guide*. 2022.

- 2124 [29] Esma Mobs. “The CERN accelerator complex in 2019. Complexe des accélérateurs du
2125 CERN en 2019”. In: (2019). General Photo.
- 2126 [30] *Pulling together: Super Conducting electromagnets*. <https://home.cern/science/engineering/pulling-together-superconducting-electromagnets>.
2127 Accessed: 2024-01-05.
2128
- 2129 [31] *The High-Luminosity LHC*. <https://voisins.web.cern.ch/en/high-luminosity-lhc-hl-lhc>. Accessed: 2024-01-05.
2130
- 2131 [32] Aad G., et al. (ATLAS Collaboration and CMS Collaboration). “Combined Measurement of
2132 the Higgs Boson Mass in pp Collisions at $\sqrt{s} = 7$ and 8 TeV with the ATLAS and CMS
2133 Experiments”. In: *Phys. Rev. Lett.* 114 (19 2015), p. 191803.
- 2134 [33] O. Aberle et al. *High-Luminosity Large Hadron Collider (HL-LHC): Technical design re-*
2135 *port*. CERN Yellow Reports: Monographs. Geneva: CERN, 2020.
- 2136 [34] The ATLAS Collaboration. “The ATLAS Experiment at the CERN Large Hadron Collider”.
2137 In: *Journal of Instrumentation* 3.08 (2008), S08003.
- 2138 [35] G Aad, B Abbott, and ATLAS Collaboration. “Performance of the reconstruction of large
2139 impact parameter tracks in the inner detector of ATLAS”. In: *Eur. Phys. J. C Part. Fields*
2140 83.11 (Nov. 2023).
- 2141 [36] Joao Pequenao. *Computer Generated image of the ATLAS calorimeter*. 2008.
- 2142 [37] *ATLAS liquid-argon calorimeter: Technical Design Report*. Technical design report. AT-
2143 LAS. Geneva: CERN, 1996.
- 2144 [38] H A Gordon. “Liquid argon calorimetry for the SSC”. In: () .
- 2145 [39] Henric Wilkens and (on behalf of the ATLAS LArg Collaboration). “The ATLAS Liquid
2146 Argon calorimeter: An overview”. In: *Journal of Physics: Conference Series* 160.1 (2009),
2147 p. 012043.
- 2148 [40] *Technical Design Report for the Phase-II Upgrade of the ATLAS Tile Calorimeter*. Tech.
2149 rep. Geneva: CERN, 2017.
- 2150 [41] “Technical Design Report for the Phase-II Upgrade of the ATLAS Muon Spectrometer”. In:
2151 () .
- 2152 [42] L Pontecorvo. “The ATLAS Muon Spectrometer”. In: (2004). revised version number 1
2153 submitted on 2003-07-27 16:31:16.

- 2154 [43] *ATLAS magnet system: Technical Design Report, 1*. Technical design report. ATLAS. Geneva:
 2155 CERN, 1997.
- 2156 [44] 2024.
- 2157 [45] Tommaso Colombo. “Data-flow Performance Optimisation on Unreliable Networks: the AT-
 2158 LAS Data-Acquisition Case”. In: *Journal of Physics: Conference Series* 608 (May 2015),
 2159 p. 012005.
- 2160 [46] Joao Pequenao. “Event Cross Section in a computer generated image of the ATLAS detec-
 2161 tor.” 2008.
- 2162 [47] ATLAS Collaboration. “ATLAS Experiment Implements Heterogeneous Particle Recon-
 2163 struction with Intel oneAPI Tools”. General Photo. 2023.
- 2164 [48] ATLAS Collaboration. “Electron and photon performance measurements with the ATLAS
 2165 detector using the 2015–2017 LHC proton-proton collision data”. In: *Journal of Instrumen-*
 2166 *tation* 14.12 (2019), P12006.
- 2167 [49] Chiara Deponte. “Studies on the properties of non-prompt photons at the ATLAS experi-
 2168 ment”. Presented 16 Aug 2022. Technische Universitaet Dortmund (DE), 2022.
- [50] ATLAS Collaboration. “Muon reconstruction performance of the ATLAS detector in pro-
 ton–proton collision data at $\sqrt{s} = 13 \text{ TeV}$ ”. In: *The European Physical Journal C* 76.5 (2016).
- 2170 [51] Sebastien Rettie. *Muon identification and performance in the ATLAS experiment*. Tech. rep.
 2171 Geneva: CERN, 2018.
- 2172 [52] B. R. Webber. *Fragmentation and Hadronization*. 1999. arXiv: hep-ph/9912292 [hep-ph].
- 2173 [53] Eric M. Metodiev. *The Fractal Lives of Jets* | Eric M. Metodiev — ericmetodiev.com. <https://www.ericmetodiev.com/post/jetformation/>. 2019, note = [Accessed 18-
 2174 05-2024],
- 2176 [54] Steven Schramm. *ATLAS Jet Reconstruction, Calibration, and Tagging of Lorentz-boosted
 2177 Objects*. Tech. rep. Geneva: CERN, 2017.
- 2178 [55] ATLAS Collaboration. “Topological cell clustering in the ATLAS calorimeters and its per-
 2179 formance in LHC Run 1”. In: *The European Physical Journal C* 77.7 (July 2017).
- 2180 [56] ATLAS Collaboration. “Jet reconstruction and performance using particle flow with the
 2181 ATLAS Detector”. In: *The European Physical Journal C* 77.7 (July 2017).

- 2182 [57] Matteo Cacciari, Gavin P Salam, and Gregory Soyez. “The anti-ktjet clustering algorithm”.
2183 In: *Journal of High Energy Physics* 2008.04 (Apr. 2008), 063–063.
- 2184 [58] Matteo Cacciari, Gavin P. Salam, and Gregory Soyez. “FastJet user manual: (for version
2185 3.0.2)”. In: *The European Physical Journal C* 72.3 (Mar. 2012).
- 2186 [59] Stephen D. Ellis and Davison E. Soper. “Successive combination jet algorithm for hadron
2187 collisions”. In: *Physical Review D* 48.7 (Oct. 1993), 3160–3166.
- 2188 [60] M. Wobisch and T. Wengler. *Hadronization Corrections to Jet Cross Sections in Deep-*
2189 *Inelastic Scattering*. 1999. arXiv: hep-ph/9907280 [hep-ph].
- 2190 [61] Gavin P Salam and Gr  gory Soyez. “A practical seedless infrared-safe cone jet algorithm”.
2191 In: *Journal of High Energy Physics* 2007.05 (May 2007), 086–086.
- 2192 [62] Gavin P. Salam. “Towards jetography”. In: *The European Physical Journal C* 67.3–4 (May
2193 2010), 637–686.
- 2194 [63] *A Monte Carlo study of track association to jets for b-tagging*. Tech. rep. Geneva: CERN,
2195 2021.
- 2196 [64] *Flavor Tagging with Track Jets in Boosted Topologies with the ATLAS Detector*. Tech. rep.
2197 All figures including auxiliary figures are available at <https://atlas.web.cern.ch/Atlas/GROUPS/PHYSICS/P>
2198 PHYS-PUB-2014-013. Geneva: CERN, 2014.
- 2199 [65] ATLAS Collaboration. “Performance of missing transverse momentum reconstruction with
2200 the ATLAS detector using proton-proton collisions at $\sqrt{s} = 13$ TeV”. In: *Eur. Phys. J. C*
2201 78.11 (2018), p. 903. arXiv: 1802.08168.
- 2202 [66] ATLAS Collaboration. *Public atlas luminosity results for run-2 of the LHC*. 2024.
- 2203 [67] GEANT4 Collaboration, S. Agostinelli, et al. “GEANT4 – a simulation toolkit”. In: *Nucl.*
2204 *Instrum. Meth. A* 506 (2003), p. 250.
- 2205 [68] Christian Bierlich et al. *A comprehensive guide to the physics and usage of PYTHIA 8.3*.
2206 2022. arXiv: 2203.11601 [hep-ph].
- 2207 [69] Michelangelo L. Mangano, Mauro Moretti, and Roberto Pittau. “Multijet matrix elements
2208 and shower evolution in hadronic collisions: -jets as a case study”. In: *Nuclear Physics B*
2209 632.1–3 (June 2002), 343–362.
- 2210 [70] The CMS Collaboration. “Search for resonant production of strongly coupled dark matter
2211 in proton-proton collisions at 13 TeV”. In: *Journal of High Energy Physics* 2022.6 (June
2212 2022).

- 2213 [71] The ATLAS Collaboration. “Search for non-resonant production of semi-visible jets using
2214 Run 2 data in ATLAS”. In: *Physics Letters B* 848 (Jan. 2024), p. 138324.
- 2215 [72] J. Alwall et al. “The automated computation of tree-level and next-to-leading order differ-
2216 ential cross sections, and their matching to parton shower simulations”. In: *JHEP* 07 (2014),
2217 p. 079. arXiv: 1405.0301 [hep-ph].
- 2218 [73] Jon Butterworth et al. “PDF4LHC recommendations for LHC Run II”. In: *J. Phys. G* 43
2219 (2016), p. 023001. arXiv: 1510.03865 [hep-ph].
- 2220 [74] Peter Skands, Stefano Carrazza, and Juan Rojo. “Tuning PYTHIA 8.1: the Monash 2013
2221 Tune”. In: *Eur. Phys. J. C* 74.8 (2014), p. 3024. arXiv: 1404.5630 [hep-ph].
- 2222 [75] Patrick T. Komiske, Eric M. Metodiev, and Jesse Thaler. “Energy flow networks: deep sets
2223 for particle jets”. In: *Journal of High Energy Physics* 2019.1 (2019).
- 2224 [76] A. Kahn et al. “Anomalous jet identification via sequence modeling”. In: *Journal of Instru-
2225 mentation* 16.08 (Aug. 2021), P08012.
- 2226 [77] Georges Aad et al. “Anomaly detection search for new resonances decaying into a Higgs
2227 boson and a generic new particle X in hadronic final states using $\sqrt{s} = 13$ TeV pp collisions
2228 with the ATLAS detector”. In: *Phys. Rev. D* 108 (2023), p. 052009. arXiv: 2306.03637
2229 [hep-ex].
- 2230 [78] Georgios Choudalakis. *On hypothesis testing, trials factor, hypertests and the BumpHunter*.
2231 2011. arXiv: 1101.0390.
- 2232 [79] Peter Loch. “Jet measurements in ATLAS”. In: *J. Phys. Conf. Ser.* 323 (2011). Ed. by Gior-
2233 gio Bellettini, p. 012002.
- 2234 [80] The ATLAS Collaboration. “Search for diboson resonances in hadronic final states in 139
2235 fb $^{-1}$ of pp collisions at $\sqrt{s} = 13$ TeV with the ATLAS detector”. In: *Journal of High Energy
2236 Physics* 2019.9 (Sept. 2019).
- 2237 [81] *Recommendations for the Modeling of Smooth Backgrounds*. Tech. rep. Geneva: CERN,
2238 2020.
- 2239 [82] Glen Cowan et al. “Asymptotic formulae for likelihood-based tests of new physics”. In: *The
2240 European Physical Journal C* 71.2 (Feb. 2011).
- 2241 [83] Ryan Edgar et al. *Functional Decomposition: A new method for search and limit setting*.
2242 2018. arXiv: 1805.04536 [physics.data-an].

[84] “Dijet Resonance Search with Weak Supervision Using

$$\sqrt{s} = 13$$

2243 *pp Collisions in the ATLAS Detector*”. In: *Physical Review Letters* 125.13 (Sept. 2020).

[85] The ATLAS Collaboration. “Jet energy scale and resolution measured in proton–proton collisions at

$$\sqrt{s} = 13$$

2244 TeV with the ATLAS detector”. In: *The European Physical Journal C* 81.8 (Aug. 2021).

[86] The ATLAS Collaboration. “Luminosity determination in pp collisions at

$$\sqrt{s} = 13$$

2245 TeV using the ATLAS detector at the LHC”. In: *The European Physical Journal C* 83.10
2246 (Oct. 2023).

2247 [87] S. Mrenna and P. Skands. “Automated parton-shower variations in pythia 8”. In: *Physical
2248 Review D* 94.7 (Oct. 2016).

2249 [88] *ATLAS Pythia 8 tunes to 7 TeV data*. Tech. rep. All figures including auxiliary figures are
2250 available at <https://atlas.web.cern.ch/Atlas/GROUPS/PHYSICS/PUBNOTES/ATL-PHYS->
2251 PUB-2014-021. Geneva: CERN, 2014.

2252 [89] A L Read. “Presentation of search results: the CLs technique”. In: *Journal of Physics G: Nuclear and Particle Physics* 28.10 (2002), p. 2693.
2253

2254 [90] *Procedure for the LHC Higgs boson search combination in Summer 2011*. Tech. rep. Geneva:
2255 CERN, 2011.

Appendix A: Trigger Studies

2258 Both the lowest unprescaled E_T^{miss} and single small-R jet triggers were considered for this
 2259 analysis. The E_T^{miss} trigger is observed to have higher efficiency for low mass, high R_{inv} points,
 2260 while the single small-R trigger favors high mass, low R_{inv} points. Figure A.1 shows the yields
 2261 and signal efficiencies across the grid for both these strategies.

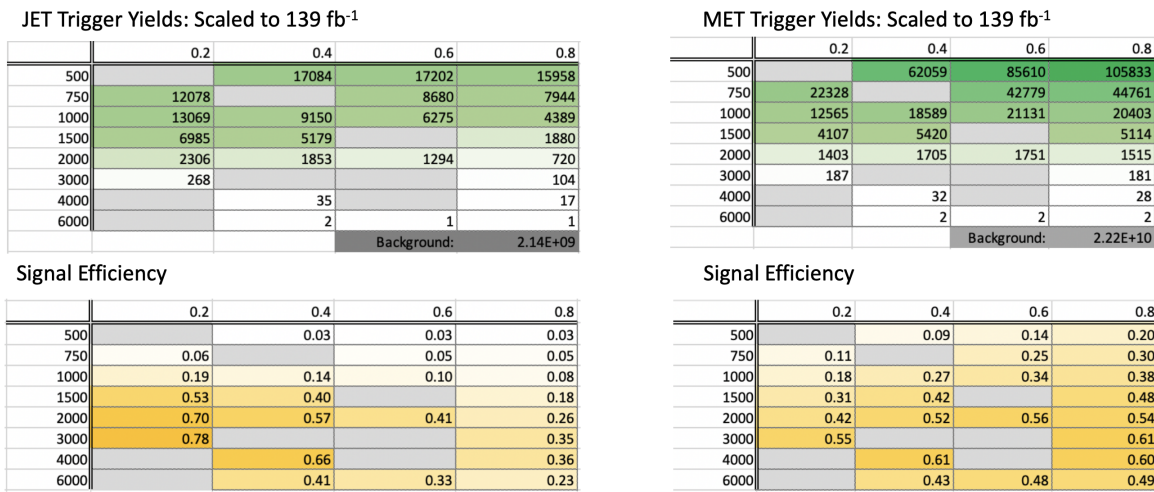


Figure A.1: Trigger yield and efficiency for both the MET trigger and small-R jet trigger approach. Each entry represent a signal point, labelled by the Z' mass and the R_{inv} fraction.

2262 The cross section is higher for the lower Z' mass signal points. As a result, our sensitivity
 2263 to these points and ability to set limits on them is already naturally enhanced. Figure A.2 shows
 2264 the factor of improvement in the inclusive S/\sqrt{B} using each trigger strategy. A cross-check was
 2265 also done calculating S/\sqrt{B} in windows around the mT mass. The results of this cross-check
 2266 confirmed the results shown in Figure A.2.

2267 Figure A.3 shows the ratio of S/\sqrt{B} across the signal grid for the jet trigger compared to the
 2268 E_T^{miss} trigger.

2269 This plot makes clear that the E_T^{miss} trigger favors the low mass, high R_{inv} signal points, while

$(\text{JET Trigger } S/\sqrt{B}) / (\text{Untriggered } S/\sqrt{B})$				
	0.2	0.4	0.6	0.8
500		1.26	1.43	1.53
750	2.99		2.52	2.68
1000	9.24	6.74	5.03	4.07
1500	26.45	20.15		8.83
2000	34.66	28.24	20.57	12.85
3000	39.05			17.35
4000		32.94		17.96
6000		20.57	16.55	11.53

$(\text{MET Trigger } S/\sqrt{B}) / (\text{Untriggered } S/\sqrt{B})$				
	0.2	0.4	0.6	0.8
500		1.43	2.21	3.15
750	1.72		3.86	4.69
1000	2.76	4.26	5.26	5.89
1500	4.83	6.56		7.47
2000	6.55	8.08	8.65	8.40
3000	8.46			9.38
4000		9.51		9.32
6000		6.68	7.43	7.59

Figure A.2: The factor of improvement in S/\sqrt{B} for each trigger method compared to the untriggered case.

	0.2	0.4	0.6	0.8
500		0.89	0.65	0.49
750	1.74		0.65	0.57
1000	3.35	1.58	0.96	0.69
1500	5.47	3.07		1.18
2000	5.29	3.49	2.38	1.53
3000	4.62			1.85
4000		3.46		1.93
6000		3.08	2.23	1.52

Figure A.3: The ratio of S/\sqrt{B} of jet trigger over E_T^{miss} trigger selection.

2270 the single jet trigger favors the high mass, low R_{inv} signal points. A number of considerations led
2271 us to selecting the single jet trigger. First, Figure A.2 illustrates that the sensitivity enhancement is
2272 greater for signals favored by the jet trigger than signals favored by the E_T^{miss} trigger. This indicates
2273 we have more to gain from focusing on the region of our signal grid where the jet trigger is most
2274 efficient. We combined this with the observation that the jet trigger is beneficial for high mass
2275 points where the cross-section is lower and we need to maximize sensitivity to hope to set limits
2276 on these points.

2277 Second, there are a number of analysis variables at our disposal which are more discriminant for
2278 high R_{inv} signals than for low R_{inv} signals. A collection of these variables are shown in Figure A.4.
2279 Given that we had multiple avenues available to enhance sensitivity to low R_{inv} signals through
2280 analysis strategy cuts, we opted for a trigger strategy that benefitted the low R_{inv} signal points.
2281 Additionally, we know E_T^{miss} is highly correlated with these discriminant analysis variables, and a
2282 E_T^{miss} trigger would reduce the effectiveness of these variables. Not implementing the E_T^{miss} trigger
2283 allows us to explore other ways of leveraging E_T^{miss} in the analysis using a cut that is more finely
2284 tuned to the specifics of the signal model than the E_T^{miss} trigger is.

2285 Third, we know that fitting the high R_{inv} mass points would be challenging given their very
2286 broad shapes in the key analysis variable m_T . Given the analysis decision to do a search for
2287 resonant features in m_T , we chose to design a search that emphasized maximizing sensitivity
2288 to the signal points that we were mostly to appear as a resonant feature in m_T . The shape of
2289 m_T and our reduced ability to set limits on high R_{inv} points is demonstrated in the body of this
2290 note. Another search strategy may be more optimal for setting limits on high R_{inv} semi-visible jet
2291 signals, but it is currently outside the scope of this analysis.

2292 A jet or E_T^{miss} trigger was also considered, but abandoned due to concerns about sculpting
2293 features in the smoothly falling E_T^{miss} or leading jet p_T distributions, as shown in Figure A.5.

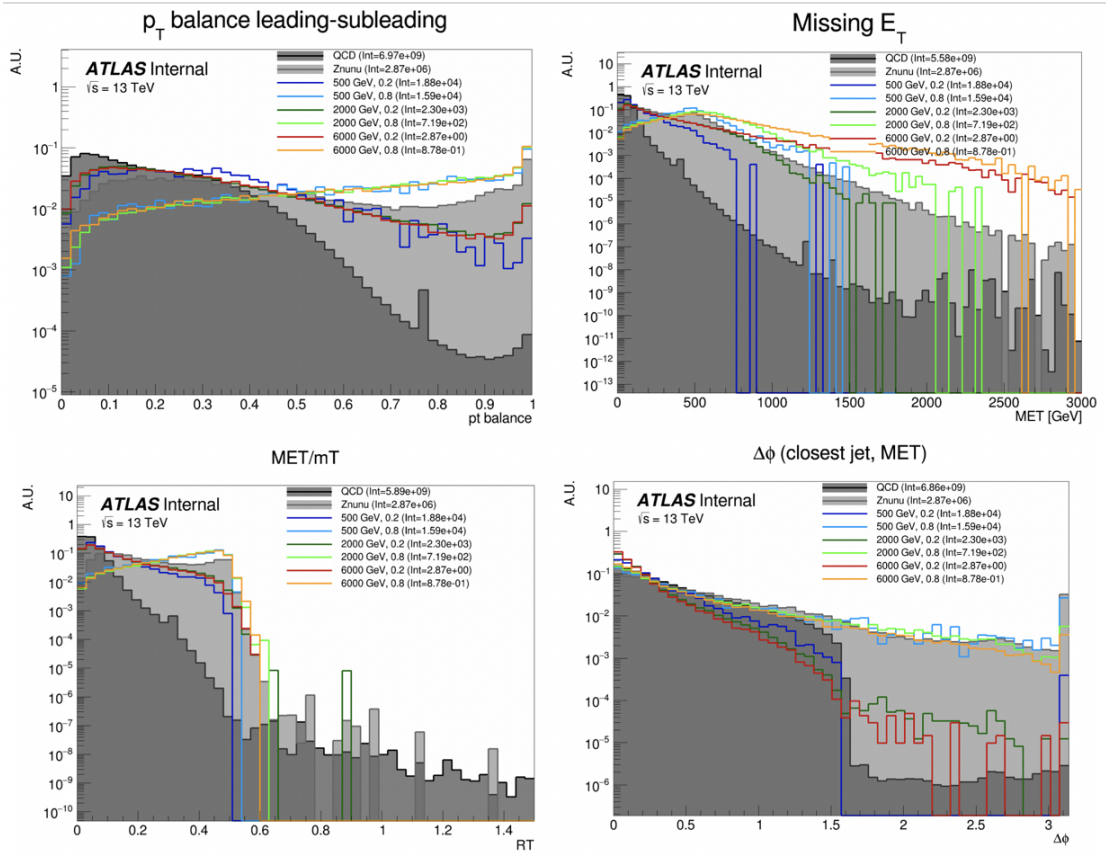


Figure A.4: Analysis variables where high R_{inv} signals a clearly distinct from background and low R_{inv} variables. On the contrary, leading jet p_T is one of the only variables where low R_{inv} signals are distinct from background.

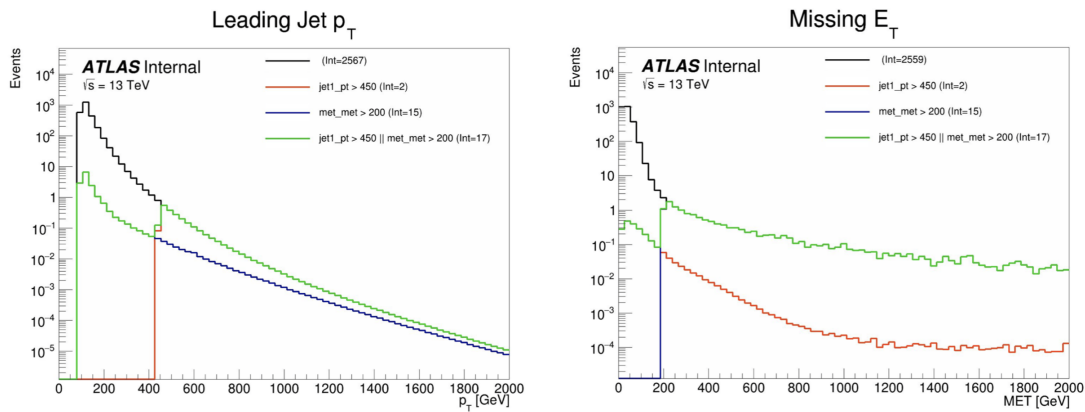


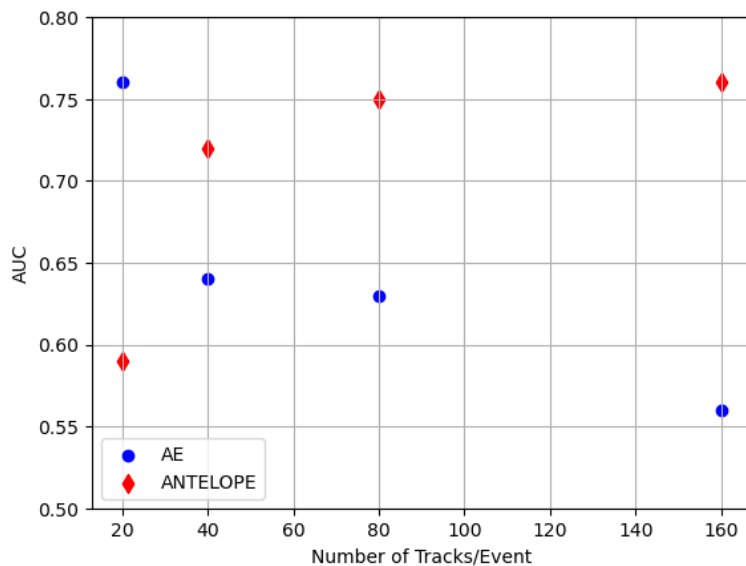
Figure A.5: OR of jet and E_T^{miss} triggers.

Appendix B: Machine Learning Approaches

2296 B.1 Unsupervised: AE vs. ANTELOPE

2297 To understand the benefits of the semi-supervised ANTELOPE approach, we study the AN-
 2298 TELOPE in comparison to a traditional anomaly detection architecture like an autoencoder. The
 2299 autoencoder cannot accommodate variable length or permutation invariant inputs.

2300 Figure B.1 shows the AUC determined by each of these two tools as a function of number
 2301 of tracks. The trend is that the AE suffers when more information is given, due to the presence
 2302 of 0-padding. In contrast, the ANTELOPE architecture performs better with more information,
 motivating the use of high dimensional input modelin with this method.

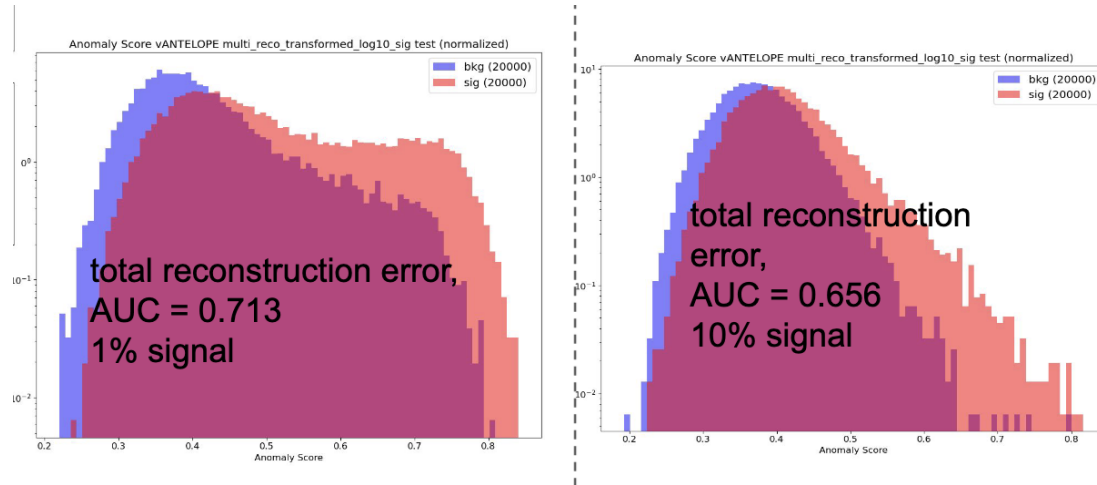


- Confirms that AE is negatively sensitive to zero padding while ANTELOPE sees a performance improvement as it sees more “information”

2303 Figure B.1

2304 **Signal Contamination**

2305 To understand the effect of signal contamination in training on the ANTELOPE score, we inject
2306 a percent of signal events into the data used to train the ANTELOPE autoencoder stage and look
2307 at the AUC on signals. Figure B.2 shows no variation in AUC with 1% contamination in training
data, but a few % drop going up to 10%.



2308 **Figure B.2**

2309 **B.2 PFN Optimality Checks**

2310 The PFN is trained using QCD as the background. A study was done to compare the perfor-
2311 mance of the tool in the analysis context if it trains against QCD or a representative MC background
2312 considering the small fractions of other processes ($V+jets$, top) that would contribute at preselec-
2313 tion. Figure B.3 shows the AUC across the grid for both training approaches, revealing better
2314 performance if the tool focuses on learning QCD differences.

2315 Further studies were done to ensure the relatively optimality of the single PFN model, trained
2316 over combined signals, across the grid. As the grid spans signals with a large range of E_T^{miss} , their
2317 varying input features and background composition may be conducive to separate PFN models
2318 trained on high and low E_T^{miss} signal points to better capture the signal-background differences.
2319 Figure B.4 shows a comparison of the signal-inclusive PFN model performance and the perfor-

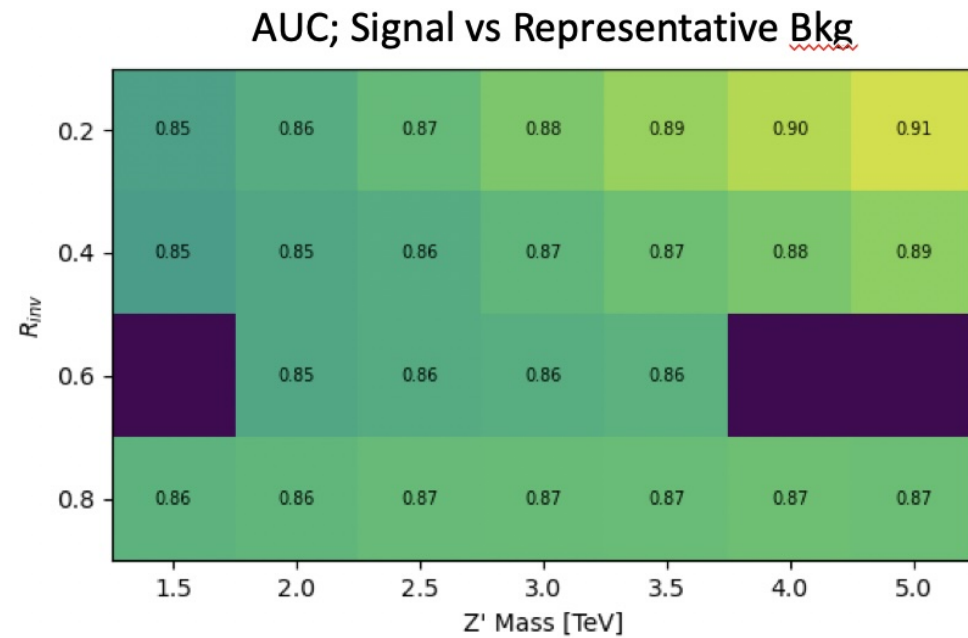
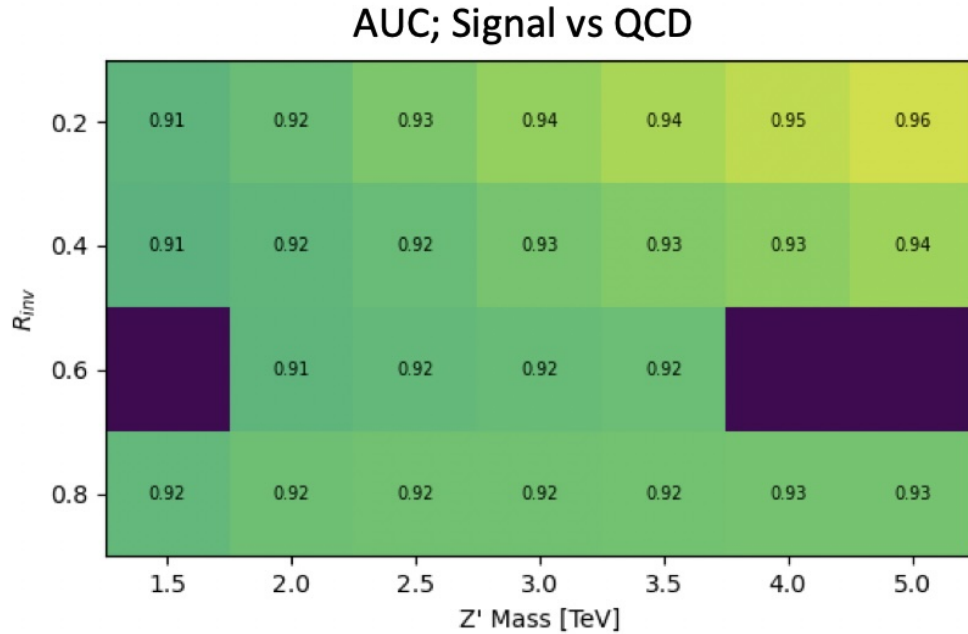


Figure B.3: AUC from the PFN score for each signal in the SVJ grid, shown versus the QCD-only training sample (top) and the total MC background (bottom). Note the three missing points will be added shortly - they were delayed due to a DAOD production mistake.

2320 mance of models separated into high and low R_{inv} signals in training. The most notable impact is
 2321 found for the low R_{inv} and high mass points, indicating that the signal-inclusive PFN is learning
 2322 morning about the distinction between high- E_T^{miss} signals and backgrounds. However, these high
 2323 mass points are also the most challenging to find due to their very wide resonance on top of m_T ,
 2324 and in the final projected sensitivity in the m_T window the differences are $< 10\%$ across the grid.
 2325 To maintain a harmonized strategy with the ANTELOPE region we keep the inclusive PFN model
 2326 as the final version.

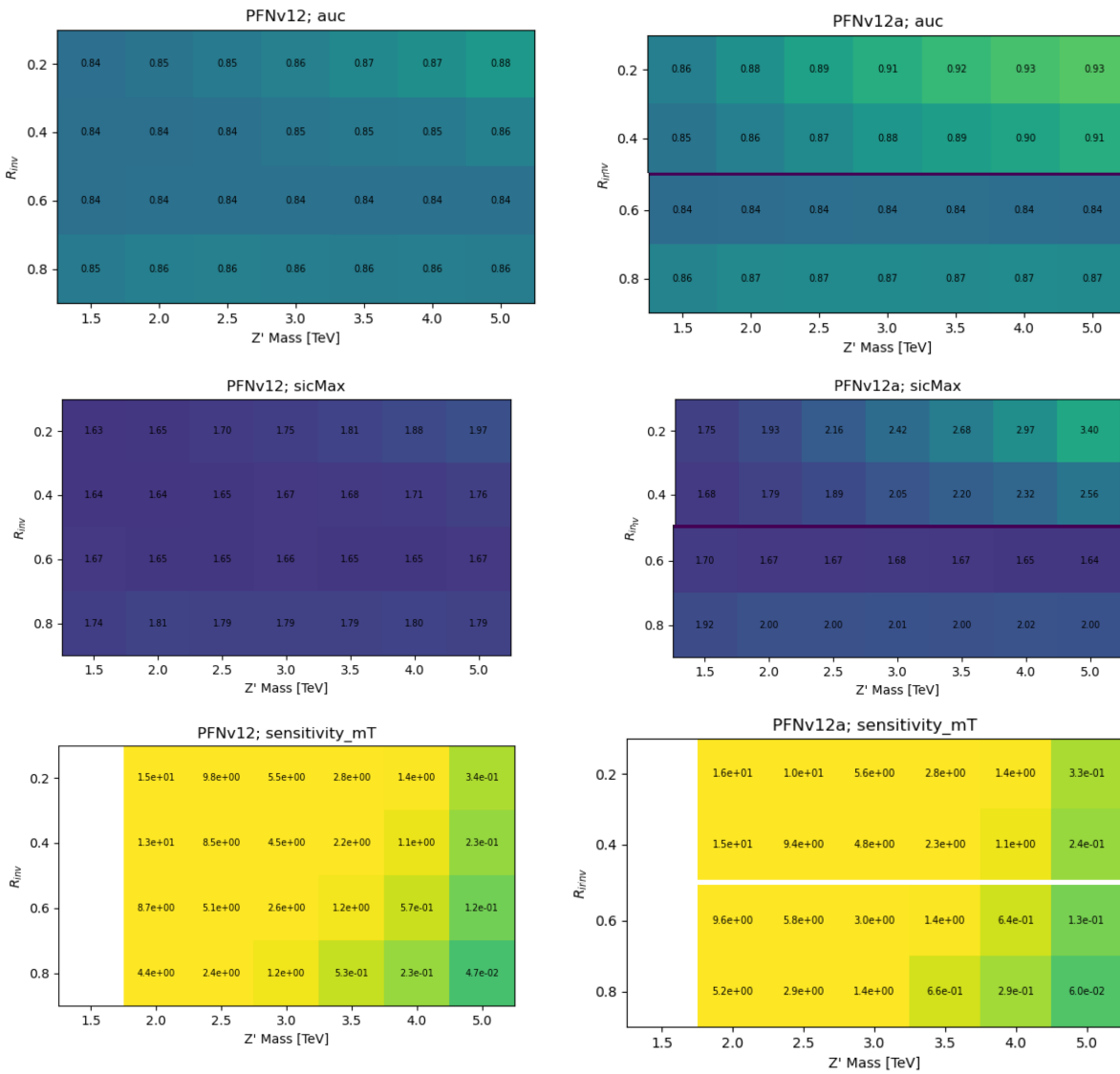


Figure B.4: Comparison of PFN AUC (top), SIC (middle), and sensitivity in the m_T mass window (bottom) for a single PFN model (left) vs. two models, trained on $R_{inv} < 0.5$ and > 0.5 separately.

2327 Figure B.5 shows the optimal cut on the PFN score for each point in the signal grid, motivating
the loose inclusive choice used to define the SR.

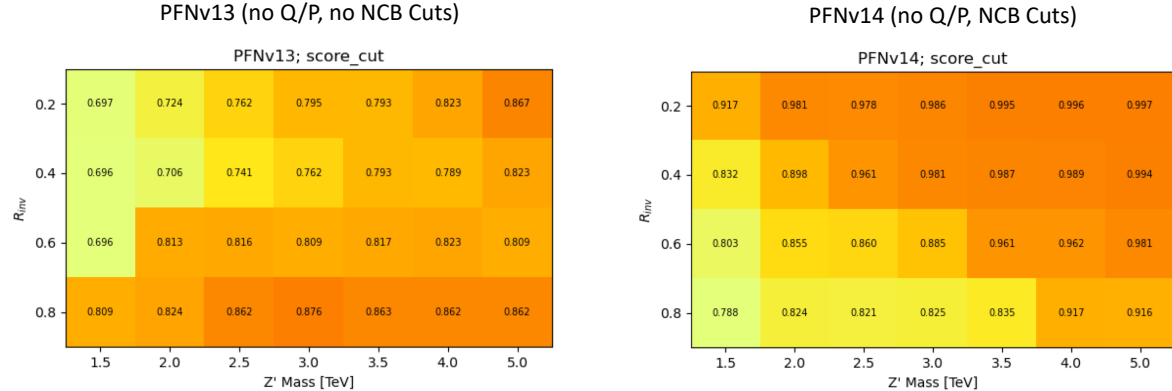


Figure B.5: Preferred cuts on the PFN score for each point in the grid, comparing the effect of adding the NCB preselection.

2328
2329 Grid cans for optimality were also performed on the number of training epochs, number of
2330 training events, batch size, learning rate, number of neurons, and dimension of the Φ space. The
2331 results of these scans are summarized in the tables in Figure B.6. The selected or default parameters
2332 were found to be optimal, or close enough to optimal to justify not increasing the training time or
2333 complexity of the network for negligible increases in performance.

2334 B.3 Supervised: BDT vs. PFN

2335 Studies of the BDT compared to the PFN performance, where training over events modeled
2336 with jet-related HLVs (high-level track variables, etas, angles, etc.) are compared to events mod-
2337 eled by the tracks of the 2 leading jets. Figure B.7 shows the performance of the BDT with and
2338 without explicit use of energy scale variables.

2339 B.4 Single Jet vs Jet System ML Approach

2340 The analysis considered both a single jet and jet system ML approach. A jet system approach,
2341 where the leading two jets and their orientation with respect to each other was selected for a variety
2342 of reasons. The jet system approach captures the MET information which is crucial to identifying

	default s_events=500096 b_events=501396	s_events:49135 b_events: 48220 *	s_events:246205 b_events:245136
AUC	.905	.874	.892

	default n_neuro n 40	n_neuro n 150	phi_dim 32	phi_dim 128	learning rate 0.0005	learning rate 0.002	nepochs 50	nepochs 200*	
AUC	.905	.898	.906	.902	.906	.898	.905	.893	.909

	default	batchsize_pfn 250	batchsize_pfn 1000
AUC	.905	.903	.902

Figure B.6: Scans done to check for optimality of PFN training parameters.

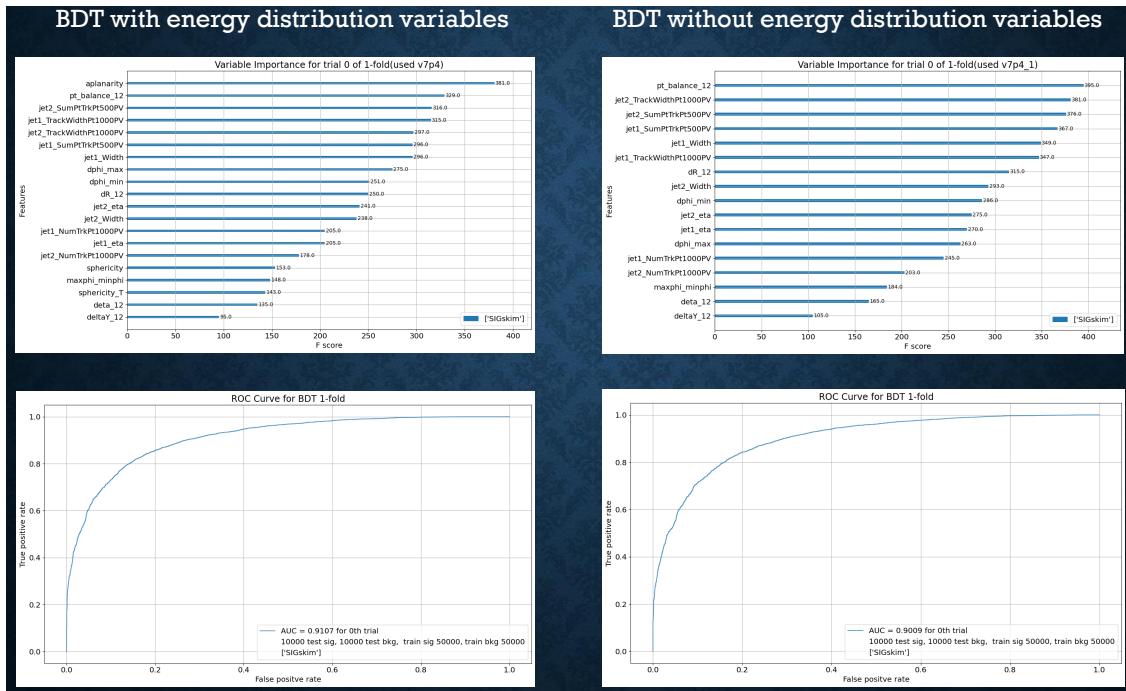


Figure B.7

2343 SVJs. In the topology where the dark quarks come from a heavy Z' decay and are back to back,
 2344 the measurable MET will have to be aligned with one or the other.

2345 Additionally, the performance of both a supervised PFN approach and an unsupervised AE ap-
 2346 proach was studied in the case of a single jet tagger. While the PFN approach was still performant
 2347 on a single jet case, the unsupervised approach was significantly improved by using both jets. This
 2348 is shown in Figure B.8.

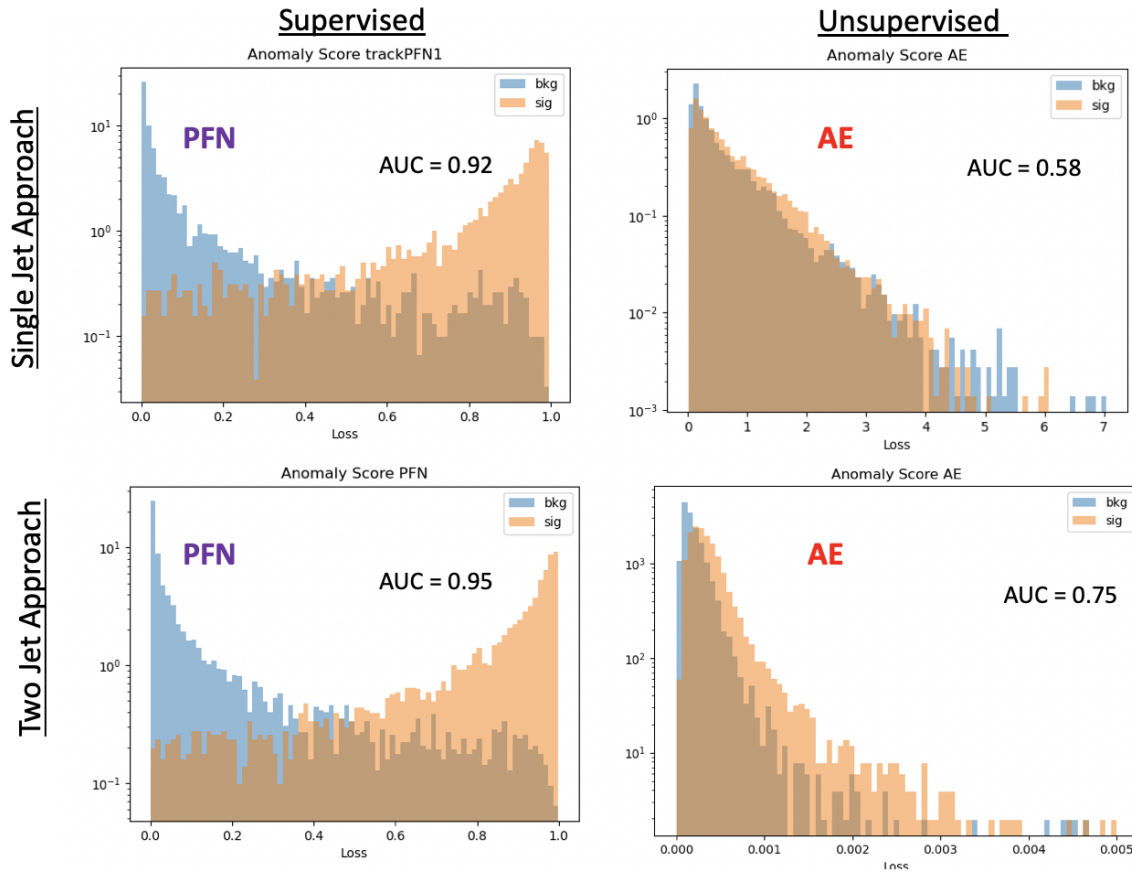


Figure B.8: ϕ Performance comparison between single jet and jet system ML approach

2349 B.5 PFN Training Composition

2350 The overall sensitivity and stability across the signal grid is observed to benefit by training
 2351 the ML tool to reject only the dominant background, QCD. This is evidenced by the PFN response
 2352 plots shown in Section 7.1.1 and the following AUC and sensitivity comparison plots in Figure B.9.

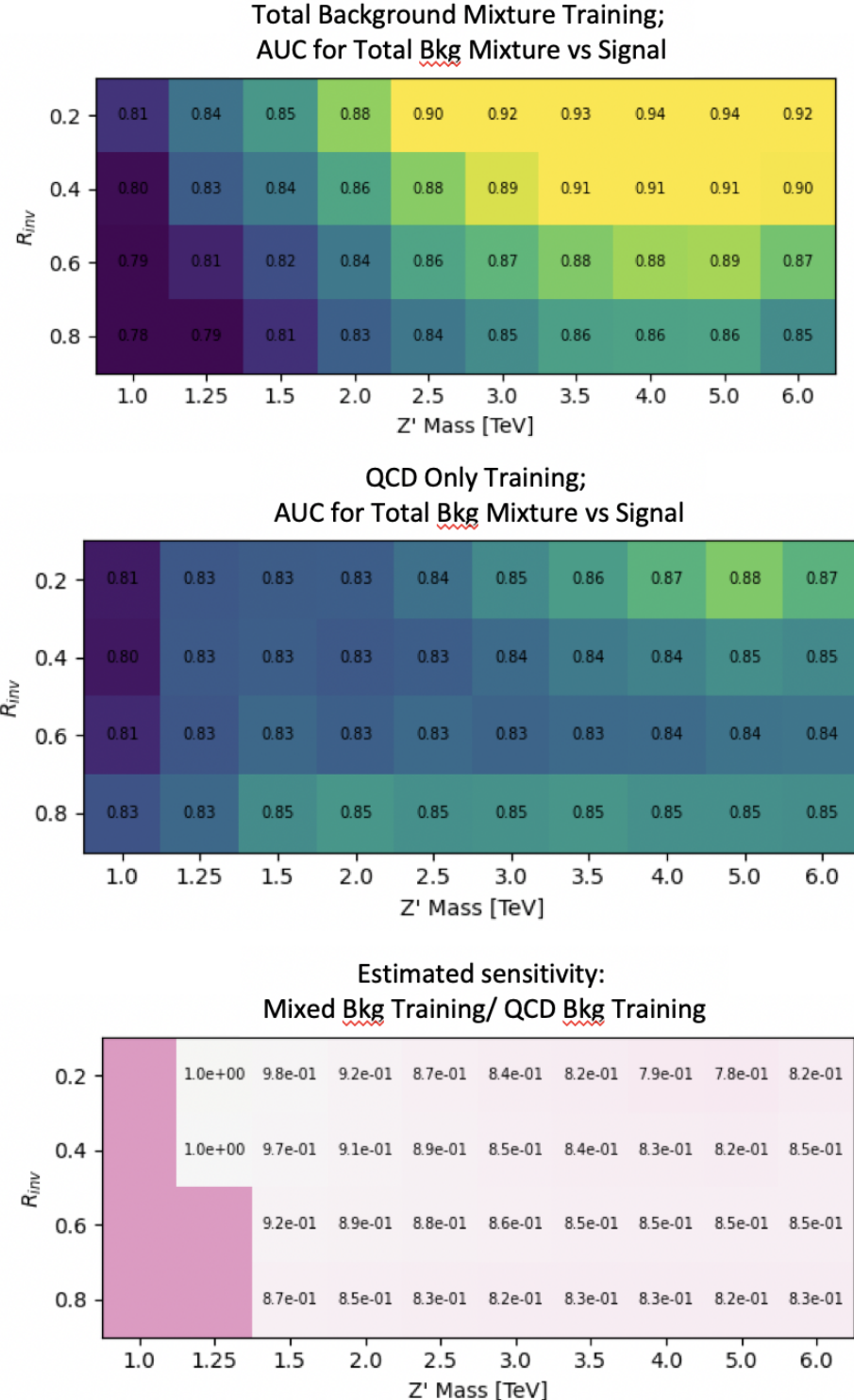


Figure B.9: ϕ Comparison in the AUC score across the grid for the mixed background strategy vs the QCD only strategy. The bottom table highlights that the QCD only strategy gives superior sensitivity across the signal grid.

2353 **B.6 E_T^{miss} and $E_T^{\text{miss}}\phi$ Shapes**

2354 The Tight cleaning working point was found to be necessary due to the nature of our signal
 2355 being E_T^{miss} and hadronic activity that are closely aligned, presenting a signature that is very af-
 2356 fected by beam-induced background (BIB). As per the cleaning recommendations, any event with
 2357 a jet that fails Tight criteria is rejected. Figure B.10 shows the effect of Tight cleaning on the shape
 of E_T^{miss} in data, fixing a feature present in Loose cleaning only.

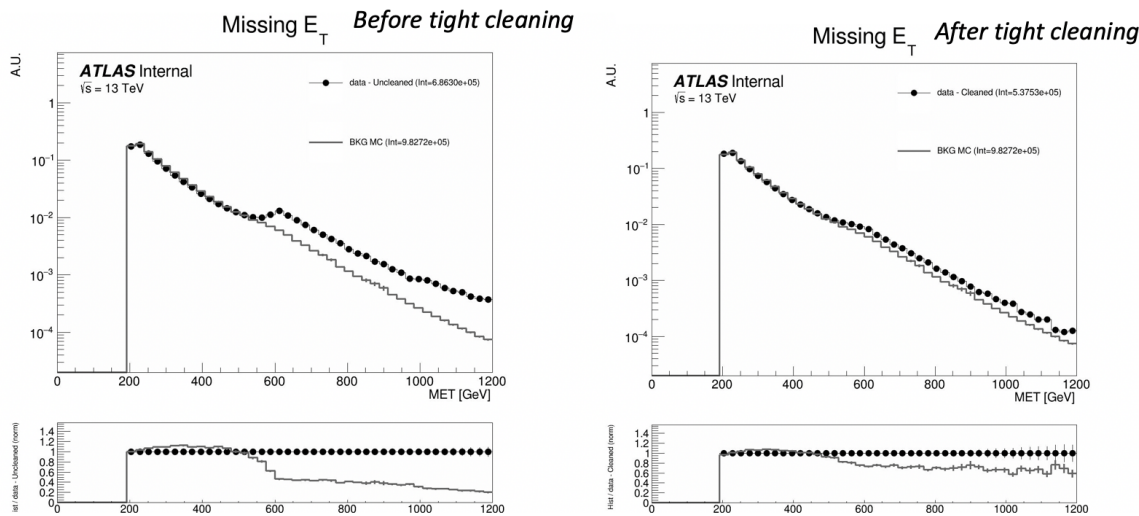


Figure B.10: E_T^{miss} in data before and after Tight event cleaning is applied.

2358
 2359 Figure B.11 further illustrates the correlation between the excess events and the leading jet p_T ,
 2360 and illustrates the impact of the tight cleaning in reducing this feature.

2361 Figure B.12 illustrates the 2D η vs ϕ distribution of the leading and subleading jets before and
 2362 after tight cleaning. No major spikes or hot areas are observed. One bright spot in the subleading
 2363 jet map at $\eta \approx 0$ and $\phi \approx -1.0$ was studies and found to have no impact on the E_T^{miss} shape, indicating
 2364 a likely missed spot in the Tile cleaning which does not affect E_T^{miss} .

2365 **B.6.1 NCB Preselection**

2366 A final preselection was derived to entirely remove the presence of non-collision background,
 2367 particularly noted through its impact on the E_T^{miss} shape. Cuts are added on the subleading jet

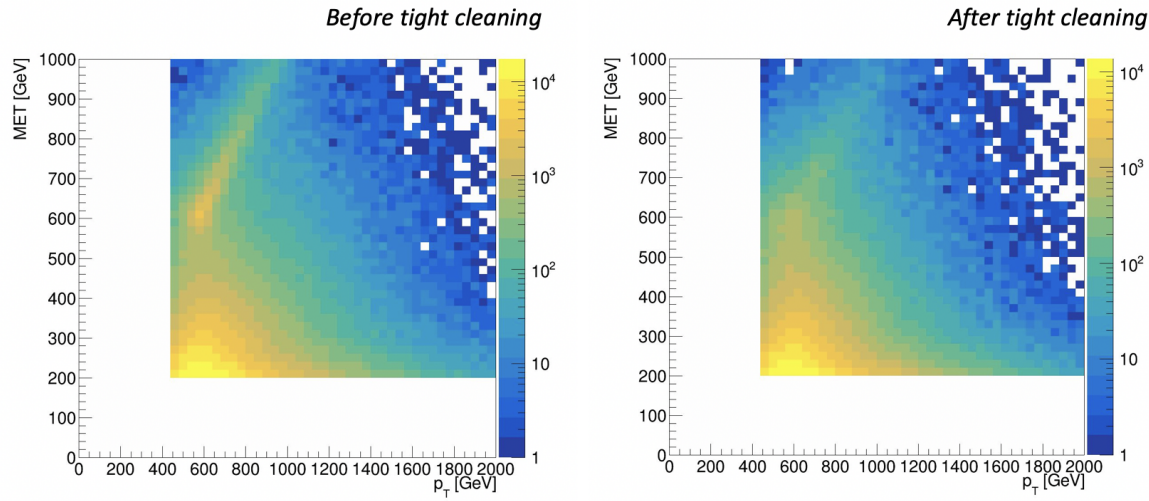


Figure B.11: E_T^{miss} vs jet1 p_T in data before and after Tight event cleaning is applied.

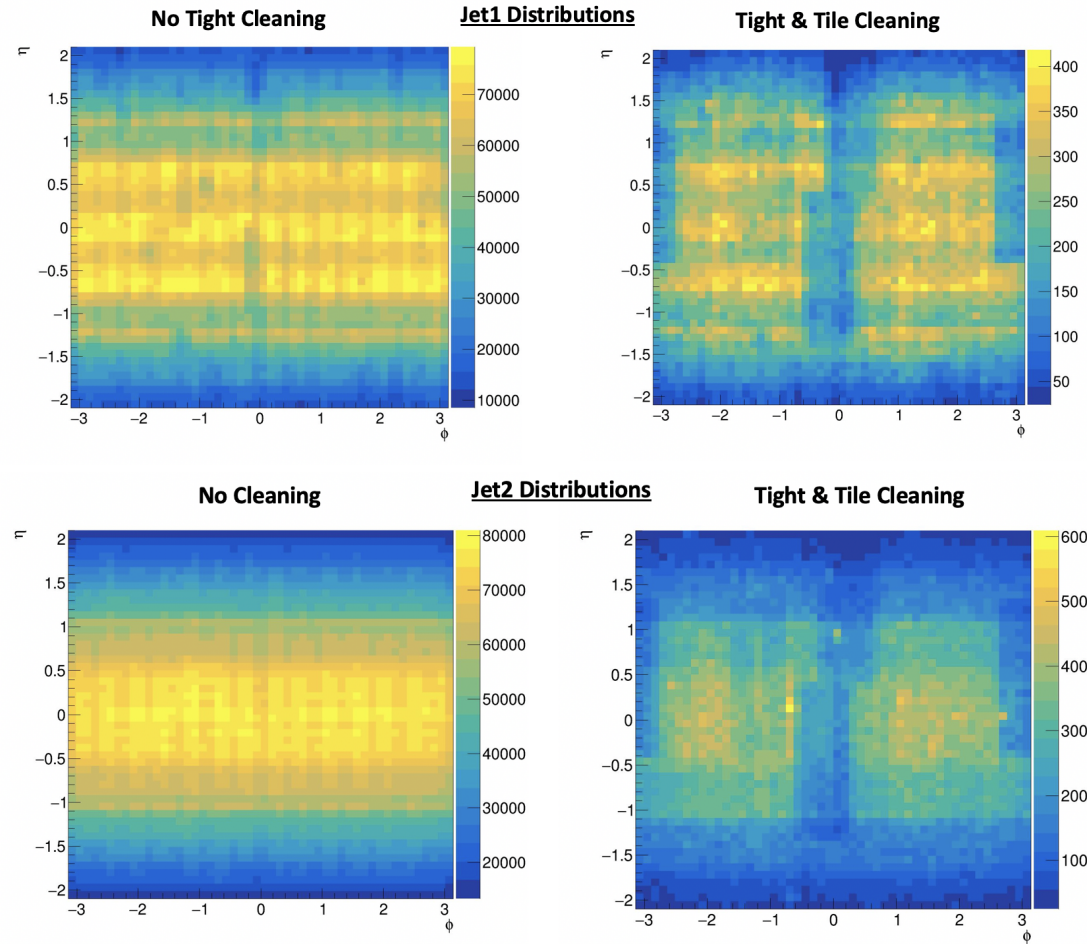


Figure B.12: η vs ϕ for leading and subleading jets, before and after the application of tight cleaning.

2368 $p_T > 150$ GeV and $\Delta\Phi(j1,j2) > 0.8$. Figure B.13 shows the impact of these cuts to create a fully
 2369 smoothly falling E_T^{miss} distribution. Figure B.14 shows the impact on the data yields in the CR and
 2370 VR and several signals in the SR; the greatest inefficiencies are found for the signal points that are
 2371 not sensitive in the analysis anyway. The reduction in background ultimately means that no impact
 is noticed on the limits.

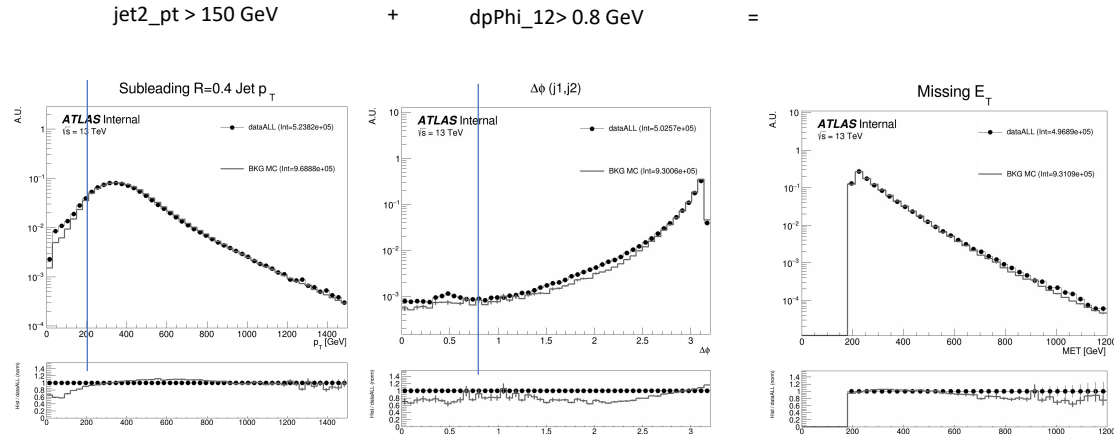


Figure B.13: Added NCB preselection and impact on E_T^{miss} shape.

2372
 2373 Figure B.15 shows the impact of these cuts on the 2D E_T^{miss} vs jet1 p_T distribution, where the
 2374 feature is also observed to be smoothed.

2375 This strategy was discussed and signed off by the Jet/ E_T^{miss} CP group ¹.

2376 B.6.2 TileCal Correction

2377 The $E_T^{\text{miss}}\phi$ distribution was fixed through the implementation of an offline TileCal correction
 2378 tool, which removes certain lumiblocks of certain runs based on poor functioning in TileCal mod-
 2379 ules. Figure B.16 shows the $E_T^{\text{miss}}\phi$ distribution in data across runs, before and after the application
 2380 of the tool, showing the ability of the tool to remove spikes due to instrumental problems.

¹<https://indico.cern.ch/event/1413217/>

Region	Before Extra Cleaning Cuts	After Extra Cleaning Cuts	Efficiency
Data - CR	108957	107435	0.99
Data - VR	116917	116008	0.99
2500, 0.2 - SR	1921	1709	0.89
2500, 0.4 - SR	1819	1424	0.78
2500, 0.6 - SR	1150	735	0.64
2500, 0.8 - SR	543	251	0.46
5000, 0.2 - SR	21.5	20.3	0.94
5000, 0.4 - SR	22.3	19.4	0.87
5000, 0.6 - SR	16.0	11.6	0.73
5000, 0.8 - SR	8.1	4.1	0.51

Figure B.14: NCB preselection impact on data and signal yields.

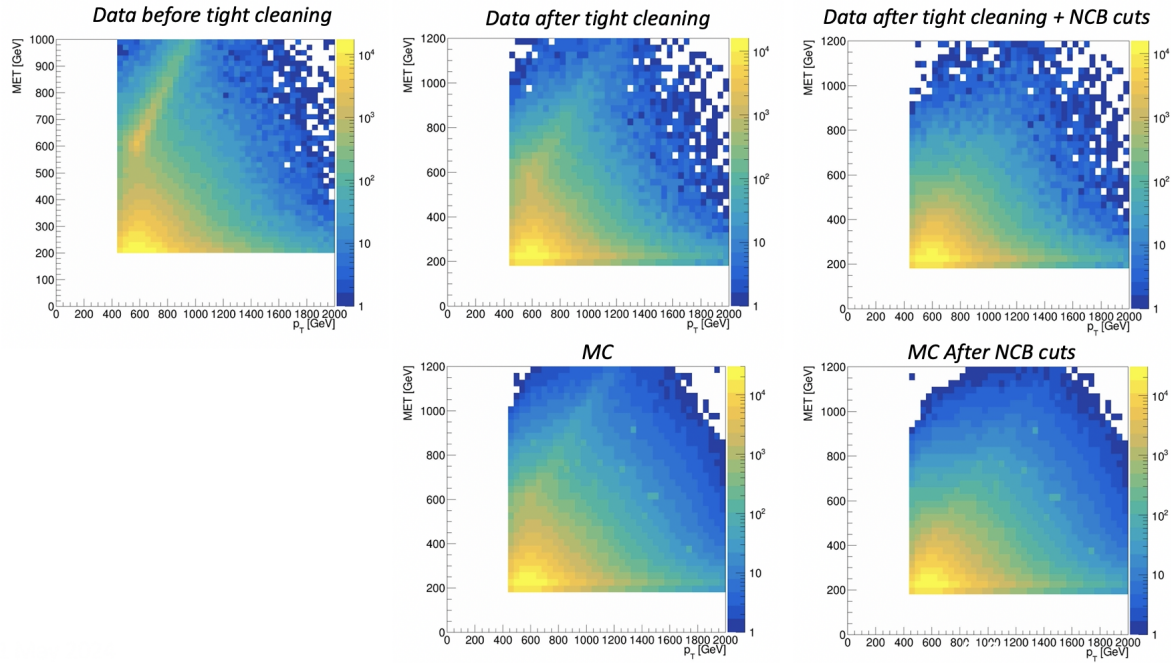


Figure B.15: Impact of tight cleaning and non-collision background preselection.

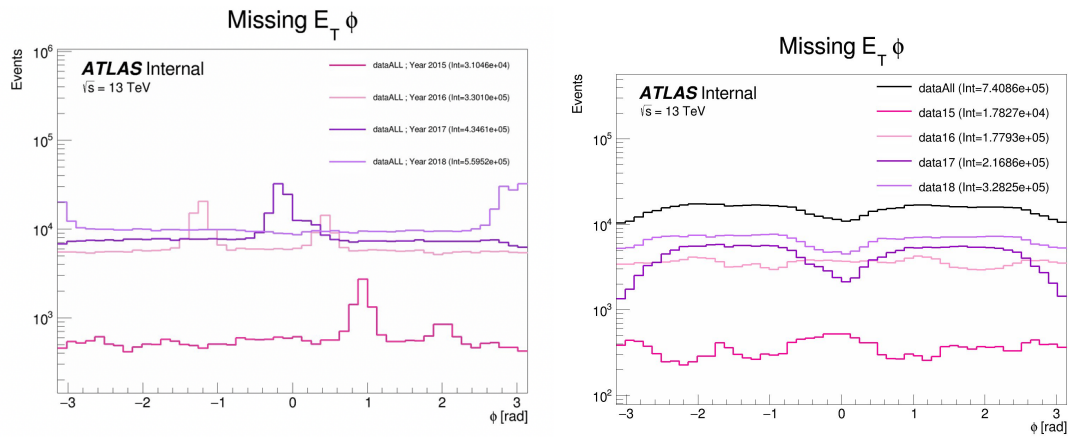


Figure B.16: $E_T^{\text{miss}}\phi$ in data, before (left) and after (right) application of the TileCal correction tool.

2381

2382

Appendix C: Truth Studies

2383 C.1 Jet dR Matching

2384 Figure C.1 demonstrates that the leading and subleading jet are overwhelmingly the most likely
2385 jets to be matched to a dark quark.

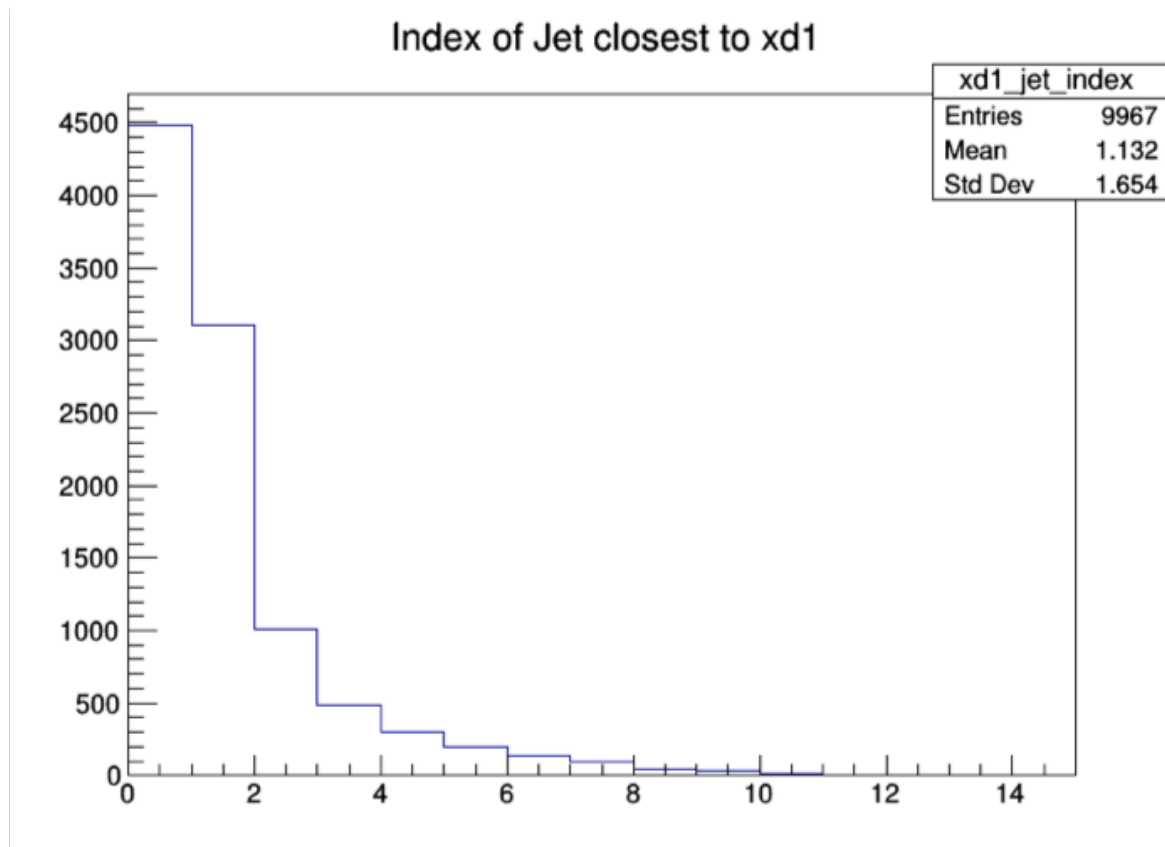


Figure C.1: Index of jets truth matched (by requirement of $\Delta R < 0.4$) with dark quark.

2386 Other matching strategies were explored, such as choosing the jet most aligned with $E_T^{\text{miss}}(\min$
2387 $\Delta\phi(j, E_T^{\text{miss}}))$ and the jet most anti-aligned with $E_T^{\text{miss}}(\max \Delta\phi(j, E_T^{\text{miss}}))$. However, in most cases
2388 these two measurements correspond to the subleading and leading jets respectively. Additionally,
2389 as shown in Figure C.2 the leading/subleading strategy generally results in more matched jets than

2390 the E_T^{miss} aligned and E_T^{miss} anti-aligned strategy. Therefore the leading and subleading jets were
 2391 chosen for consideration in this analysis.

Signal ($M_{Z'}$, r_{inv})	% Leading Jets dR Matched	% MET anti- aligned Jets dR matched	% Subleading Jets dR Matched	% MET aligned jets dR matched
750 GeV, 0.2	0.432883	0.3567	0.3777	0.3504
750 GeV, 0.8	0.187819	0.1589	0.1826	0.1803
3500 GeV, 0.2	0.692931	0.5408	0.5097	0.4144
3500 GeV, 0.8	0.344057	0.2927	0.2634	0.2585
6000 GeV, 0.2	0.647237	0.5047	0.4975	0.3919
6000 GeV, 0.8	0.345542	0.2882	0.2517	0.249

Figure C.2: Percent of jets with $\Delta R(j, E_T^{\text{miss}}) < 0.4$ comparing two jet identification strategies. Leading and subleading jets are seen to be the better metric for identifying jets associated with the dark quark decay.

Appendix D: BumpHunter

2394 D.1 Signal Mass Resolution m_T Binning

2395 In the discovery region, a binning for m_T is determined that is based on the expected signal
 2396 width. This is done to improve the BumpHunter performance. The signal mass resolution for a
 2397 given point is determined with a double-sided Crystal Ball fit to the mass. These fits are performed
 2398 across Z' mass, and a linear fit to these values is performed to determine the optimal bin width
 2399 across m_T .

2400 The x-axis value used is a data-driven way to determine the appropriate value of m_T for a given
 2401 signal, given that the considerable E_T^{miss} from the dark particles means that the truth Z' mass does
 2402 not well approximate the peak m_T value. The E_T^{miss} in the final state is generally an underestimate
 2403 of the amount of energy that could be attributed to dark hadrons, as any dark hadrons that are
 2404 back-to-back in the transverse plane will cancel out and not register as E_T^{miss} . Therefore m_T is
 2405 always an underestimate of the Z' mass, so the truth Z' mass can be used as an upper bound. An
 2406 integral is then performed backwards from that value until 60% of the total signal yield is included.
 2407 This window is referred to as the 60% mass window; the mean of this window then provides an
 2408 approximate localization of the signal mass peak in m_T . Figure D.1 shows some examples of this
 2409 algorithm on several signal points of varying R_{inv} and mass.

2410 Figure D.2 shows the result of this linear fit for the four R_{inv} values considered in the signal
 2411 grid. As expected, the resolution is considerably different for low and high R_{inv} points.

2412 A single m_T binning for the final SR plotting and BumpHunting is determined by selecting a
 2413 harmonized binning at low m_T , and moving to wider bins at high m_T . As for higher R_{inv} signal
 2414 points the mass resolution linear fit gives negative results, we require each bin to have a width of
 2415 at least 100 GeV. Figure D.3 shows the resulting bins for each R_{inv} category that comes from the

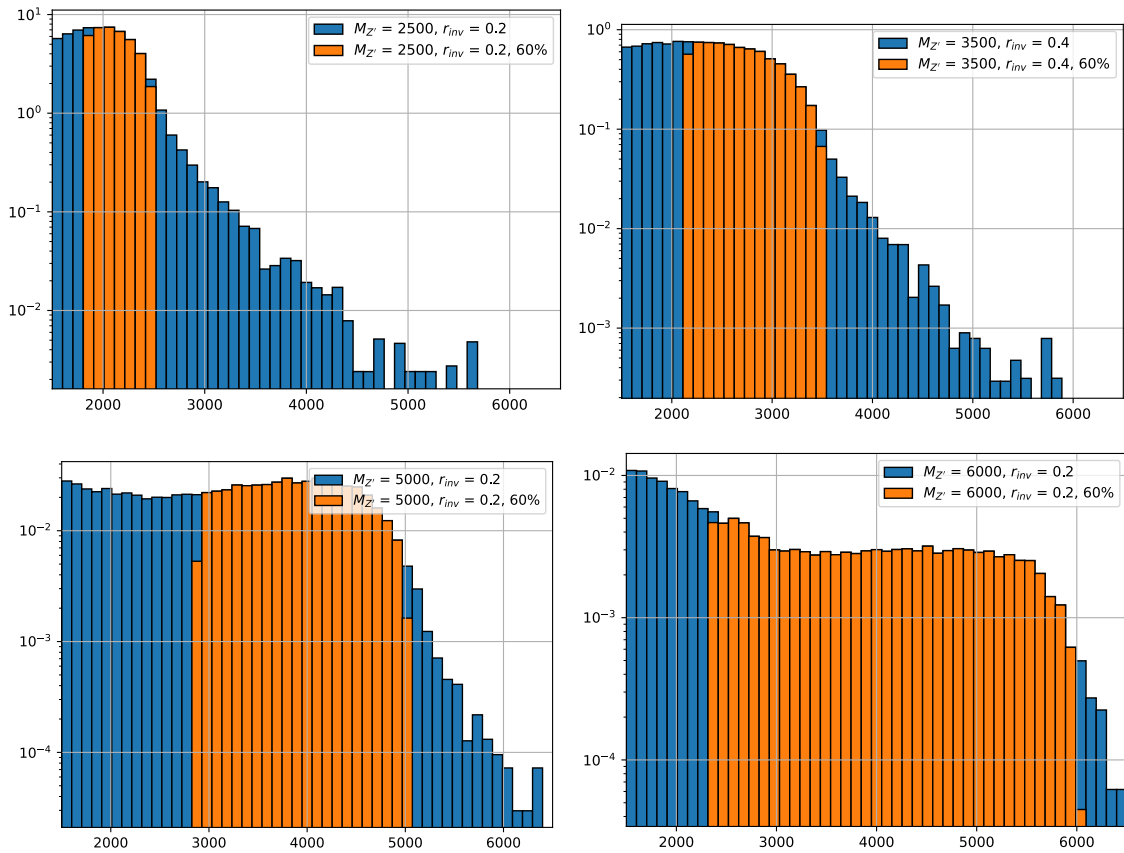


Figure D.1: Example determinations of the 60% mass window means for several signal points.

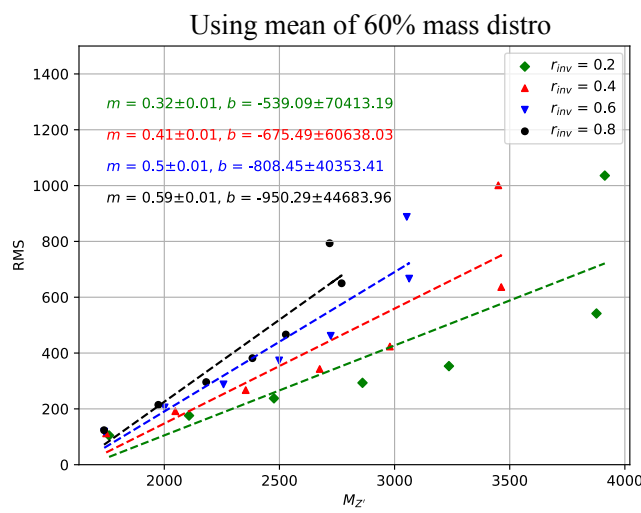


Figure D.2: Signal mass resolution for m_T binning for the signal grid in (R_{inv} , mass) space.

mass resolution fits, with the addition of the minimum 100 GeV bin width requirement.

$r_{inv} = 0.2 \rightarrow [1500, 1600, 1700, 1800, 1904, 2029, 2177, 2356, 2569, 2824, 3128, 3493, 3929, 4451, 5075, 5822, 6715]$

$r_{inv} = 0.4 \rightarrow [1500, 1600, 1700, 1800, 1910, 2053, 2238, 2477, 2787, 3187, 3704, 4374, 5240, 6361]$

$r_{inv} = 0.6 \rightarrow [1500, 1600, 1700, 1800, 1919, 2087, 2321, 2650, 3110, 3755, 4659, 5925, 7698]$

$r_{inv} = 0.8 \rightarrow [1500, 1600, 1700, 1800, 1927, 2117, 2400, 2823, 3455, 4400, 5811, 7918]$

Figure D.3: m_T bins based on the signal mass resolution and the minimum 100 GeV width requirement, for each R_{inv} signal category.

2416

2417 In order to have a final m_T binning that is not highly model-dependent, we consolidate these
2418 four different bins into a single binning which is provided below:

2419 **[1500, 1600, 1700, 1800, 1900, 2025, 2175, 2350, 2575, 2825, 3125, 3500, 3925, 4450, 5075,
2420 6000]**